The structure and dynamics of the Vela OB2 association

Joseph Armstrong

Doctor of Philosophy

Department of Physics, Keele University

December 2021

Abstract

This thesis presents studies of the structure and dynamics of the Vela OB2 association. OB associations are sparse, gravitationally unbound groups of young stars, vital for studying the formation and early evolution of stars and star-forming regions, and the formation of the Galactic field population. The majority of stars in our Galaxy and others form in associations or clusters, ranging in size from hundreds of stars to tens of thousands, but only a small fraction of these groups are dense enough to remain together for a long time (Lada & Lada 2003). OB associations represent the transitional phase of these groups between formation from turbulent molecular clouds to dispersion into the Galactic field. And it is in these early stages of a star's life that their subsequent evolution is determined and in which they form planetary systems.

We used Gaia DR1 and 2MASS photometry to trace the wide-scale population of YSOs (young stellar objects) across Vela OB2, using the GES (Gaia ESO Survey) sample of the γ Vel cluster as a basis. We plot a YSO density map and select targets for two observing runs, complementing it with Gaia DR2 photometry and astrometry for the second observing run. The spectra were used to obtain radial velocities (RVs) and Lithium equivalent-widths (EW(Li)s), the latter used to confirm the youth of our targets. We used the first set of spectra to study the A and B populations identified by Jeffries et al. (2014), expanding on their sample. We investigated the kinematics of the two groups and found that while the γ Vel cluster (population A) did not show expansion, the wider Vela OB2 sources (population B) does show significant evidence for expansion.

The second set of spectra provided a sample of $\sim$400 YSOs across Vela OB2 with 3D spatial and kinematic data. We identify significant substructure and separate the sample into six groups, including the Vela OB2 association and three open

clusters. We find significant evidence of expansion in the association with a kinematic age of 13-23 Myr, in good agreement with literature ages of 15-20 Myr. We also trace back the motion of the association and the clusters, constraining their arrangement at formation. Finally, we identified a number of candidate runaways stars, and show that by using RV and age estimates for the stars we can rule out the majority of these as runaways from known clusters.

Acknowledgements

Firstly, I would like to give special thanks to my supervisor, Dr Nick Wright, for his patient guidance and generous support, without which I would never have made it this far. I would like to thank Prof. Rob Jeffries and Dr. Richard Jackson for their advice and technical support, and I would like to thank the members of the Keele Astrophysics group and all my friends at the University for making my time there so enjoyable. Finally, I would like to thank my parents and my wife, Maelodee, for their constant love and care.

> "*The heavens declare the glory of God, the skies proclaim the work of His hands.*"
>
> – Psalm 19:1

Contents

List of Figures

List of Tables

1 Introduction

This chapter introduces the concepts of star cluster and association formation and evolution and the processes behind them. In order to understand where star clusters and associations come from we must understand how individual stars are formed, their origins in giant molecular clouds, their early evolution and environment. To understand how clusters and associations evolve we must understand how their member stars interact with each other and their environment, and have sufficient knowledge of the techniques needed to analyse the structure and kinematics of these groups.

1.1 Star Formation

1.1.1 Molecular Clouds

To understand how star clusters form and evolve, we must give some context regarding their birthplaces, namely Giant Molecular Clouds (GMCs). GMCs are vast complexes of molecular gas (predominantly H_2), which can be as large as hundreds of parsecs across and can have masses anywhere in the range $\sim 10^4 - 10^6 \, M_\odot$. Rather than having uniform density or a smooth density gradient, they have been found to be substructured in filaments (Fig. 1.1), sheets and clumps (Williams, Blitz & McKee 2000). The internal motions of the molecular gas within a GMC are driven by turbulence, often as the result of feedback mechanisms from stars, and are kept from overall gravitational collapse by thermal and magnetic pressure.
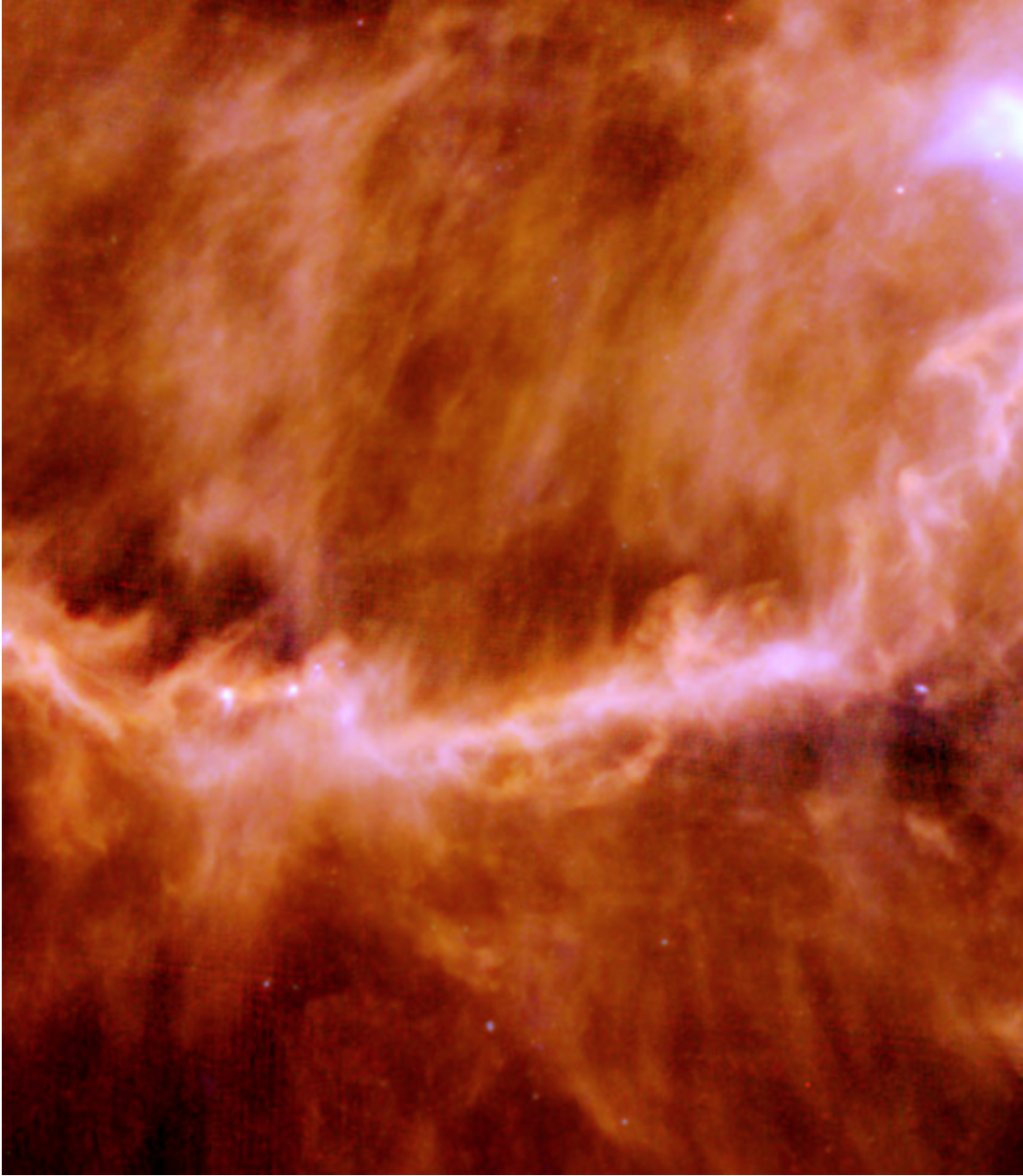
Figure 1.1: The B211 filament in the Taurus molecular cloud running left to right across the image. Striations tracing the magnetic field of the cloud perpendicular to the main filament are visible, as well as bright dots indicating newly formed stars. This image spans about 2×5 degrees (10×25 pc) and combines Herschel bands at 160 μm (blue), 250 μm (green) and 500 μm (red). Credit: ESA/Herschel.

1.1.2 Formation Of Stars

The densest regions of molecular clouds fragment and produce prestellar cores, and it is when gravity in these cores becomes sufficient to overpower internal pressure that they begin to collapse and heat up. The Jeans mass, the critical mass required for gravity to overcome internal pressure, for a molecular cloud of radius R is given as

$$M_J = \frac{3kT}{2Gm}R \tag{1.1}$$

where m is the average mass of a particle in the cloud, T is the absolute temperature, G is the gravitational constant and k is Boltzmann's constant. Magnetic fields can also contribute to the internal pressure inhibiting collapse, up to about 30% of the thermal pressure support (McKee & Tan 2003). When a dense core exceeds this critical mass and begins to collapse it will continue to accrete molecular gas and as it heats up it will produce infrared radiation. Such an object is known as a protostar. Infalling molecular gas impacts the star in a shock-front, which heats up incoming material further. Young objects that are not yet hot enough to ignite hydrogen are known as "pre main-sequence" stars. Their luminosity comes from the release of gravitational potential energy as they collapse and contract, rather than fusion reactions, and so, as they accrete material and heat up, their mass and luminosity change until joining the main-sequence. This evolution can be modelled and illustrated diagramatically (Fig. 1.2). Eventually the protostar will become hot enough to burn deuterium and drive convection. Depending on its mass, this phase may be short lived before the star ignites hydrogen and for the most massive stars ($> 10M_\odot$), hydrogen burning begins while material is still infalling. When a star begins fusing hydrogen in its core it enters the main-sequence and its mass and luminosity remain stable until it starts to run out of fuel in the core.

Star formation occurs within GMCs preferentially along filaments and the regions of highest density, where filaments converge (known as hubs), are where
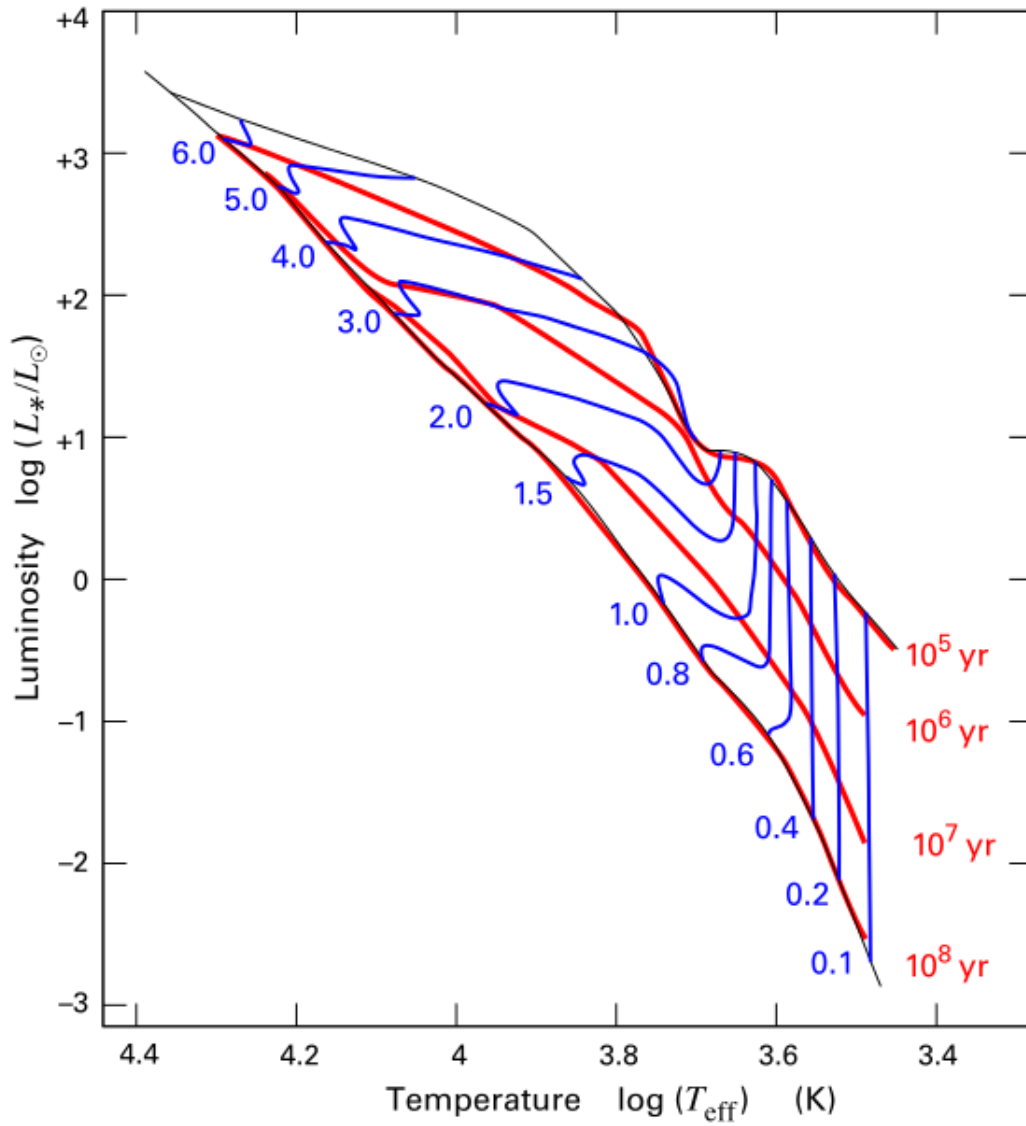
Figure 1.2: An illustration of PMS evolutionary tracks (blue) and isochrones (red) in temperature vs luminosity (Stahler & Palla 2008). A PMS star of a given mass ($M_\odot$ given in blue) will move along an evolutionary track as it ages until it reaches the zero age main-sequence (ZAMS, in black). A PMS star of a given age will be located at a point on the relevant isochrone depending on its mass. These evolutionary models are only approximations however, and the apparent position of a star on an observational HR diagram may vary due to binarity, variability or accretion.

high-mass stars are thought to form (Schneider et al. 2012). Gas and dust are funnelled along these filaments into dense regions that contract and fragment, creating prestellar cores which eventually form young stars. Since many cores can form and fragment in hub-filament systems, stars will form from these cores often hundreds at a time within ∼10 pc scales. In this proximity the young stars can form gravitationally bound groups called star clusters.

1.1.3   The Initial Mass Function

The single most important factor in determining a star's evolution in the future is it's mass at formation or 'initial' mass. While a single star's initial mass may be determined by a complex combination of physical variables, such as molecular gas density, proximity to other stars during formation, tidal forces etc. the distribution of masses in a population of stars has been found to follow a functional form. The functional form of this distribution is what is known as a population's initial mass function (IMF), and has been found to be surprisingly universal both in the solar neighbourhood and beyond (Lee et al. 2020). Since its introduction by Salpeter (1955) there have been numerous studies determining cluster IMFs from luminosity functions (Massey 2003), and many proposed functional forms have been put forward as information on stellar populations have improved (Salpeter 1955; Miller & Scalo 1979; Kroupa 2002; Maschberger 2013). For an illustration of a modern IMF see figure 1.3.

A key feature of a stellar population that results from its IMF is the ratio of high- to low- mass stars. The vast majority of stars formed in a population will have masses of the range $0.1 - 1 M_\odot$, and the most massive O-type stars ($> 10 M_\odot$) occur with a rarity of a few in a thousand.

In Salpeter (1955), the IMF is modelled in the form of a power-law. However, Miller & Scalo (1979) concluded that the power-law form did not accurately describe
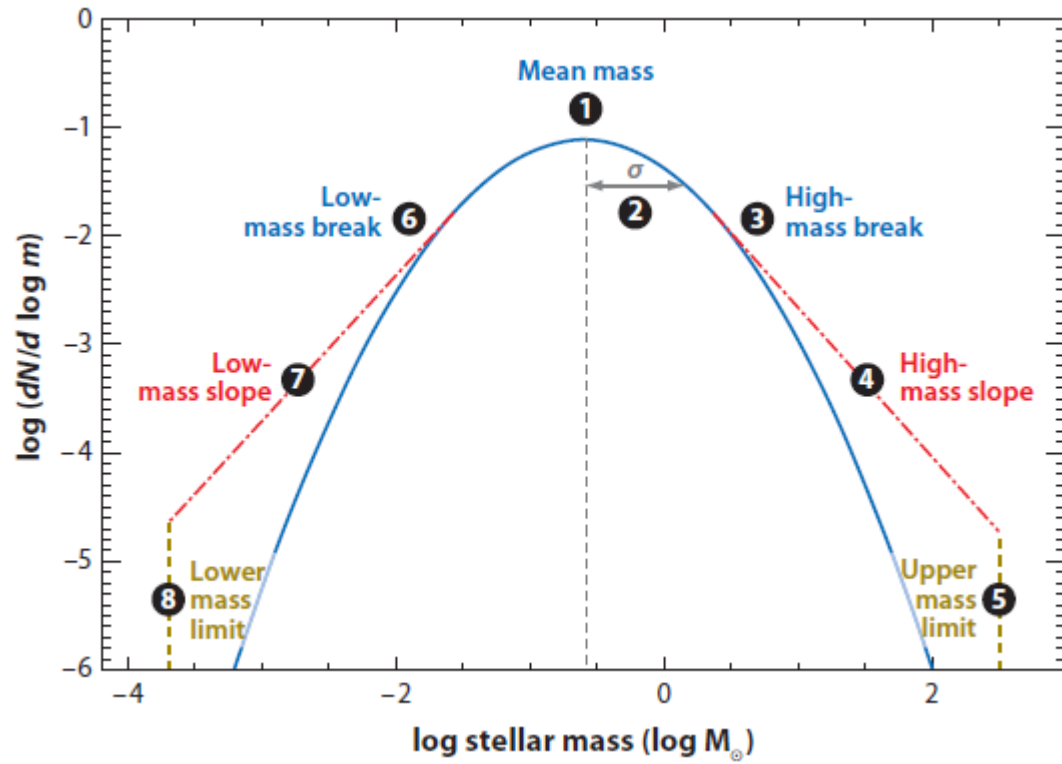
Figure 1.3: An illustration of an eight-parameter IMF (Bastian, Covey & Meyer 2010).

the distribution of lower mass stars and suggested that a logarithmic-normal form was a better fit.

$$\frac{dlog\xi(log(M))}{dlog(M)} = -(1 + log(M)) \qquad (1.2)$$

where M is stellar mass, where

$$\xi(log(M)) = \frac{dn}{dlog(M)} \qquad (1.3)$$

and where n is stellar number density.

The log-normal form was also given theoretical justification by Zinnecker (1984), who argued that if star formation is indeed a complex combination of independent physical variables (or can be approximated as such), then the Central Limit Theorem, which says that the normalised sum of independent random variables tends toward a normal distribution, can be applied to stellar populations and the mass distribution is normal in logarithmic scale. Studies since have indicated that the form of the IMF may not necessarily be continuous over the whole range of masses, discontinuities may arise at mass values where different physical mechanisms in star formation become more or less prevalent over others, introducing extra complexity to models.

1.1.4 Feedback

Feedback is the name of the process by which stars affect their environment. Feedback processes include supernovae from the most massive stars, as well as stellar winds, ionisation, radiation pressure, jets and molecular outflows. It is thought that feedback processes are responsible for the dispersal of gas which brings star formation to an end and determines the final masses of forming stars, influencing the dynamics of young clusters by shaping the residual gas and thus the local gravitational potential and eroding protoplanetary disks, which influences the development of planetary

systems.

Here we outline some of the main types of feedback:

Photoionization - Energetic photons (> 13.6 eV) emitted by massive stars dissociate molecular hydrogen and ionize HI into HII, creating a HII region around the star that expands as the process continues. The outer edge of this HII region is called the ionization front, and its expansion slows as the volume of the region increases. A shell of compressed matter is produced outside of the ionization front. In the situation where a HII region expands to the edge of the molecular cloud the pressurised gas can burst out in a champagne flow.

Winds - For highly luminous stars (O and post-main-sequence OB types) radiation pressure at the surface of the star is strong enough to overcome gravity and lifts the outer layers away as stellar winds. The winds are then accelerated outward into the local environment.

Radiation pressure - Photons emitted by stars transfer energy and momentum to the material of the surrounding cloud. Krumholz & Matzner (2009) find that for very massive star clusters, radiation pressure can overtake ionisation as the dominant mechanism in the initial expansion of HII regions.

Jets - Sometimes, as a result of interaction between a star and its accretion disc, a magnetic field is produced which ejects outflows above and below the rotation axis of the star. Jet velocities can reach $\sim 100 \, \mathrm{kms^{-1}}$ and produce bowshocks that spread out into the surrounding environment. Frank et al. (2014) discuss how jets and outflows drive turbulence in the surrounding cloud.

Supernovae - After a few Myrs the most massive stars reach the end of their lives and explode as supernovae. This leads to the release of an immense amount of energy as well as the ejection of the remaining outer layers of the star. The

resulting shock impacts the surrounding cloud and creates a dense, expanding shell.

Many of these types of feedback only or predominantly occur from massive O- and B-type stars, which means that, although they are the least numerous, they have the greatest effect on the local environment and thus the greatest effect on the evolution of their cluster.

Calculations by Whitworth (1979) predict that a GMC can be dispersed by massive stars if as little as 4% of the gas forms stars following a field star IMF. The ionization and dispersal of gas in the molecular cloud due to feedback can bring star formation in that region to an end. Dale, Ercolano & Bonnell (2013) compare the effects of stellar winds and ionization, and conclude from their simulations that stellar winds have a much smaller effect on sweeping away gas than photoionization, and that photoionization can be almost solely responsible for reducing the star formation efficiency[1] (SFE), hindering further star formation.

1.1.5 Residual gas expulsion

The typical star formation efficiency across a GMC is less than 10%, i.e, less than 10% of the material in a GMC will go into newly forming stars (Clark et al. 2005), and on the scale of a cluster there is a strong dependence on the initial energy of gas in the region (Clark, Bonnell & Klessen 2008). For an embedded cluster held together by the combined gravitational potential of both stars and gas (in virial equilibrium, see section 1.2.3), the gas will contribute the majority of the binding mass. So once excess gas begins to be expelled from the cluster, either driven out by stellar

---

[1]Star formation efficiency is essentially the proportion of molecular gas in a star forming region that is used in the formation of new stars.

winds or by the first supernovae, a large amount of mass is lost from the system, often throwing the cluster out of virial equilibrium and thus the cluster is likely to become unbound (Bastian & Goodwin 2006), though the cluster core may remain bound (Kroupa, Aarseth & Hurley 2001). This process is known as "residual gas expulsion" and has been a popular hypothesis used to explain the "infant mortality" phenomena, that there are a greater number of young clusters observed than old and so many must die young. The difference in numbers of young and old clusters has been observed in both Galactic clusters (Lada & Lada 2003) and extragalactic (Bastian et al. 2005; Fall, Chandar & Whitmore 2005).

1.1.6   Triggering

Feedback may not necessarily cause star formation to cease. Elmegreen & Lada (1977) proposed a chain reaction-like mechanism for star formation where feedback from a group of newly formed stars creates an ionizing shock front, which compresses material elsewhere in the molecular cloud and triggers further star formation. This new group of stars can begin the process over again in a chain reaction, until the cloud is dispersed and a complex of stars is left.

This model can explain the variety of ages and kinematics seen in large groups of stars, such as OB associations (see Section 1.3.1), as via a triggered formation scenario small subgroups will be formed in bursts. However, according to Dale, Ercolano & Bonnell (2013), feedback likely disrupts star formation to a greater extent than it contributes.

1.2 Star Clusters

Star clusters are groups of stars which have been formed in close proximity within the same parent molecular cloud in a relatively short amount of time, and which are bound together by their mutual gravity. Their motion relative to each other is predominantly determined by their mutual gravitational attraction, but relative to the wider environment their group motion is typically much larger. These clusters are traditionally thought to form inside the dense cores of GMCs (Lada & Lada 2003), though recent investigations have uncovered more complex structures within GMCs and have found that interstellar filaments play a crucial role in star formation (André et al. 2014). Analyses of the structure of gas clouds in the Taurus region (Hacar & Tafalla 2011; Hacar et al. 2013) have indicated that dense star forming cores are produced when velocity-coherent filaments of sufficient mass fragment. Hacar et al. (2016) looked at radial velocities of newly formed stars in the Orion A cloud and found striking similarity between the kinematics and spatial structure of the young stars and the dense cores of the gas cloud, suggesting that groups of stars inherit their structure from their parental gas.

In their earliest stages (< 2 - 3 Myrs) clusters are embedded in their parent GMC, hence the term 'embedded cluster', and are obscured by interstellar dust, which made observing the early stages of star and cluster formation a difficult endeavour until the advent of infrared astronomy. After a few Myrs clusters will have either depleted or dispersed all their molecular gas by feedback processes and star formation will finish.

Clusters are often referred to in the literature as one of four main types:

Embedded clusters - Clusters up to a few Myrs in age which are still enveloped in the molecular gas of their parent cloud (Fig 1.4a) and are thus best observed in the infrared. Only the most massive cluster members will evolve onto the main sequence in this time, while less massive members will still be pre-main

sequence stars. Star formation may continue during this stage until the gas surrounding the cluster is dispersed by feedback (see section 1.1.4)

Exposed young clusters - Clusters where the molecular gas in their immediate vicinity has been dispersed, allowing the cluster to be observed in the visible (Fig 1.4b). These clusters are still associated with their parent cloud and have begun to evolve dynamically. Because of their youth, it is difficult to tell whether clusters this young are gravitationally bound based simply on their existence, and measurements of velocity are often needed.

Open clusters - Clusters no longer associated with molecular gas and are of an age (typically > 10 Myrs but can be up to 10^4 Myrs) at which the members have experienced significant dynamical interactions for it to be clear that they are in virial equilibrium (Fig 1.4c). If the cluster was not in virial equilibrium then it would have started to disperse by this point in time.

Globular clusters - Much older objects than the previous types (many Gyrs old), these clusters tend to exist in the halos of galaxies on elliptical orbits around the galactic centres. They are made up of hundreds of thousands of old stars, are much more massive than most open clusters and have become dynamically relaxed, hence their spherical or 'globular' shape (Fig 1.4d).

The evolution of a cluster depends heavily on whether it is gravitationally bound or not. For a cluster to be bound, the gravitational attraction between the member stars and molecular gas within the cluster must be greater than the internal kinetic energy of the cluster, i.e the cluster has negative total energy. Though it is still possible for individual stars to escape as runaways via binary interactions, a bound cluster will not disperse unless disturbed by external forces. When a cluster's total energy is positive, i.e its internal kinetic energy is greater than its gravitational potential energy, the cluster will expand, weakening the gravitational attraction fur-

Figure 1.4: *Top left* : The embedded cluster RCW 38 (< 1 Myr) in the Vela constellation. Image Credit: ESO. *Top right* : The young cluster NGC 6231 (~ 3 Myrs) in the constellation of Scorpius. Image Credit: NASA / CXC / University of Valparaiso / M. Kuhn et al / WISE / JPL. *Bottom left* : The star cluster NGC 299, an open cluster aged ~ 25 Myrs in the Small Magellanic Cloud. Image Credit: NASA / ESA / Hubble. *Bottom right* : The Messier 80 globular cluster. Credit: Hubble Space Telescope / NASA.

ther until the cluster has eventually dissipated. The majority ($> 90\%$; Lada & Lada 2003) of young or embedded clusters do not survive to become bound open clusters. This is because clusters can lose up to $\sim 80\%$ of their members following gas expulsion (Lada, Margulis & Dearborn 1984; Kroupa 2002) so only the most massive embedded clusters subsequently remain bound.

1.2.1 Cluster structure

Since stars form in the densest regions of their parent GMCs, and the GMCs are themselves highly substructured in sheets, filaments and cores, it is not surprising that newly formed stars have been found to be distributed with similar substructure (Larson 1995; Cartwright & Whitworth 2004; Sánchez & Alfaro 2009; André et al. 2010) and exhibit fractal patterns, i.e the structures are self-similar on a range of scales. In order to assess this substructure a number of statistical measures have been developed, one in particular is the Q parameter (Cartwright & Whitworth 2004) which quantifies and distinguishes between fractal substructure and smooth radial density gradients. Parker et al. (2014) test the Q parameter on the results of a series of N-body simulations and observed that a region with Q < 0.8 must be dynamically young, since it is not well mixed enough to have erased its original substructure, while a region with Q > 1.5 has evolved toward a smooth radial profile. Wright et al. (2014) applied this parameter to the Cygnus OB2 association and measured Q= 0.34, which despite possible biases strongly indicates that the region is highly substructured and has been since its formation. That being said there are examples of young clusters ($\sim$1 Myr) with smooth radial profiles, such as the Orion Nebula Cluster and IC348 (Hillenbrand & Hartmann 1998; Cartwright & Whitworth 2004).

It has been shown that young clusters can erase their substructure within a few crossing times (Scally & Clarke 2002; Goodwin & Whitworth 2004). Gravitational

interactions between stars leads to the transfer of kinetic energy, and the cluster relaxes into a smooth distribution. Kinetic energy can also be removed from the cluster via dynamical ejections. This leads to a simple hypothesis that if all star forming regions are born with considerable physical substructure, those that are bound will undergo rapid mixing to erase this structure, while those that are unbound will expand but preserve their substructure. The rate at which young clusters will erase their substructure depends on their velocity dispersions, the higher the velocity dispersion the longer the substructure will be preserved (Goodwin & Whitworth 2004). Therefore it is possible for the structure of clusters of the same age to evolve at different rates, depending on their boundedness. But for older open clusters and globular clusters their initial structure will have long since been erased.

1.2.2 Mass segregation

In older open and globular clusters, mass segregation has been observed for a long time (Elmegreen et al. 2000) and is thought to be a consequence of energy equipartition, i.e. where as the cluster evolves and the member stars interact and transfer energy through two-body encounters, the kinetic energy of stars becomes more equal ($v \propto \frac{1}{\sqrt{M}}$) and thus massive stars have smaller velocities. With smaller velocities, such stars are expected to sink towards the centres of the cluster's gravitational potential well, thereby becoming more concentrated.

Bonnell & Davies (1998) calculated that dynamical mass segregation would need to take place over a cluster relaxation time, which can be written as

$$t_{rl} = \frac{\langle v^2 \rangle^{3/2}}{15.4 G^2 m \rho \ln \Lambda} \tag{1.4}$$

where ρ is the local density, $\langle v^2 \rangle$ the average square velocity of cluster members, m the mean stellar mass and $\Lambda = 0.4N$ for a homogenous distribution of equal mass

stars (Spitzer 1987). The relaxation time can be interpreted as the time required for stars in a cluster to have undergone sufficient two-body interactions to have achieved energy equipartition. Therefore, if mass segregation is a consequence of energy equipartition, mass segregation should not be seen in clusters younger than the relaxation time of the cluster. If massive stars were found to be located preferentially towards the center of a young cluster then their mass segregation must be primordial (due to the star formation process) and not dynamical. However, later studies have challenged this theory. Allison et al. (2009) have shown that mass segregation of the most massive stars can take place on very short timescales, given dynamically cool initial conditions. The study by Wright et al. (2014) concluded that the Cygnus OB2 association is not mass segregated despite being highly substructured, indicating that the star formation process does not always produce mass segregation. Ascenso, Alves & Lago (2009) also argue that observations of mass segregation can be explained by incompleteness due to crowding in the cores of clusters.

1.2.3 The Virial Theorem

Originally presented in 1870 by Rudolf Clausius in a lecture titled 'On A Mechanical Theorem Applicable To Heat', the virial theorem describes a relationship between time-averaged kinetic and potential energies for a stable mechanical system of N particles, systems found in thermodynamics, quantum mechanics, and astrophysics. The theorem can be applied to star clusters and molecular clouds to assess their dynamical state, namely, whether they are gravitationally bound or unbound.

Within a system of bodies moving in a gravitational field, the distances between the bodies changes, changing the gravitational force they apply on each other and thus changing their energies and speeds. However, after a sufficient time has passed for many of these changes to occur, the distribution of speeds within the whole sys-

tem reaches an equilibrium, where a change in speed of one body is accompanied by a change elsewhere, maintaining the distribution. We say a system in such a state is dynamically relaxed.

The expression of the virial theorem for a dynamically relaxed mechanical system with kinetic energy K and potential energy U is

$$0 = 2\langle K \rangle + \langle U \rangle \tag{1.5}$$

In the literature, it is also presented in forms with the system's total energy $E = K + U$,

$$E = -\langle K \rangle = \langle U \rangle / 2 \tag{1.6}$$

from which can be inferred the interesting consequence that a system in virial equilibrium must have negative total energy.

We now look at applying this theorem specifically to a group of stars. If we approximate the cluster as a uniform density sphere of radius R, and assume the movements of stars are random and thus the averages of the velocity components are isotropic, the virial theorem gives us

$$M = 5\frac{R\langle v_r^2 \rangle}{G} \tag{1.7}$$

where $\langle v_r^2 \rangle$ is the average square radial velocity of the stars and G is the gravitational constant. This form is known as the virial mass equation. It allows us to estimate a cluster's total mass using only the cluster radius R and average square velocity in one dimension. The average of radial velocities $\langle v_r \rangle$ can be determined from a sample of stars in the cluster. Essentially, we are determining the mass from the effect of gravitational attractions on the stars' internal motions, so as the motions, and thus $\langle v_r^2 \rangle$ increase, so does the virial mass.

This method is not without its limitations, however.

- To apply this method we have to assume that the system is dynamically relaxed, but we cannot be sure based on any observations we can make. We expect that multiple body systems will tend to a steady state over one dynamical timescale, so this assumption becomes more reasonable the greater the age of the system in question.

- The virial/gravitational radius R (or r_g) of a system is not directly measurable, but is usually derived from the half-mass radius r_h, where $r_h/R \approx 0.5$ (Binney & Tremaine 1998). In Spitzer (1987), it is shown that the virial theorem gives

$$U \approx -0.4 \frac{GM^2}{r_h} \tag{1.8}$$

for a system with spherical symmetry.

Even then, in order to measure a radius, it is necessary to define a centre. To calculate the most intuitive centre, the cluster's centre of mass, we require knowledge, or further assumptions, about the masses of the individual stars and their 3D positions. However, our knowledge is often unsatisfactory for computing an accurate centre of mass, so other estimators have also been developed to suit the available data. A cluster's luminosity density can be used to derive a centre, though this is still made difficult due to observational effects such as crowding.

- The form for potential energy U assumes that the cluster can be approximated as spherical and of uniform density. We would expect in most cases that cluster density increases towards the centre rather than being uniform. The virial mass equation can be modified for the application of different density models. In Zwart, McMillan & Gieles (2010) and Gieles, Sana & Zwart (2010), it is explained how the virial mass may be expressed as

$$M = \eta \frac{\sigma_{dyn}^2 r_{eff}}{G} \tag{1.9}$$

where $\eta = \frac{6r_{vir}}{r_{eff}}$ is a parameter that depends on the density profile of the system, $\sigma_{dyn}^2 = \frac{1}{3}\langle v^2 \rangle$ is the system's velocity dispersion assuming symmetry and r_{eff} is the effective radius (half-light radius). The value of η depends upon the parameters of the density profile. In a Plummer (1911) profile $\eta \approx 10$, for an Elson, Fall & Freeman (1987) (EFF) profile, the value of η drops sharply for shallow density profiles $\eta \leq 9$, and is very sensitive to the effect of mass segregation. The King profiles (King 1962; King 1966), though different in shape to EFF, produce similar $\eta \approx 9$.

1.3 OB Associations

OB associations are groups of young stars that are associated by a common motion through space (Ambartsumian 1947). They were initially identified only by the brightest and most massive O and B-type member stars, hence 'OB' association. As early as 1914, (Kapteyn 1914) had mapped out the distribution of 'helium stars' (now obsolete synonym for B-type star) in the Galactic plane, which Eddington (1914) also discussed, and Kapteyn (1918) then commented on the grouping of such stars around the Orion nebula. But it was not until Ambartsumian (1947) that the term 'association' was first coined. Such associations typically span a much larger volume in space than open clusters, tens or hundreds of parsecs across, so Ambartsumian (1955) realised that these groups had typical densities $< 0.1 M_\odot$ pc^{-3}, less than the density for which a cluster is stable against disruption from Galactic tidal forces. He realised that this implied that associations had to be young objects, less than a few tens of Myrs old and thus considerably younger than the Galaxy. This was one of the first demonstrations that star formation is still occuring in the present epoch. This hypothesis was supported by the discovery by Blaauw (1952) of the expansion of the Perseus OB2 association.

In his review, Blaauw (1964) described the knowledge of faint-star membership as being " in a most unsatisfactory state". This is due mostly to the nature of associations, having low density and being spread across large areas of sky, which makes it very difficult to identify faint members against the galactic background. Also, at this time, kinematic data was limited and so stars were considered association members based on luminosity position rather than motion or parallax.

The Hipparcos census (1989-1993) (Perryman et al. 1997) provided high precision positions and proper motions for over 90 000 stars, which allowed fresh investigation of nearby associations (see Fig. 1.5), and in particular, studies which aimed to identify which stars are members of which associations,e.g (de Zeeuw et al. 1999), and the associations' distances. However, these are only the most massive members and a small fraction of the total stellar population, assuming it follows a classic IMF. Pre-Gaia, much was unknown about the population of low-mass stars in associations. To what extent do their positions and velocities correlate with those of the OB stars, how do they evolve, and which processes are responsible for this evolution? These are all questions that hopefully can be addressed with Gaia data.

1.3.1   Origins of associations

Because Ambartsumian (1947) realised that associations are not dense enough to resist disruption from galactic tidal forces, associations are thought to be gravitationally unbound and many hypotheses have since been proposed to explain their origins. In a following paper Ambartsumian (1955) suggested that associations were formed from the expanding, disintegrated remains of massive, dense bodies. A similar hypothesis was put forward by Opik (1953) who proposed that the expanding shell of a supernova explosion could compress dust to create an association of stars, and then Oort (1954) suggested the same could happen with an expanding HII region
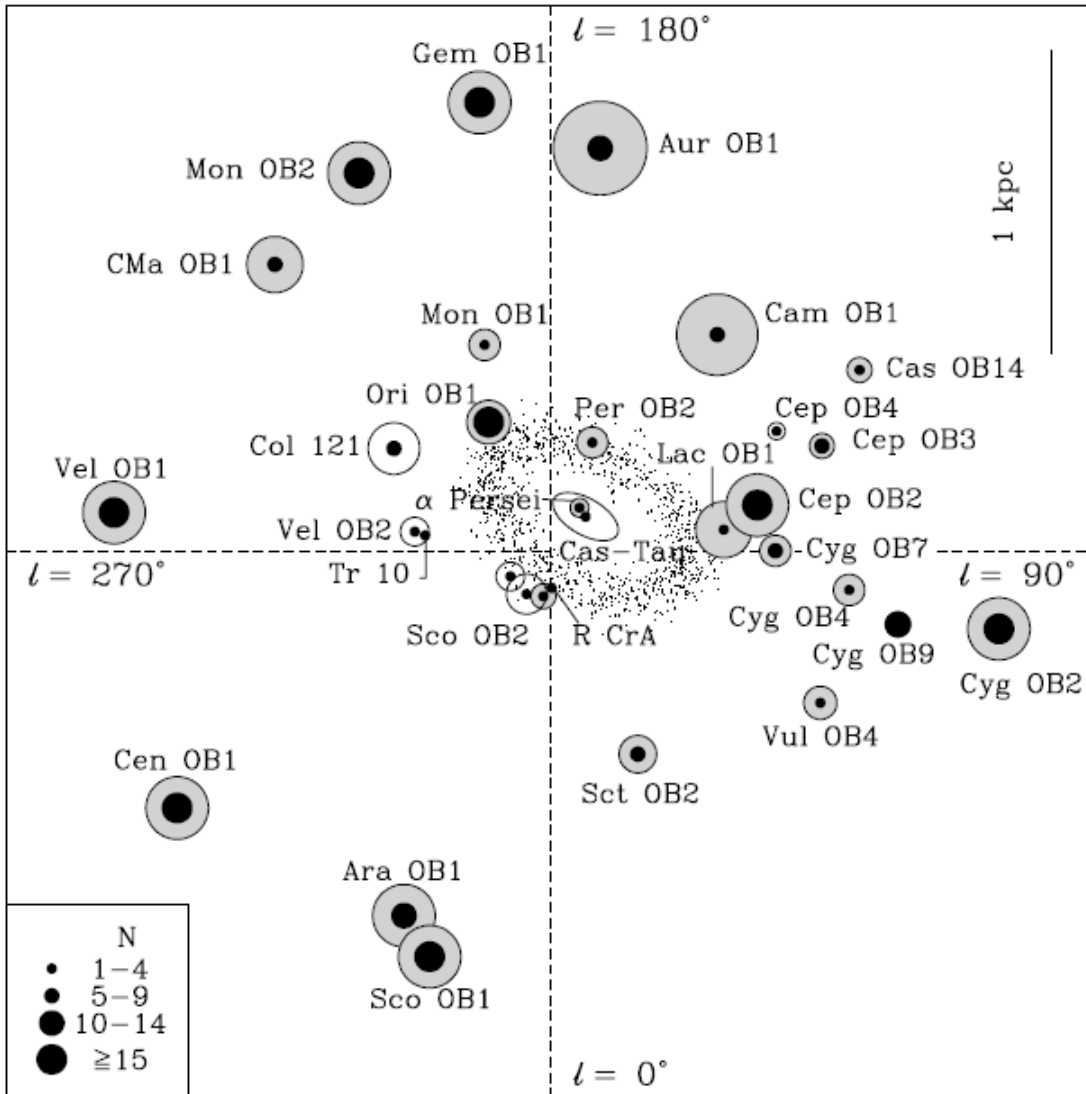
Figure 1.5: Pre-Hipparcos positions, projected onto the galactic plane, of OB associations within 1.5 kpc of the sun (de Zeeuw et al. 1999). The size of the outer circles is proportional to their projected dimensions, while the size of the central dots indicates the number N of stars with luminosity $> M_V \sim 5$ mag (Humphreys 1978). The distribution of small dots indicates the Gould Belt.

rather than a supernova. The common idea behind these theories being that, since associations are expanding groups of stars, they must have formed from expanding clouds of gas, so the question is what phenomena produces the expanding motion?

The rejection of a need for associations to form from unbound clouds was first considered by von Hoerner (1968) who proposed that the massive O and B type stars would sweep away the interstellar dust around them, and from this loss of mass, the newly formed stars would become gravitationally unbound and the group would begin to expand. This theory of residual gas expulsion was first explored mathematically by Tutukov (1978) and then Hills (1980), who estimated that the loss of as little as 10 - 15% of a young cluster's mass by gas expulsion would be sufficient to unbind it. Duerr, Imhoff & Lada (1982) provided support for this scenario in their study of the λ Ori OB and T association, which is located in a HII region surrounded by a shell of dust. They concluded that the massive stars had indeed swept away the remaining dust and left a unbound group of stars. N-body simulations have been used to study the degree to which the SFE and the size of the cluster affects how likely the cluster is to remain bound after gas expulsion (Kroupa, Aarseth & Hurley 2001; Fellhauer & Kroupa 2005; Pfalzner & Kaczmarek 2013). Such models predict that, unless the SFE of a cluster is relatively high (> 0.3), they will become unbound and radially disperse.

At the time of the review by Lada & Lada (2003) evidence was such that the expansion of young clusters via gas expulsion offered the best explanation for how stars formed and dispersed into the field population, and that OB associations were a midway stage in this evolution where stars still retained their group motion but were unbound and dispersed over a greater volume. However, studies making use of the recently released Gaia astrometric data have produced evidence that questions this theory. Wright & Mamajek (2018) analysed the dynamics of the Scorpius-Centaurus OB2 association and found that it did not display the radial expansion pattern expected if the association had been formed as a more compact cluster (or

clusters). Rather, they concluded that the association was most likely formed in multiple highly-substructured subgroups, across the area that it now occupies, and in multiple star forming events, as evidenced by the age distribution found by Pecaut & Mamajek (2016). Ward & Kruijssen (2018) examine kinematic parameters of 18 nearby association with > 100 identified members each and concluded that none of these associations showed signs of having began as dense clusters. The results of these more recent kinematic studies suggest that associations are made up of many substructured groups that share an associated motion, and that their substructure indicates they could not have formed as single dense clusters.

Bressert et al. (2010) investigated the environments YSOs in the solar neighbourhood form in and found that they exist in groups of a wide range of densities. Only a small fraction were found to have formed in dense clusters. This lead to the hypothesis that associations are made up of a continuous distribution of stars at both low and high density, such that high-density regions collapse to form bound clusters while low-density regions disperse as the wider, unbound population of the association (Kruijssen 2012). This, along with the evidence that groups of stars form with substructure (Larson 1995; Cartwright & Whitworth 2004; Sánchez & Alfaro 2009; André et al. 2010), questions the older monolithic cluster formation model.

This evidence perhaps better supports a triggered formation scenario, which would explains why subgroups of star complexes are found to be of different ages (Blaauw 1964), and accounts for star formation within the core of the cloud, not only at the edge and offers a mechanism by which associations may be produced from gravitationally bound GMCs (Elmegreen & Lada 1977; Blitz & Thaddeus 1980).

Triggered star formation has gained recent interest thanks to new studies of OB associations. Krause et al. (2018) analysed the interstellar medium (ISM) around the Sco-Cen OB2 association and suggest a formation mechanism where a supperbubble of hot gas created by feedback from new stars in one region triggers the collapse of a dense cloud elsewhere, in a "surround and squash" scenario, creating the multiple

subgroups of different ages apparent in the association.

The hypotheses for the origins of associations can be split into two main categories;

Expanding clusters - The majority of stars are born in clusters embedded within molecular clouds, but most of these, Lada & Lada (2003) claim as many as $\sim 90 - 95\%$, become unbound following residual gas expulsion and expand radially. The common motion of the association is inherited from the early stage spent as a gravitationally bound cluster.

Born across unbound GMCs - Unbound, turbulent GMCs form stars in subgroups among sheets and filaments of gas compressed by turbulence with initial spacing larger than that typical of embedded clusters (Clark et al. 2005). The OB association would thus form initially spread over a large volume and is gravitationally unbound to begin with, rather than having expanded from a smaller volume, and the common motion of the association is inherited from the motion of the GMC itself as well any spatial and kinematic substructure.

These two possible origins can be distinguished observationally by looking for evidence of expansion in an association. If an association is expanding radially from a central point with an expansion timescale consistent with the age of the population, it would suggest that it was formed as a dense cluster. Such expansion would be expected to be isotropic (Baumgardt & Kroupa 2007). If the expansion trends do not trace back to a dense configuration within the lifetime of the population, or the trends are significantly anisotropic, it would indicate that the population initially formed with structure over a large volume.

1.3.2   Determining membership of OB associations

A star's membership of an association can be determined by how well its motion correlates with the motion of other members. Even though OB associations are thought to be gravitationally unbound, their internal motions are of the order of only a few kms^{-1}, much smaller than the group velocity through space, and so the proper motion of the group's members on the plane of the sky will seem to converge to a point (Jones 1971; De Bruijne 1999; de Zeeuw et al. 1999). Because of this, the 'convergent point method' was the classical technique for determining association membership, before astrometric data became more precise. Once a convergent point is determined, a membership probability for a star can be calculated from how close a star's motion will bring it to the convergent point. This method does not eliminate contaminants, however, as non-members with a small velocity component tangential to the direction toward the convergent point can have a significant membership probability. It is useful to compare membership probabilities produced by multiple methods.

Another method of producing membership probabilities is the so-called 'Spaghetti method' (Hoogerwerf & Aguilar 1999; de Zeeuw et al. 1999) which uses positions, parallaxes and proper motions to construct cylinders (spaghetti) of membership probability in 3D velocity space for each star. The intersection of these cylinders will be the group velocity. The cylinder's axis is oriented in the line-of-sight direction, since it is the direction in which we have no velocity information (radial velocity). Once we have made spaghetti for all our membership candidates, we construct a sphere of radius

$$R_s = \sqrt{\sigma_{int}^2 + \sigma_{median}^2} \qquad (1.10)$$

where σ_{median} is the median error of the tangential velocities and σ_{int} is the internal velocity dispersion. The fraction of a spaghetti that lies within this sphere is the star's membership probability.

The membership lists of OB associations studied in de Zeeuw et al. (1999) are produced by intersecting membership lists using each of the above methods on stars either previously classified as O or B type or later-type stars at the right distance to belong to an association. Early-type stars are rarer than late-type stars and so the field star contamination rate is considerably lower.

With the huge improvements to precision of kinematic data available from new surveys such as Gaia, recent studies have been able to effectively select members by defining areas in proper motion space combined with parallax cuts (Damiani et al. 2019), or by using agglomerative clustering algorithms to allocate stars with similar kinematics into groups (Cantat-Gaudin et al. 2019c).

1.4   Confirming youth in stars

Young stars which have yet to converge onto the main sequence exhibit some different properties than main-sequence stars, some of which can be identified photometrically or spectroscopically. These properties are especially useful for separating young cluster members from older stars in the background.

Surface gravity indicators -   Surface gravity is a useful way of separating giants from cluster main sequence and pre-main sequence stars. Since giants are greatly inflated, their surfaces are much further from their center of gravity, hence experience a smaller surface gravity. Damiani et al. (2014) uses a gravity index derived from the flux ratio between low-g and high-g features in the 6750-6780 Å region, which is used to distinguish between giants, main-sequence and PMS stars.

Surface Lithium abundance -   Despite composing only a tiny fraction of the interstellar medium, lithium can be observed in stellar atmospheres, using in

particular the Li I absorption line at 6708 Å. Low-mass ($< 1.2\,\mathrm{M_\odot}$) PMS stars are not hot enough to burn their lithium until they begin to contract onto the main-sequence, at which point surface lithium begins to deplete at a rate dependent on its mass. Therefore the presence of lithium can be used as an identifier of youth in PMS stars. Some studies of young clusters (Jeffries et al. 2014; Sacco et al. 2017) have used a large EW(Li) as their principal criterion for finding young low-mass cluster or association members.

X-ray luminosity -   Due to magnetic activity in low-mass PMS stars, their X-rays are $10^1 - 10^4$ times more luminous than those of main sequence stars (Preibisch & Feigelson 2005). This makes X-ray observations especially useful for separating young cluster members from backgrounds of older field stars e.g (Wright & Drake 2009). Modern X-ray observatories have a small field of view however, and therefore are not well suited to wide-area studies of nearby OB associations.

Colour magnitude diagrams -   Since PMS stars are more luminous for their effective temperature than main-sequence stars, in a plot of colour versus absolute magnitude they will appear in a different place. An isochrone can be placed alongside stellar populations on colour-magnitude diagrams (CMDs) to show where PMS stars of a given age are likely to be found. For stars undergoing pre-main sequence contraction, their luminosity changes rapidly, meaning their CMD location is potentially a precise indicator of age. However, plotting with observed (apparent) magnitudes means bright, distant stars can be located in the same place on a diagram as nearer, fainter stars. With distance information one can calculate absolute magnitudes, which separates different types of stars more effectively. There are also many other physical factors that influence luminosity / magnitude and effective temperature / colour, including binarity, extinction, non-uniform reddening and the

presence of disks and accretion, all of which need to be considered when estimating stellar ages from isochronal position. Also, multiple models do exist (Baraffe et al. 1998; Siess, Dufour & Forestini 2000; Tognelli, Prada Moroni & Degl'Innocenti 2011; Baraffe et al. 2015) and vary in their treatment of opacity, atmospheres, etc.

Variability - PMS stars are also known to exhibit photometric variability, i.e. their brightness varies during the PMS stage of their evolution. This variability can be due to a number of reasons. T Tauri stars (TTSs), low-mass ($< 2M\odot$) PMS stars which exhibit variability, can be split into two classes; classical TTSs which accrete material from their circumstellar disks, causing variability, and weak-line TTSs which do not show signs of accretion but whose variability is due to a non-uniform distribution of spots on their surface (Herbst et al. 1994; Bhardwaj et al. 2019). More massive PMS stars ($2M\odot < M < 8M\odot$) known as Herbig Ae/Be stars also show variability due to obscuration from circumstellar dust (Herbst et al. 1994). Variability can be detected by taking photometric observations over time and plotting a light curve (time vs apparent magnitude), the amplitude and period of which can indicate the nature of a star's variability (Samus' et al. 2017).

These and other methods of selecting stars of similar ages are discussed in detail in reviews by Soderblom (2010) and Soderblom et al. (2014).

1.5 The Gaia Mission

The European Space Agency's (ESA) astrometric mission Gaia (originally Global Astrometric Interferometer for Astrophysics) was proposed by Lennart Lindegren

and Michael Perryman in 1995, and aims to collect precise, to an as yet unmatched degree, measurements of the positions, parallaxes and proper motions of over a billion stars complete to 20th magnitude (Gaia Collaboration et al. 2016b; Lindegren et al. 2016). Its design and space environment allows sensitivity, accuracy and sky coverage impossible to obtain with ground-based facilities. Its predecessor, the *Hipparcos* satellite, led the way to significant advancement of our knowledge of the structure and evolution of stars and the dynamics of groups of stars. Gaia is capable of detecting much fainter sources than *Hipparcos* and making measurements of much greater precision. It is set to provide the data needed to answer questions about the structure and dynamics of the Galaxy, star formation history, binary and multiple star systems, stellar evolution, exoplanets and many other topics besides.

Gaia was launched in December 2013 and after a period of performance verification, began operations in the summer of 2014. Data processing and calibration is managed by the Gaia Data Processing and Analysis Consortium (DPAC).

1.5.1   Measurement

The Gaia satellite's 'payload' (the set of on-board instruments) is built onto a torus-shaped bench (Fig. 1.6) made of silicon carbide, on which the telescopes and instruments are mounted. In order for Gaia to observe and take astrometric readings across the whole sky the satellite spins slowly on the rotation axis (Fig. 1.6) and measures the time taken for objects to cross its field of view, which is the so-called "scanning space astrometry principle" (Lindegren & Bastian 2010) employed successfully in the preceding *Hipparcos* mission. The satellite's spin axis is also controlled to precess slowly, so that the great circles traced by the two fields of view move while maintaining a slight overlap, thus scanning the entire sky repeatedly over the course of the mission.
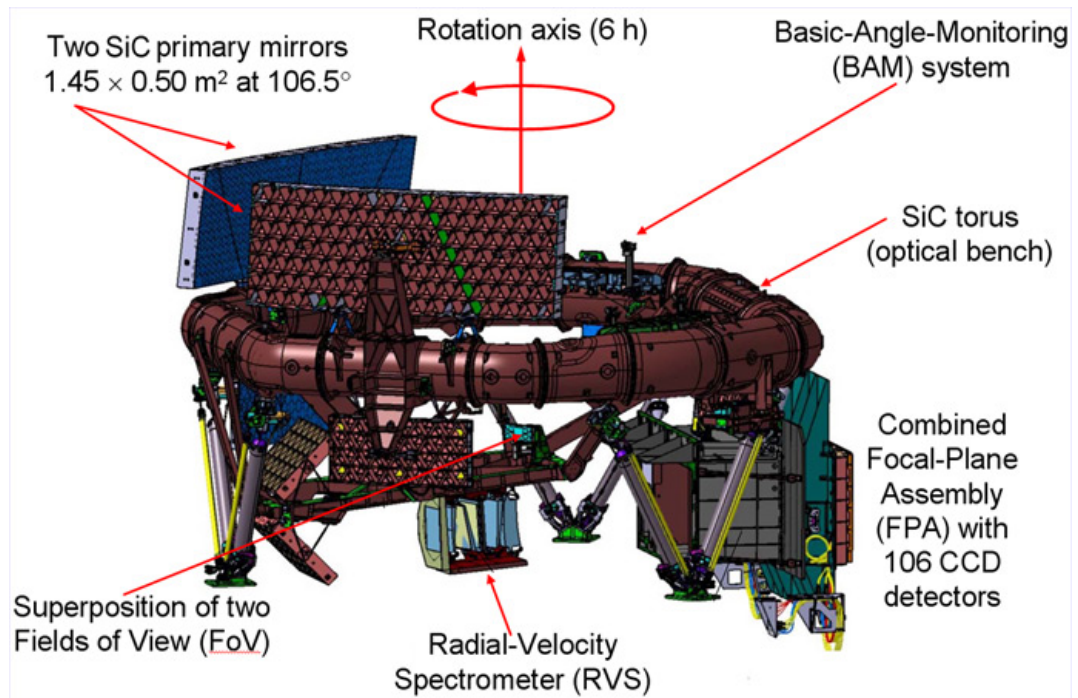
Figure 1.6: Diagram showing the two mirrors and instruments mounted on the torus-shaped optical bench. (Image from EADS Astrium.)
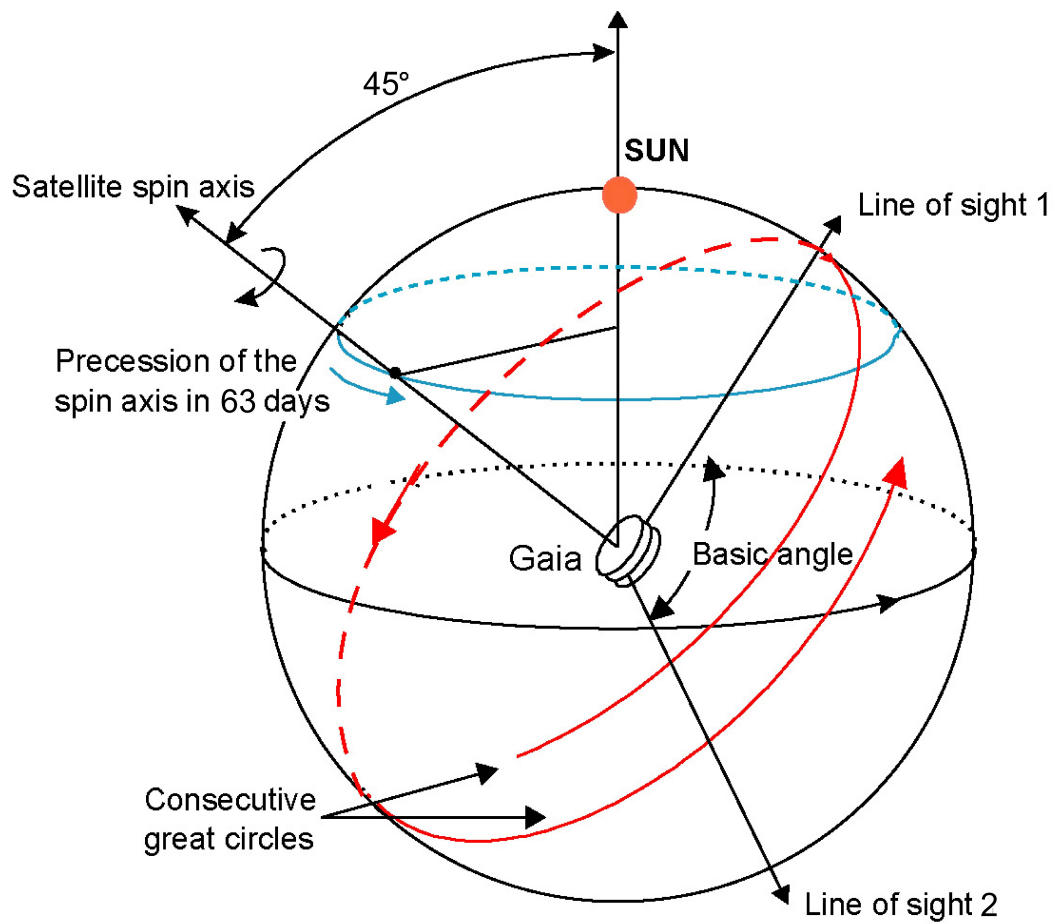
Figure 1.7: Diagram showing the orientation of the Gaia satellite's spin axis, lines of sight and great circles, which allow full sky coverage. (Image credit: ESA)

Gaia makes observations with a pair of identical 'three-mirror anastimatic' telescopes, which point in directions separated by the 'basic angle' $\Gamma = 106.5°$, meaning that the satellite has two lines of sight (Figs 1.6, 1.7). Knowing the basic angle and the observation times of a source in each field of view allows calculations of angular separations between objects, which is necessary for measuring parallaxes. This angle is chosen as the optimum basic angle to maximise sensitivity to parallax proportional to $\sin(\eta)\sin(\Gamma)$ where η is the angle between the Sun and the satellite's spin axis; (see Gaia Collaboration et al. 2016c), whilst maximising the accuracy with which the positions of stars on the great circle can be derived and avoiding sunlight entering the telescopes. Light entering the telescopes is reflected by a series of silver coated mirrors, and merged into a common path before reaching the focal plane (Fig 1.8), a mosaic of 106 CCD detectors each with a resolution of 4500×1966 pixels, giving a total of 938 million pixels. These CCDs are operated in 'time-delayed integration' (TDI) mode, so that they can collect charge whilst the objects move along the focal plane as a resut of the satellite's spin. With 938 million pixels operating in TDI mode, many times more data is produced than can be sent back to Earth, so several reduction processes are employed on the satellite itself:

- Data is only read from within little 'windows' around objects of interest, and the excess is flushed. Windows are automatically assigned to objects of interest on board the satellite by video processing units (VPUs) attached to each of the seven rows of CCDs.

- Resulting linespread functions and spectra are compressed on board, making room for 2 to 2.5 times more data.

Because Gaia's measurement principle produces angular measurements by comparing the differences of the times taken for objects to cross each telescope's field of view, the basic angle Γ between the telescopes needs to be kept constant, as even the slightest variation can introduce significant systematic errors. So, in order to monitor
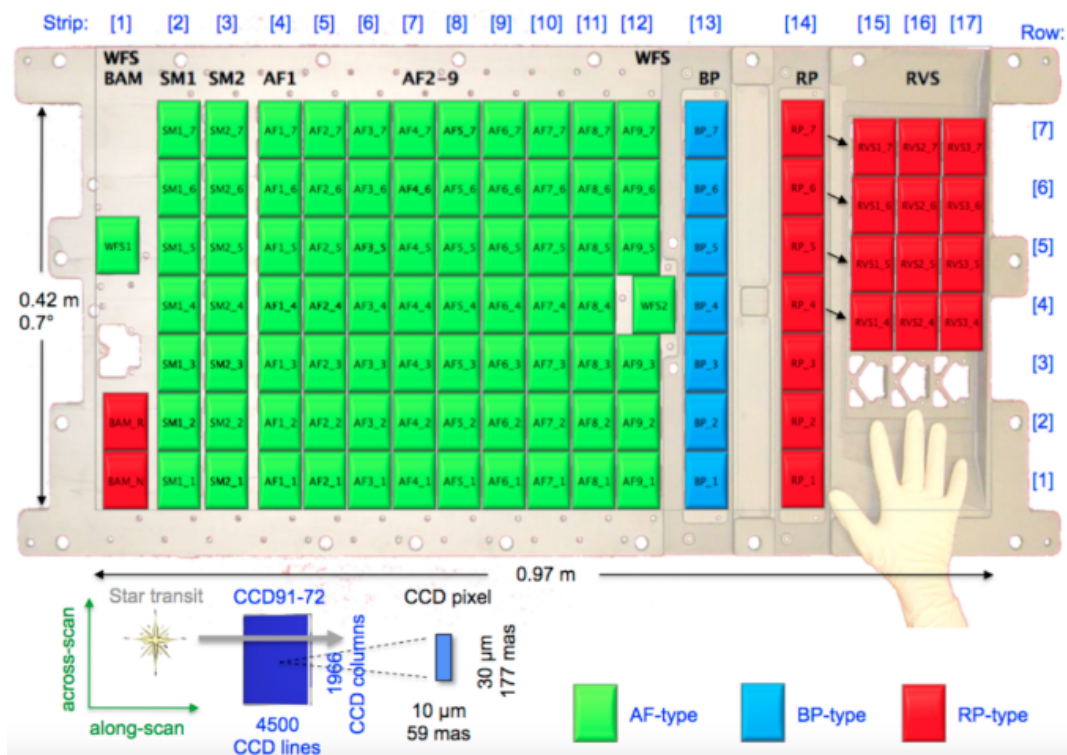
Figure 1.8: Schematic of the focal plane assembly (Gaia Collaboration et al. 2016b) with terminology indicated below.

and re-calibrate the basic angle, Gaia is fitted with an ultra-precise interferometric metrology system, the basic angle monitor (BAM) (Gielesen et al. 2012; Mora et al. 2014; Gielesen et al. 2017), which is able to measure displacements on the scale of picometers (10^{-12} m).

1.5.2 The astrometric solution

In order to take full advantage of Gaia's precision capabilities and produce a coherent set of astrometric data for observed sources, the astrometric core solution is applied during data processing. The astrometric core solution uses a series of physical and mathematical models (Fig 1.9) to simultaneously determine the astrometric parameters (positions, parallaxes and proper motions) for all sources at once (Lindegren et al. 2012; Lindegren et al. 2016; Lindegren et al. 2018a). The models incorporated aim to take into account the complex relationships between astrometric, photometric and spectroscopic data, as well as the celestial reference frame, instrument attitude and geometric calibration determined by the 'core solution' (Lindegren et al. 2012).

In DR1 the astrometric solution was calibrated on the Tycho-2 catalogue and so was only complete for sources in the TGAS subset. In DR2 however, the astrometic solution became self-calibrated and all five parameters (positions,parallax and proper motions) were available for the majority of sources.

1.5.3 Data Releases

1.5.3.1 DR1

The first data release (DR1) from Gaia was available from 14th September 2016, containing positions and Gaia (G) magnitudes for all sources with acceptable posi-

tional errors (1.14 billion), and parallaxes and proper motions for objects detected by both Gaia and either of Tycho 2 (TGAS - Tycho-Gaia Astrometric Solution, 2 million sources) or *Hipparcos.* In TGAS the astrometric solution depends on the availablilty of Tycho-2 positions, so the TGAS data set contains 2,057,050 sources with 5 astrometric parameters, while the secondary data set of non-TGAS sources contains 1,140,622,719 sources with only positions in DR1. All sources in the TGAS catalogue were treated as single stars initially, so astrometric effects from binary orbital motion are ignored. This and other source modelling errors contribute to the 'astrometric excess noise' parameter, which is the difference between the measured astrometry and the astrometric model. Many bright stars (Gmag $\leq$ 7) are missing from DR1, as the images of these sources are heavily saturated and the sparsity of objects at this magnitude makes calibration of the instrument configuration difficult (Gaia Collaboration et al. 2016a).

1.5.3.2   DR2

The second data release became available on the 25th April 2018, providing the full five-parameter astrometric solution (positions, parallaxes, proper motions) for 1.33 billion sources down to the limiting magnitude of $G = 21$. The astrometric solution for DR2 does not depend on *Hipparcos* or Tycho-2 positions, only Gaia data, making it entirely independent of preceding astrometric missions. It also provided red and blue passband photometry (G_{RP},G_{BP}) for 1.38 billion sources in addition to G magnitudes for all 1.69 billion sources. Mean radial velocities were also published for 7.2 million sources with $4 < G < 13$, effective temperatures (T_{eff}) for 161 million sources and luminosities for 77 million sources, as well as other data.

Gaia DR2 data is based on preliminary calibrations of less than two years of observations, and as such there are still a number of known systematic errors to

be taken into consideration. For example, Lindegren et al. (2018a) discuss a median zero-point offset of -0.029 mas in parallax, spurious parallax values caused by cross-matching issues and underestimation of uncertainties for bright $G < 13$ objects. Arenou et al. (2018) identify potential outliers in the data set and recommend a number of filters to clean samples before use.

1.5.3.3   Future releases

Due to delays the full third data release (DR3) is expected only by the second half of 2021, so it will be split in order to publish an early release in the third quarter of 2020. The early release will contain improved astrometry and photometry for objects from DR2 as well as results for quasars. The full DR3 catalogue will also contain object classifications, BP/RP spectra and mean radial velocities for certain objects.

The final data release for the mission does not yet have an official expected date of publication, but will consist of complete astrometric, photometric and radial velocity catalogues, source classifications, a list of exo-planets and more.

2   The Vela OB2 association

We now look at the region that my PhD work has focussed on, the Vela OB2 complex, and review the body of work that forms the context for the following chapters of this thesis.

2.1   Pre-HIPPARCOS

The first indication of an association in the Vela region was found by Kapteyn (1914), who identified 15 bright (V > 7) 'helium' stars (now known as B-type stars) as possible group members based on an investigation of proper motions. These stars, however, were spread over a large area on the sky ($219° \leq l \leq 272°$, $-10° \leq b \leq 3°$ in old Galactic coordinates) and Kapteyn was not convinced that their proper motions were enough to confirm the existence of a physical group. He added a hopeful comment that if radial velocities were known for most of the stars the nature of the group could be more confidently determined.

Later Blaauw (1946) gathered radial velocities for 12 of these 15 stars as well as introducing corrections to the proper motions. For the 9 radial velocity measurements with errors <3 kms^{-1} there was a wide spread in values. Thus Blaauw determined that these stars should not be considered a group. In his review "O associations in the solar neighbourhood" (Blaauw 1964) there is no mention of an association in the Vela region, though, de Zeeuw et al. (1999) point out that a group of bright stars centered on l = 230°, b = −10° is visible in Figure 3 of that paper (see Fig. 2.1).

In their investigation of the Vela X supernova remnant Brandt et al. (1971) comment on the proximity of Vela X and the pulsar PSR 033-45 to the object γ Vel, which we now know is a spectroscopic binary composed of a massive O star and a
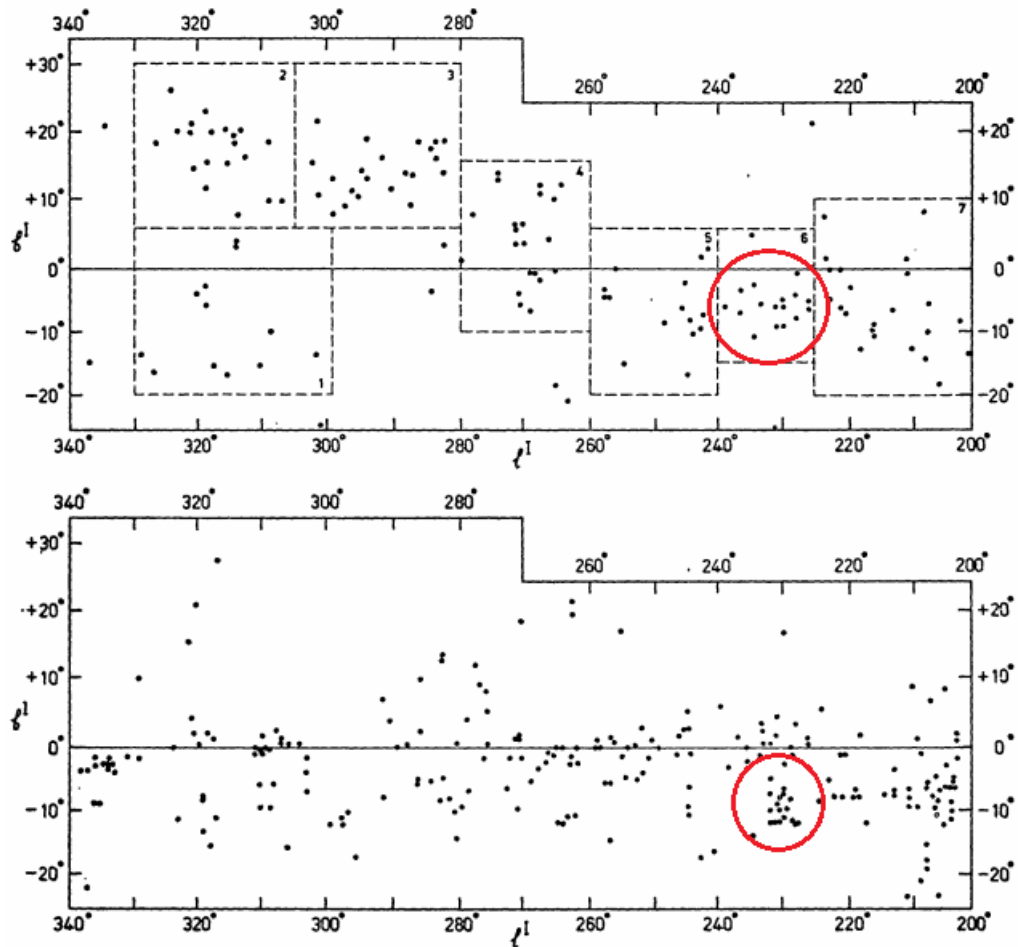
Figure 2.1: Figure 3 of Blaauw (1964) in old galactic coordinates. Top: O-B3 type stars brighter than $m = 4.5, 5.25, 5.5$ for types B0 and B1, B2, B3. Bottom: Stars fainter than these limits but still brighter than $m = 7.0$ The red circle is added to the original image to indicate the group of bright stars in the Vela region pointed out by de Zeeuw et al. (1999).

Wolf-Rayet star (28.5 $\pm$ 1.1 M$_\odot$, 9 $\pm$ 0.6 M$_\odot$; North et al. 2007), and nine other stars with similar distance moduli. They considered the possibility that all of these are members of an association. This coincided with the work of Upton (1973) who estimated distance moduli for 151 stars in the Bright Star Catalogue of type B5 or hotter in a $\sim 1200°$ area including the Vela and Puppis regions. He found evidence for the existence of three groups in the distance modulus range $7.6 < (m-M)_0 < 8.6$ ($\sim$ 400 - 500 pc), his association A containing γ Vel and PSR 0833-45 in its limits and extending to $(m-M)_0 > 7.0$ ($\sim$350 pc), adding strong support to the theory of Brandt et al. (1971).

Straka (1973) also picked up on this idea and compared the evidence for an association based on proper motions with evidence from the H-R diagram. He concluded that the proper motions of the 10 stars from Brandt et al. (1971) did not support the existence of an association since only 5 agree in position angle while the other 5 differ greatly and do not correlate with position. However, looking at the magnitudes and spectral types of all 498 O and B stars in this region (from the SAO catalogue), he found the distributions in magnitude of B2, B3, B5, B8 and B9 stars strongly suggested a group centered at $\sim$ 500 pc, a result that remained unchanged after several different attempts to remove foreground and background contaminants. This work also suggested an association age of order 10^7 years.

In a series of papers (Eggen 1980, Eggen 1982, Eggen 1983, Eggen 1986) Eggen considered the supposed cluster Collinder 173 (which includes the γ Vel system), Trumpler 10 and the open cluster NGC 2547 to be components of the "Vela sheet", the overdensity of B and A-type stars across this region at a distance of $350 - 450$ pc, and lists 29 members for Col 173 based on photometric evidence. He denotes a more distant association ($\sim$ 1.8 kpc) as Vela OB2, though since de Zeeuw et al. (1999) Vela OB2 has come to refer to the Vela sheet, and in particular, Col 173.

2.2 *Hipparcos*

The *Hipparcos* mission (Perryman et al. 1997) drastically improved the scope of investigation for OB associations with positions, proper motions and parallaxes for stars brighter than $V = 9$. In particular, the comprehensive study of de Zeeuw et al. (1999) used *Hipparcos* data to identify moving groups within 1 kpc, producing group membership probabilities for stars by combining the results of an updated convergent point method (De Bruijne 1999) with the "Spaghetti method " (Hoogerwerf & Aguilar 1999) (see section 1.4). They identified 93 probable members of Vela OB2 spread over ~ 100 deg^2, centered around $l = 263°$, $b = -7°$ and measured a mean distance of 410 ± 12 pc (Fig. 2.2). These members include γ^2 Vel (its binary partner γ^1 Vel was not in the catalogue), 3 other members from Brandt et al. (1971) but only 3 members from Eggen 1980; Eggen 1983; Eggen 1986, as 22 out of his 29 members were not included in the catalogue either. They find Vela OB2 and Col 173 to be the same entity, but consider Trumpler 10 a separate association in its own right.

From comparing these investigations it becomes evident how often groups and members of groups are reclassified when new data becomes available. This is something to bear in mind when we discuss which stars we consider part of Vela OB2 (chapter 6) and when discussing formation and evolution scenarios for the Vela complex (chapter 7).

2.3 Post-*Hipparcos* studies

The previously discussed investigations focussed on the massive members of Vela OB2 and did not touch on intermediate- and low- mass stars in the region, which
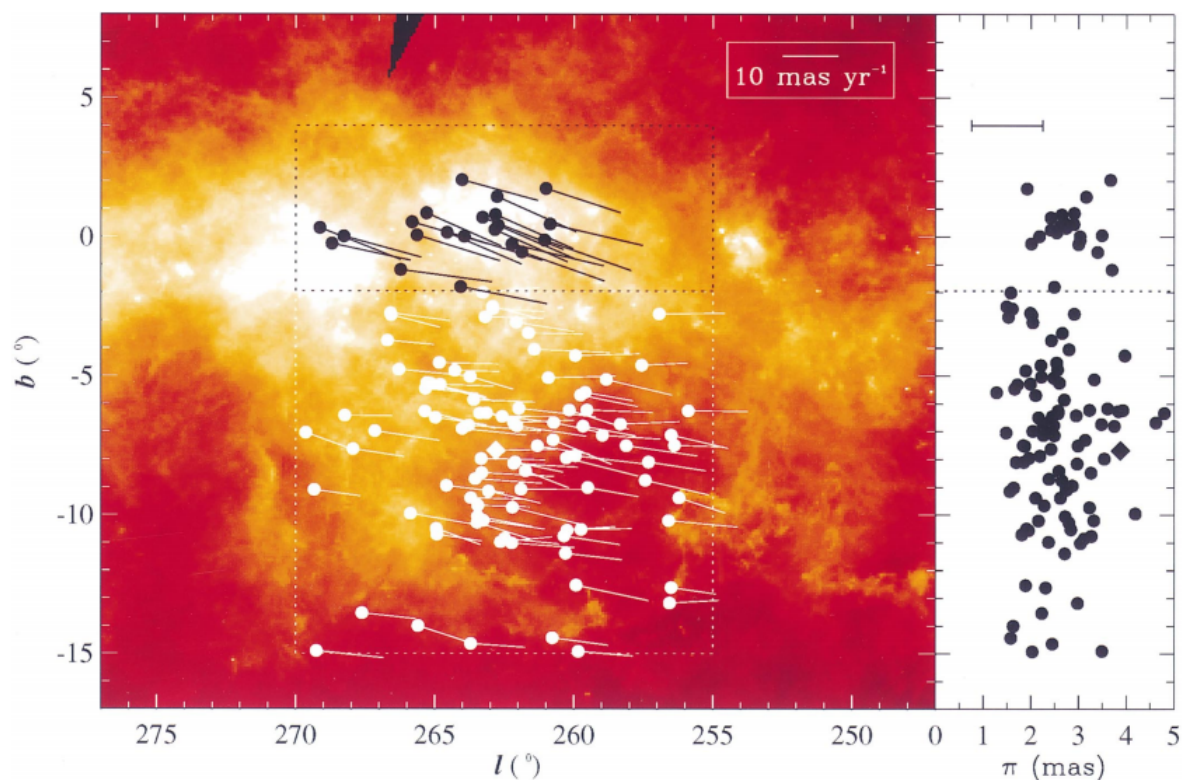
Figure 2.2: *Left* : Positions and proper motions for the *Hipparcos* members of Vela OB2 (white) and Trumpler 10 (black) from de Zeeuw et al. (1999) plotted over the IRAS 100μm skyflux. *Right* : Parallax and Galactic latitude for the same stars. The diamond denotes the Wolf-Rayet star γ^2 Velorum (WR 11).

according to a typical IMF (section 1.1.3) would mean the vast majority ($\sim 95\%$) of members were undiscovered up to this point. This is understandable, since until the advent of the X-ray detection of PMS stars in the 1980s such young stars were too difficult to identify against the background of field stars.

The first discovery of PMS stars in the Vela OB2 region came from Pozzo et al. (2000), who identified a population of PMS stars apparently clustered around γ^2 Vel using ROSAT[1] X-ray observations. They also obtained BVI photometry for the cluster field and compare the positions of the sources in a V-I vs V colour-magnitude diagram to low-mass isochrones for the assumed distance and reddening of Vela OB2 (410 pc, E(V-I)=0.06). They discuss at some length whether or not these are coeval and at the same distance as γ^2 Vel, and conclude that this is more plausible than the massive star having formed in isolation in the cluster's foreground, though this would mean γ^2 Vel would be located at a greater distance and therefore be of a greater mass than previous estimates would suggest.

The cluster was revisited by Jeffries et al. (2009) who combined BVI photometry in a 0.9 deg^2 area around γ Vel with optical spectroscopy and X-ray observations for subsamples to determine cluster membership probabilities. They confirm the youth of objects by detection of lithium absorption, Hα emission and X-ray activity. Their distance modulus for the cluster (7.76 ± 0.07) is in good agreement with that of Vela OB2 (7.72 ± 0.08), and so they conclude that the cluster does indeed belong to Vela OB2 and is aged ~ 10 Myr.

Jeffries et al. (2014) used spectroscopy from the Gaia ESO Survey (GES) (Gilmore et al. 2012) to measure radial velocities for 208 confirmed members of the γ Vel cluster. They find evidence for the existence of two kinematic populations among the PMS stars, with RV dispersions $\sigma_A = 0.34 \pm 0.16$ kms^{-1}, $\sigma_B = 1.60 \pm 0.37$ kms^{-1} and mean offset 2.15 ± 0.48 kms^{-1} (Fig 2.3). Population A is spatially concen-

---

[1]Röntgensatellit, as X-rays are Röntgenstrahlen in German

trated around γ^2 Vel while population B is more uniformly dispersed, and evidence of different levels of Li depletion suggests that population A is $1-2$ Myr older. They discuss several scenarios as possible explanations for the origin of these populations.

Core-halo - First is a scenario where population A is the bound core remaining from an originally larger cluster, and population B is a halo of stars no longer bound to the cluster, possibly as a result of residual gas expulsion. This is supported by the discrepancy between the mass of γ^2 Vel ($\sim 35M_\odot$) and the mass of population A ($\sim 100M_\odot$) , compared to the ratio expected between a cluster and its most massive star (Weidner, Kroupa & Bonnell 2010) which suggests a star of such a mass as γ^2 Vel would be more likely to form in a cluster of significantly higher initial mass $\sim 1000M_\odot$. If population B originally belonged to this cluster the mass ratio becomes more consistent. However, this does not explain the difference in mean velocities and inferred ages between the populations, so the authors believe this scenario is unlikely.

Captured cluster - Second is a scenario where the stars form in an unbound association, but over time γ^2 Vel collects smaller companion stars within its gravitational potential. Population A is comprised of these captured stars while B is the dispersing association. For a star as massive as γ^2 Vel this could happen within as few as $\sim$3 Myrs. This might explain population A's small velocity dispersion but still not the difference in Li depletion between the two populations.

Cluster + association - Lastly is the scenario where the γ Vel cluster formed in a particularly dense region of the Vela OB2 association, dense enough to be gravitationally bound. Some stars may have been expelled after residual gas expulsion and have mixed with the wider association but a bound cluster has remained. Within the extended star forming region of Vela OB2, age
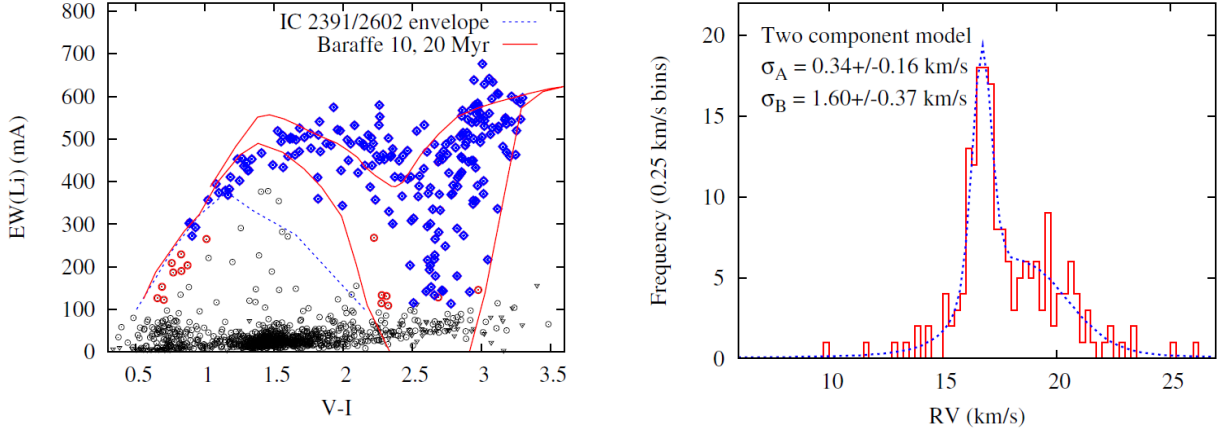
Figure 2.3: *Left* : V-I colour versus EW(Li). Blue points are candidate members and red points are possible members based on Li but are outside the colour-magnitude sequence. The red lines are 10 and 20 Myr isochrones (Baraffe et al. 1998) with reddening E(V-I) = 0.055. *Right* : Radial velocity histogram of γ Vel members showing the two-component Gaussian best fit. (Jeffries et al. 2014)

and velocity differences between stars formed in different regions are not surprising, so this scenario seems the likeliest.

Sacco et al. (2015) investigate GES observations of the cluster NGC 2547, which is located in close proximity (2 degrees south or ~ 10 pc) of γ Vel, and discover 15 stars that are likely to belong to population B from Jeffries et al. (2014). They consider two possible scenarios to explain the spatial extent of this population. Firstly an expanding cluster scenario, where after the formation of the central binary and residual gas expulsion, the γ Vel cluster began to disperse and low-mass stars ($< 0.5 M_\odot$) at the outer edge could have moved ~ 10 pc towards NGC 2547, considering the velocity dispersion of population B. This would also explain why the γ Vel cluster has a lower total mass than expected from the mass of γ^2 Vel (Jeffries et al. 2014), if many cluster members have dispersed to a larger volume. However,

they comment that this scenario does not explain why the two populations are offset in RVs, and that it is unlikely that other members of Vela OB2 would have spread out over its current volume from a smaller region given the age of γ Vel. More likely is that the association formed in a dispersed, low-density configuration that includes these stars belonging to population B, and that the clusters γ Vel and NGC 2547 were formed from locally dense regions of this association.

Focusing on the third scenario of Jeffries et al. (2014), Mapelli et al. (2015) perform N-body simulations of two subclusters colliding in order to constrain what conditions can recreate the features seen in the γ Vel cluster. They successfully reproduce the RV dispersions and offset between populations as well as the differences in concentration, centroid location and age. These results support the possibility that γ Vel is the product of two subclusters merging. Mapelli et al. (2015) also comment that population B is highly likely to be supervirial (total kinetic energy is greater than total gravitational potential) and is in the process of dispersing into the field.

Prisinzano et al. (2016) revisit the membership selection for γ Vel, combining photometry, measurements of radial velocity, EW(Li)s, Hα, the γ gravity index (Damiani et al. 2014), accretion activity and X-ray detection to produce a list of 242 confirmed cluster members, a sample more than 90% complete. They use evolutionary tracks and isochrones from Baraffe et al. (2015) assuming distance modulus 7.76 and $E(V - I) = 0.055$ for the cluster (Jeffries et al. 2009) to derive masses for 237 of these. They then derive the cluster IMF from this sample and find it consistent with a Kroupa (2002) canonical IMF, and using a Kolmogorov-Smirnov test, do not find significant evidence that the populations A and B have different mass distributions. However, considering the mass range used to determine the IMF, the total mass of the γ Vel cluster is estimated to be $\sim 100 M_\odot$, similar to the result of Jeffries et al. (2014), which is still inconsistent with the mass expected of a cluster containing γ^2 Vel ($\sim 35 M_\odot$). This suggests that the two populations originated from the same star

formation process in the same molecular cloud.

3 Gaia DR1 YSO identification

This chapter describes work performed using data from Gaia DR1, starting with an investigation into the dynamics of Vela OB2 based on the members from de Zeeuw et al. (1999). The results of this investigation showed that Vela OB2 is gravitationally unbound, but this result is based on a small sample of massive stars whose membership was determined using *Hipparcos* astrometry. In order to get a more accurate estimate of the volume, total mass and dynamical state of Vela OB2, we need a large sample of members with up to date astrometry. Thus we investigated how Gaia DR1 photometry could be used to identify low-mass members of Vela OB2, which would give us insight into the substructure of the association. Most of these results were published in Armstrong, Wright & Jeffries (2018).

3.1 High-mass members of Vela OB2

To investigate the dynamics of the Vela OB2 association we gathered the most up to date astrometry of its members.

With the release of Gaia DR1 came the TGAS catalogue, containing updated astrometry for objects observed by Hipparcos or Tycho-2, including 42 of the Vela OB2 members identified by de Zeeuw et al. (1999). This sample is incomplete (42/93 stars) due to the Gaia satellite's saturation limit of G = 5.7 at the time of DR1's publication. For the other 51 members we use Hipparcos astrometry in this investigation.

Our first aim was to assess the dynamical state of the OB members of Vela OB2. As a sparse OB association which is unstable to galactic tidal forces (Blaauw 1964) we expect that these stars are gravitationally unbound. We therefore expect
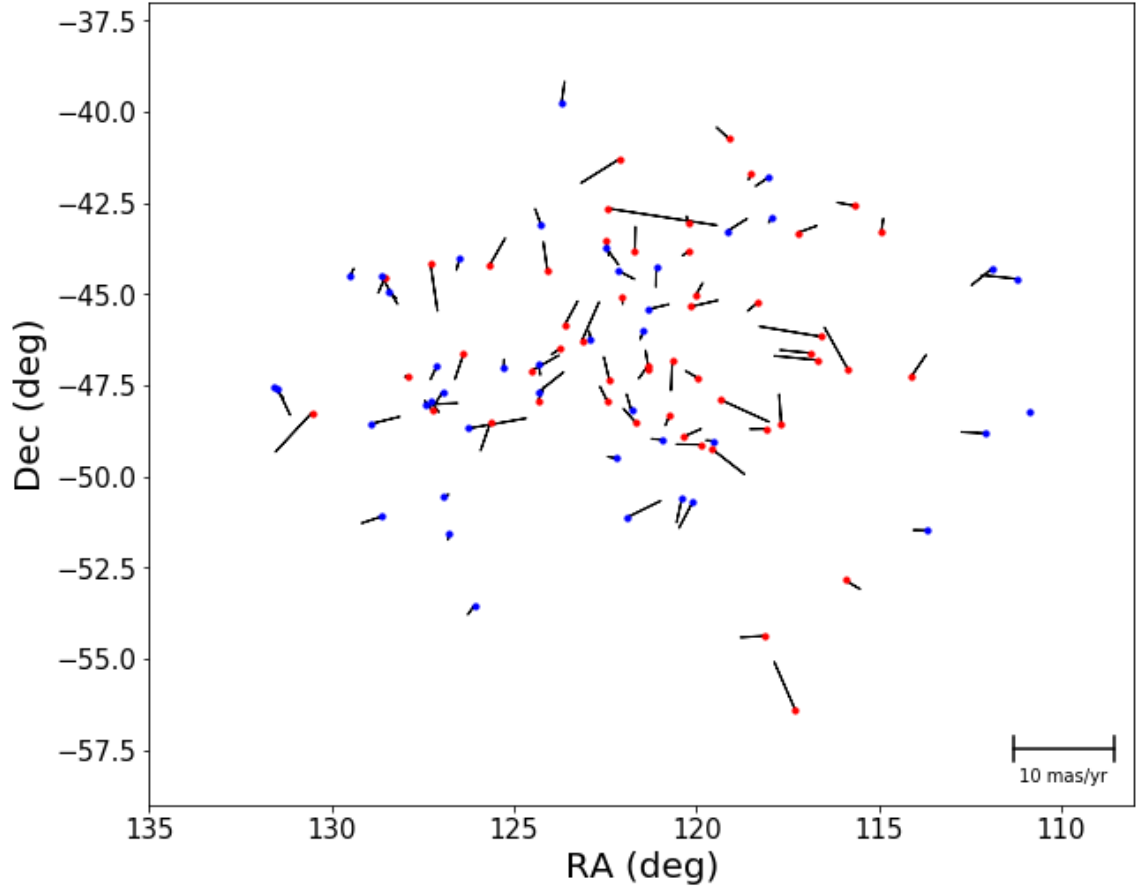
Figure 3.1: Figure showing the current positions in Right Ascension and Declination of the 93 Vela OB2 members, with their relative proper motions shown as vectors, scaled to show the distance travelled over 1 Myr. Only 42 members have proper motions available in the TGAS catalogue (blue), the others are plotted with *Hipparcos* (Perryman et al. 1997) proper motions (red).

that the virial theorem using the measured velocity dispersion will lead to a virial mass that is significantly higher than the estimated stellar mass of the association. In figure 3.1 we plot the positions and proper motions of these 93 stars. It should be noted that this is only representative of the high-mass component of the association,

there will likely be thousands of low-mass members that have yet to be identified (see section 3.2). However, due to the nature of the virial theorem, assuming no energy equipartition, objects within the association that are not included in this sample will still be indirectly represented in the total energy and thus the velocities we measure in the sample. This is one of the greatest strengths of the virial mass estimate, that estimates of virial mass can still be made with relative accuracy despite having an incomplete sample. The association's virial radius can also be determined accurately from this sample size assuming no mass segregation.

In figure 3.2, we plot histograms of the RA and Dec components of the members' proper motions to help visualise the distribution of velocities. For a single population we might expect the proper motions to follow a Gaussian distribution. A distribution of proper motions with multiple peaks may indicate the existence of multiple populations, such as in the γ Vel cluster (see section 2.3). Aside from the outlying points in the -12 to -10 mas/yr bin, the distributions in Fig. 3.2 show that the proper motions of the 93 O and B type members of Vela OB2 are reasonably well fit by a Gaussian distribution. Kinematic substructure (e.g, Wright et al. 2016) or expansive or contractive motion (e.g, Kounkel et al. 2018) are not apparent from a visual inspection of the OB members alone.

We wish to consider the motions of the stars in reference to the association, thus we must subtract the group mean velocity from each star's proper motion and then take the mean of the squares of these to find the average velocities in two dimensions ($\langle v_{RA}^2 \rangle = 6.14$ x 10^6 m^{2}s^{-2}, $\langle v_{Dec}^2 \rangle = 1.15$ x 10^7 m^{2}s^{-2}). We calculate the half-mass radius of the group by specifying the centre of the group as the position median, calculating each star's distance from that point, assuming a distance of 410 pc from the Sun to the association (de Zeeuw et al. 1999), and taking the distance that encloses half of the stars, essentially approximating the star's masses as equal ($r_h = 13.47$ pc). This provides an estimate for the mass of the association assuming
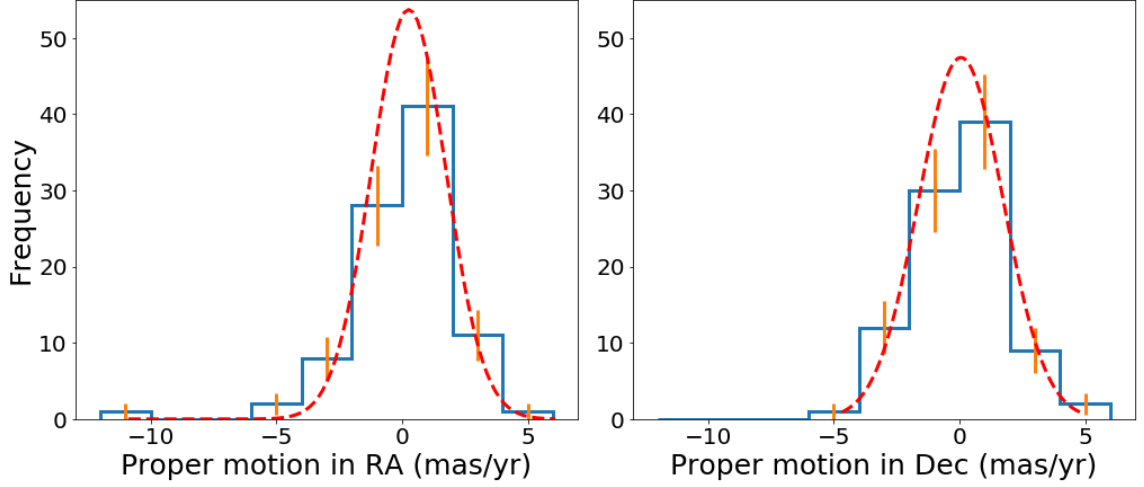
Figure 3.2: Distribution of proper motions of the 93 OB members of Vela OB2 with the association's average proper motions subtracted. The red dotted line is a Gaussian fit to the data using the interquartile range (to reduce the impact of outliers) with means at 0 and standard deviations $\sigma_{RA} = 1.486$ mas yr^{-1} and $\sigma_{Dec} = 1.683$ mas yr^{-1}.

it is in virial equilibrium.

$$M = \frac{5r_h(\langle v_{RA}^2 \rangle + \langle v_{Dec}^2 \rangle)}{3G} \tag{3.1}$$

$$= (9.19 \pm 0.10) \times 10^5 \ M_\odot \tag{3.2}$$

The mass of the association can also be estimated by assuming a fit to an IMF and extrapolating the sample of OB stars to cover the full mass spectrum. We chose to use the Maschberger (2013) IMF model to randomly generate a population to match the population of high-mass stars of Vela OB2 from de Zeeuw et al. (1999). The quantile function of the Maschberger IMF is of the form

$$m(u) = \mu([u(G(m_u) - G(m_l)) + G(m_l)]^{\frac{1}{1-\beta}} - 1)^{\frac{1}{1-\alpha}} \tag{3.3}$$

where

$$G(m) = (1 + (\frac{m}{\mu})^{1-\alpha})^{1-\beta} \tag{3.4}$$

is the 'auxiliary equation', $\alpha = 2.3$ is the high-mass exponent, $\beta = 1.4$ is the low-mass exponent, $\mu = 0.2 M_\odot$ is the scale parameter, $m_l = 0.01 M_\odot$ is the lower mass limit, $m_u = 150 M_\odot$ is the upper mass limit and u is a randomly generated number between 0 and 1.

At this point we judged 11 of the 93 bright stars as unlikely to belong to the association, seven due to significantly higher B-V values (likely late-type contaminants, Fig. 3.3), and four with Gaia DR2 parallaxes significantly higher or lower than the rest of the sample.

Populations were created by randomly generating values for u and substituting these into the quantile function to produce stellar masses. For each population this is repeated until 82 stars with masses $> 3 M_\odot$ (roughly the minimum mass of a B-type star) are produced, after which the total number of stars in the population and the total mass of the population is recorded (see Fig. 3.4).

We generate $10,000$ populations and look at the averages of the total number of stars and the total population mass. The mean total cluster mass of 10000 randomly generated populations is 1888 ± 156 M$\odot$, less than our result from the virial theorem by at least an order of magnitude.

The discrepancy in this estimate informs us of its dynamical state. Recall the assumptions required for application of the virial theorem, in particular, the assumption that the cluster is gravitationally bound. As we mentioned earlier in section 1.3, it has been theorised that associations are typically unbound. The masses of unbound, expanding systems are likely to be vastly overestimated by the virial theorem. Our apparent overestimation of the mass of Vela OB2 is a good indication that it is also gravitationally unbound, and may have expanded outward to its present size from a smaller region in which it was formed. However, if the association is indeed formed of subclusters of low-mass stars congregated around the O and B type stars, each subcluster may still be in virial equilibrium, though the whole association is not.
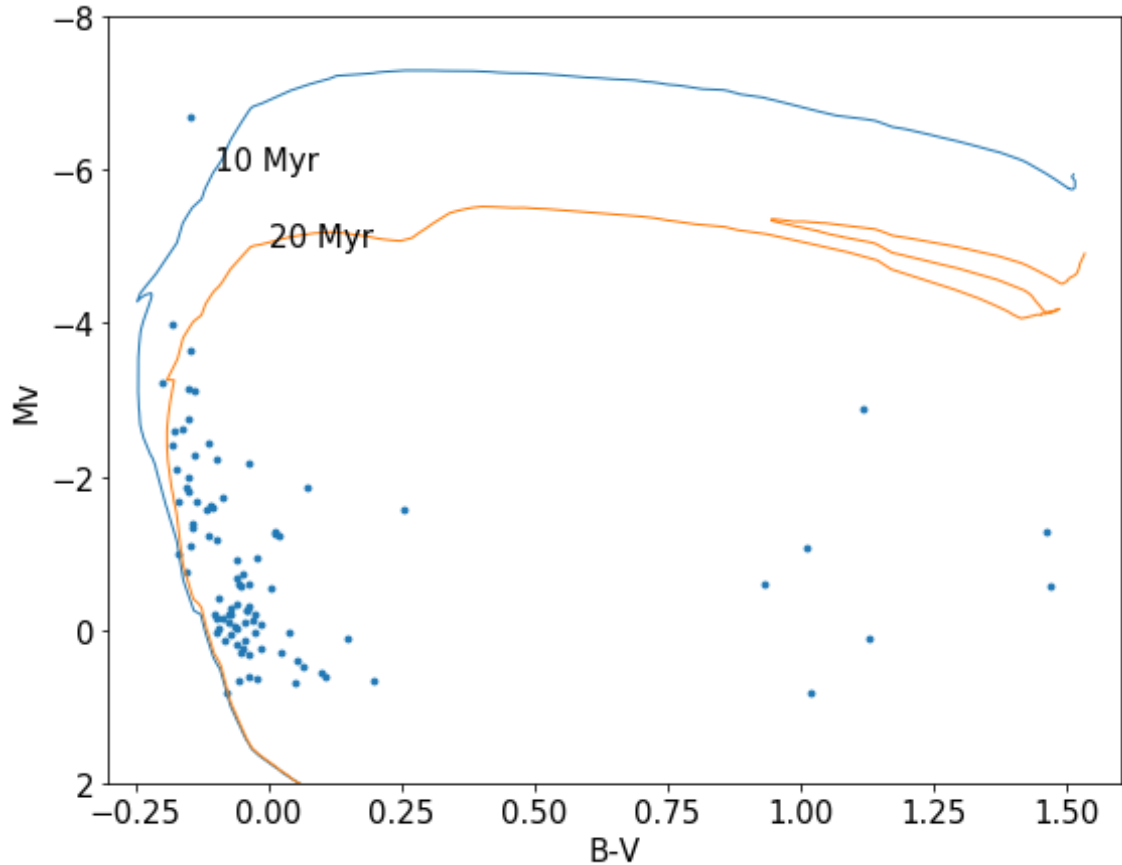
Figure 3.3: From Armstrong, Wright & Jeffries (2018), B-V vs Mv colour-magnitude diagram of the 93 high-mass association members from de Zeeuw et al. (1999). Mv values were calculated using B-V and V from the Extended Hipparcos Compilation of Anderson & Francis (2012), parallaxes for 86 stars from Gaia DR2 (Luri et al. 2018) and reddening of $A_V = 0.131$ mag from Jeffries et al. (2014). For the 7 high-mass stars without Gaia DR2 parallaxes, the median parallax value of the sample was used. Also plotted are 10 and 20 Myr isochrones from Ekström et al. (2012) for stars with $Z = 0.014$, using bolometric corrections (BCs) for B type stars from Pecaut & Mamajek (2013). The 7 stars with large B-V colour were considered to be non-members of the association and removed from the sample. The difference in colour between the isochrones and the majority of stars is possibly due to localised extinction or inaccuracies in the model atmospheres.
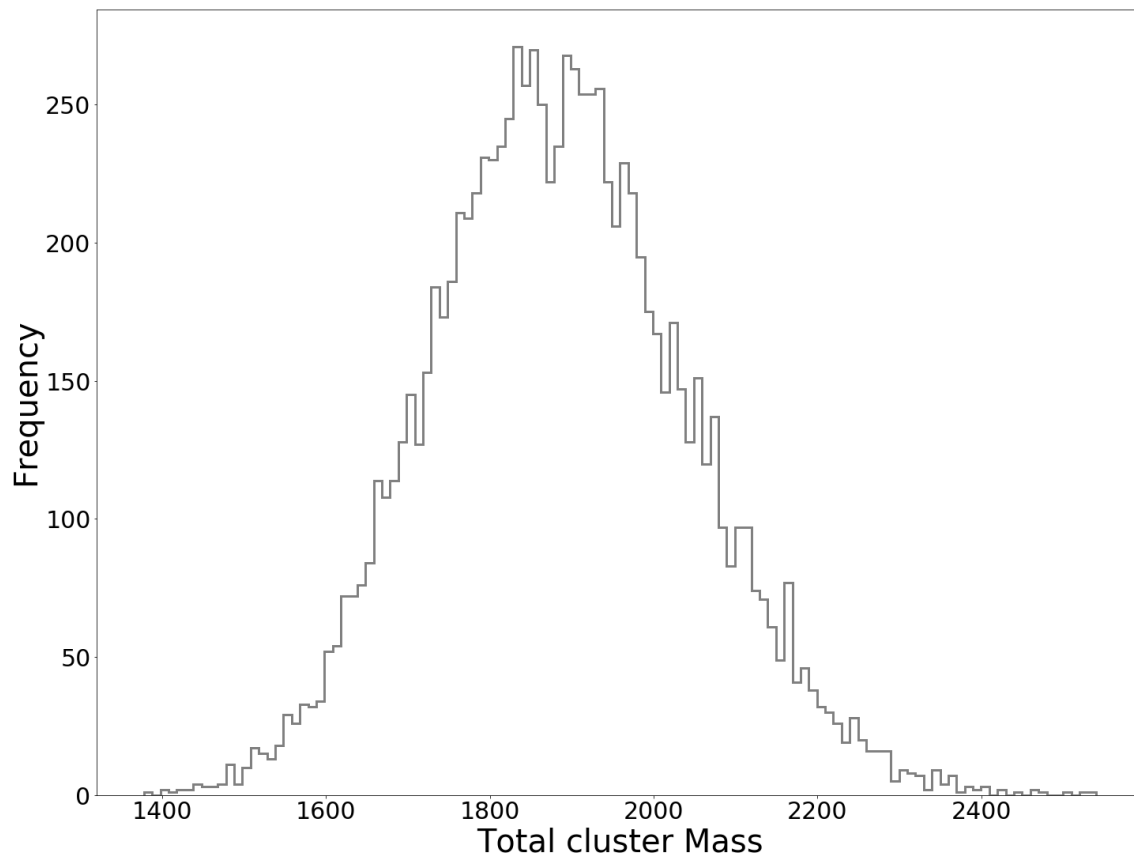
Figure 3.4: A histogram of total cluster masses generated using the Maschberger (2013) IMF for 10000 populations with 82 stars of $> 3M_\odot$.

3.2 Estimating the size of the low-mass population of Vela OB2

The sample of association members identified by de Zeeuw et al. (1999) are the brightest and most massive stars only, the vast majority of stars in the association will be much less massive and fainter. If we are able to identify this low-mass population we will be able to assess the state of Vela OB2 in far greater detail than before.

Firstly, we want an idea of the size of this low-mass population. In order to estimate the total stellar mass and expected low-mass population of Vela OB2, we created model populations using the Maschberger (2013) IMF (see section 3.1) to match the high mass population from de Zeeuw et al. (1999), but refine the method by taking into consideration the completeness limit (the turn-over point in the observed luminosity function) of the OB population sample. Based on the remaining association members relative to the isochrones (Fig. 3.3) we estimate the sample completeness limit to be at $\sim 2.5 M_\odot$ (Fig. 3.5), with 72 of the 82 likely Vela OB2 members being at least this massive.

Ten thousand stellar populations were randomly generated using the Maschberger (2013) IMF, sampling until 72 stars with $M > 2.5 M_\odot$ were produced, and then noting the total number of stars and total mass of the population for each iteration. The median number of stars with $M > 0.1 M_\odot$ in a randomly generated population was 1965 ± 228 and the median total mass was $1285 \pm 110 M_\odot$ (Fig. 3.6).

Jeffries et al. (2014) and Prisinzano et al. (2016) found only 278 likely cluster members in the 0.9 degree^2 area around γ^2 Vel with a $\sim 90\%$ complete sample. Thus, assuming that the whole population of Vela OB2 follows a standard IMF, we estimated that there are ~ 1600 association members yet to be identified in the wider area of the association, with ~ 1085 of these within in the mass range $1.5 > M/M_\odot > 0.2$ sampled by Jeffries et al. (2014).

PMS evolutionary tracks from Baraffe et al. (2015) were plotted in a G-K vs
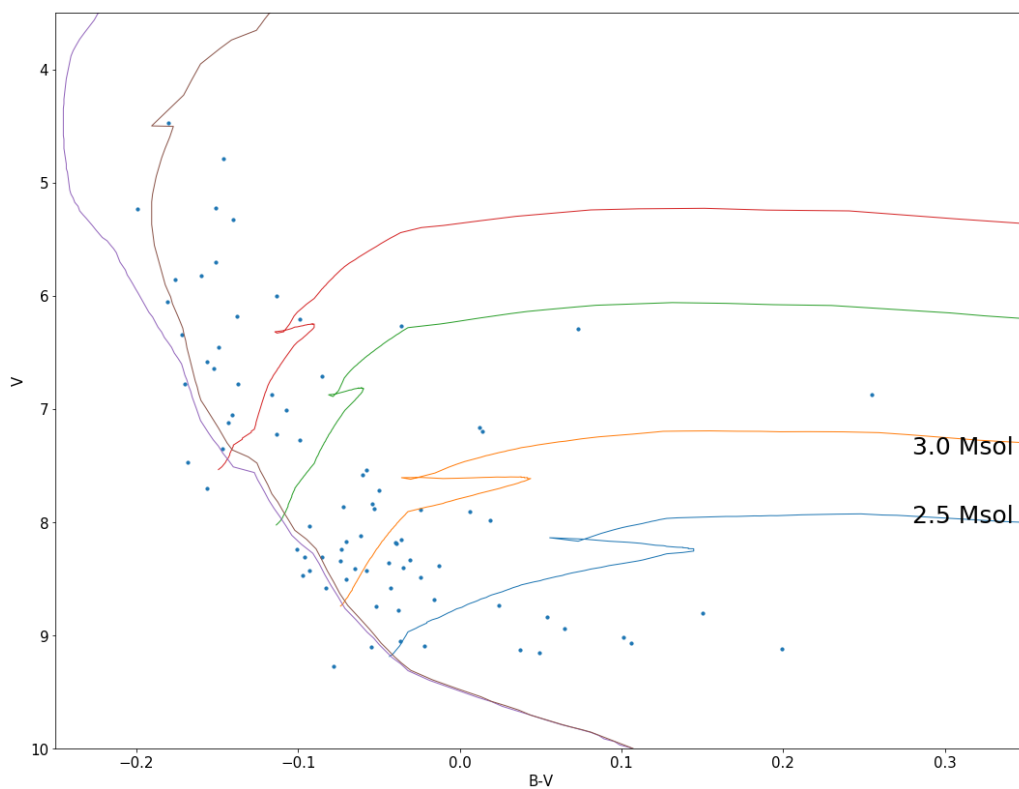
Figure 3.5: B-V vs V colour-magnitude diagram of the 82 high-mass association members from de Zeeuw et al. (1999) using B-V and V from the Extended Hipparcos Compilation of Anderson & Francis (2012). Also plotted are evolutionary tracks from Ekström et al. (2012) for stars with $Z = 0.014$, using bolometric corrections (BCs) for B type stars from Pecaut & Mamajek (2013). From this diagram, we estimate the sample completeness limit to be at $\sim 2.5 M_\odot$, as there are fewer sources below this evolutionary track than between $3 - 2.5 M_\odot$.
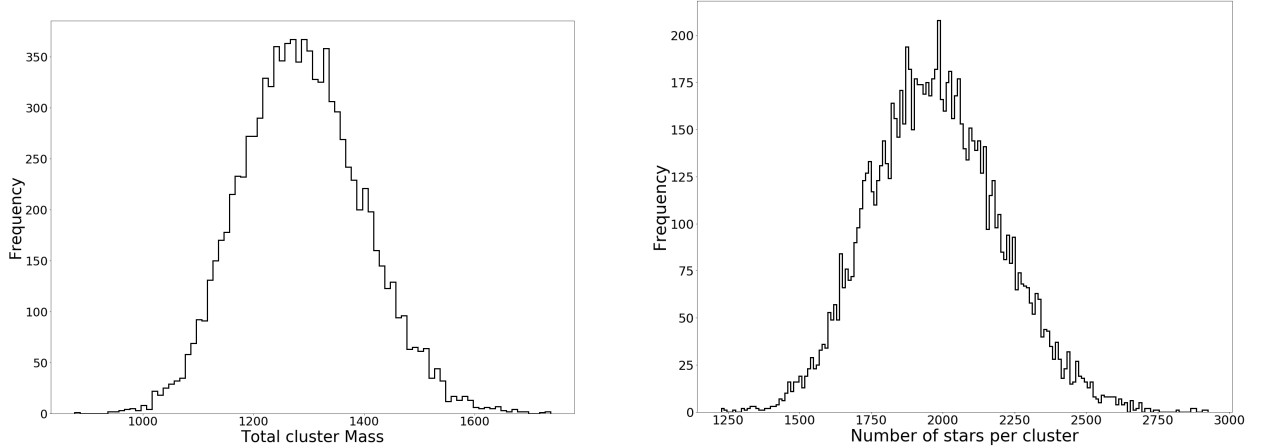
Figure 3.6: *Left* : Histogram of total cluster masses generated using the Maschberger (2013) IMF for 10000 populations with 72 stars of $> 2.5 M_\odot$. *Right* : Histogram of number of stars per cluster generated using the Maschberger (2013) IMF for 10000 populations with 72 stars of $> 2.5 M_\odot$.

G colour-magnitude diagram converted from $\log L$ and $\log T_{eff}$ using BC values for young stars from Table 6 of Pecaut & Mamajek (2013), a V-I to G-V conversion from Jordi et al. (2010), alongside our G-K vs G selection box (Fig. 3.7 *left*). The selection box was chosen to select stars in the mass ranges $0.45 M_\odot > M > 0.17 M_\odot$ for a 10 Myr isochrone and $0.39 M_\odot > M > 0.16 M_\odot$ for a 20 Myr isochrone. The Baraffe et al. (2015) PMS isochrones were used here as they cover the low mass range $(1.4 M_\odot > M > 0.07 M_\odot)$ to which our target PMS stars belong, whereas the Ekström et al. (2012) isochrones are for high-mass main-sequence stars $(120 M_\odot > M > 0.8 M_\odot)$. The mean number of stars in these mass ranges produced in our randomly generated populations was 815 and 788 stars respectively.
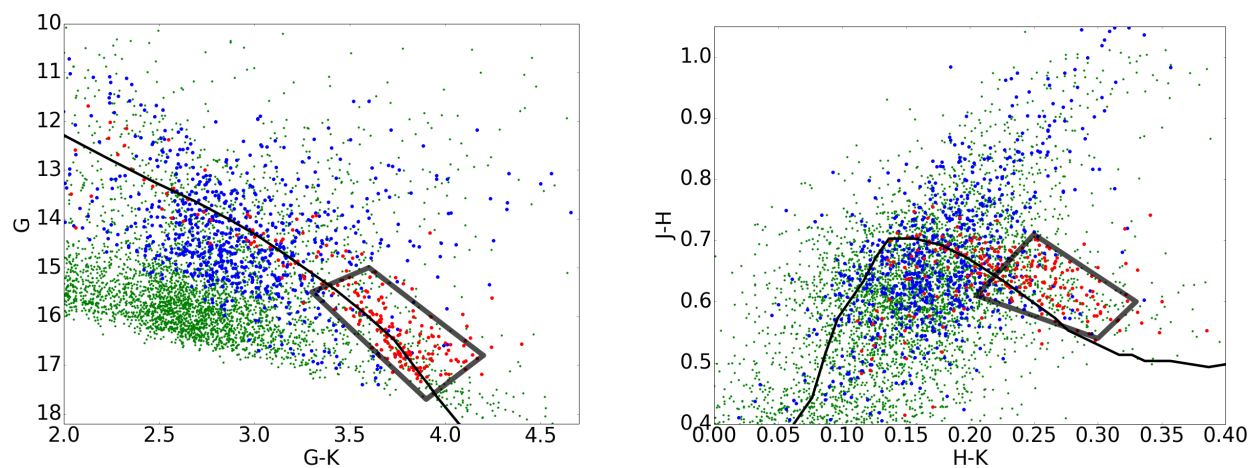
Figure 3.7: *Left* : G-K vs G colour magnitude diagram of objects with both Gaia and 2MASS photometry (green) within a 0.9 degree^2 area around γ Velorum, spectroscopically identified young stars (red) and field stars (blue) from Jeffries et al. (2014). The box encases the area containing the highest ratio of red points to blue and green points, thus expected to be the area where unconfirmed (green) stars have the highest likelihood of being cluster members. Also shown is a 10 Myr PMS isochrone from Baraffe et al. (2015) at a distance modulus of 7.76 mag and reddened by $A_V = 0.131$ mag (Jeffries et al. 2014). *Right* : H-K vs J-H colour-colour diagram for the same objects. A 10 Myr PMS isochrone from Baraffe et al. (2015) and a second selection box are shown. These plots were the final versions published in Armstrong, Wright & Jeffries (2018).

3.3 Searching for low-mass association members

Due to the shape of the IMF, the vast majority of stars in an OB association will be of a lower-mass ($\sim 0.1 - 1 M_\odot$), and we have estimated that there are ~ 1600 association members to be identified in Vela OB2. Analysis of the distribution and kinematics of these low-mass members will allow us to learn much more about the formation and dynamical evolution of the association than the OB member sample alone.

In order to begin analysing the distribution of an association's low-mass members, we must first develop a method to reliably identify them, separating association members from field stars in the foreground and background. We would like to be able to judge the likelihood of whether or not a star belongs to an association without relying on its astrometry, in order to avoid introducing biases into the later analysis. In the case of Vela OB2, which is of an age $\sim$ 10 - 20 Myr (de Zeeuw et al. 1999), its low-mass members are still too young to have evolved onto the main sequence, so they may be identified using Gaia and 2MASS photometry. Spectroscopic identifiers, while being in many cases more precise than photometry, are not yet available on such a scale. Jeffries et al. (2009) and Jeffries et al. (2014) used the photometric identification of PMS stars (in combination with other identifiers) in the 0.9 degree^2 around γ Vel, and since this cluster of stars very likely belongs to Vela OB2, we can use their position on a colour-magnitude diagram to create a photometric filter for young low-mass stars across the wider association.

3.3.1 Photometric selection

In order to define the photometric selection criteria we combined G band photometry from Gaia and J, H and K photometry from the 2MASS catalogue for all objects

within the area around the known OB members of Vela OB2 ($254° < l < 271°$, $-16° < b < 1°$). Data taken from the 2MASS catalogue were filtered based on given quality flags (Skrutskie et al. 2006), which are based on measurement uncertainties and scan signal-to-noise ratios (e.g, 'A' = valid measurement with SNR > 10 and uncertainty < 0.10857). Initially we selected sources with A to C quality photometry, but later restricted this to A only for all three bands, as well as requiring uncertainties in J, H and K-band magnitudes < 0.05 mag to reduce contamination from outliers. We also required the contamination of confusion flag 'Cflg' equal to '0' for all three bands. These filters reduced our sample of sources from 589,000 to 99,935, predominantly removing background artifacts and confused or faint sources.

These objects were filtered through selection boxes in G-K vs G and H-K vs J-H diagrams (Fig. 3.7). Fig. 3.7 *left* shows all objects in our sample within the 0.9 degree^2 around γ Vel in the G-K vs G diagram (green), with an illustrative 10 Myr isochrone from Baraffe et al. (2015), at a distance modulus of 7.76 mag and reddened by $A_V = 0.131$ mag (Jeffries et al. 2014). Uncertainties were not taken into account to judge if sources are inside or outside selection boxes. This will lead to some uncertainty in the exact membership, but this effect is likely to be small. Objects spectroscopically characterised as young stars by Jeffries et al. (2014) and Prisinzano et al. (2016) are identified, as are objects spectroscopically confirmed to be contaminating field stars. The previously identified objects form a clear PMS in Fig 3.7 *left*, following the 10 Myr isochrone. The selection box is designed to select this sequence but exclude the extensive contamination at brighter magnitudes. 138 members (red in Fig. 3.7) and 22 non-members (blue in Fig. 3.7) from Jeffries et al. (2014) and Prisinzano et al. (2016) appear within the G-K vs G selection box, as well as 25 sources not included in the Jeffries et al. (2014) sample (green).

3.3.2 Estimating contamination

Initially we used the G-K vs G filter alone, but realised there would still be some amount of contamination from other objects located in the selection box, such as distant giants faint and red enough to appear close to the PMS stars. We used the Jeffries et al. (2014) γ Vel cluster members to get an idea of the number of contaminants we expected to find in the area of sky around Vela OB2. The whole association spans an area of 100 square degrees on the sky, much larger than the area considered by Jeffries et al. (2014), so we took multiple 1 degree squares of the sky around γ Vel and, for each, considered how many objects appear in the box on the colour-magnitude diagram. Looking at separate 1 square degree areas of sky is not only convenient, since we can use the number of PMS stars identified in Jeffries et al. (2009) to predict the numbers of background stars in each, but would also give us a rough idea of the spatial variation of the numbers of low-mass members.

For the 1 square degree area with γ Vel at the center, which is where we have GES data, members constituted $130/(130 + 69) \sim 65\%$ of the objects in our initial selection area of the G-K vs G diagram. We therefore predicted that among the 61 unconfirmed objects in the same area we should have approximately 40 members and 21 non-members, so an approximate total of 170 members and 90 non-members. We then used this to predict how many of the unconfirmed objects in our G-K vs G selection in other 1 square degree areas are likely to be association members. If our expectation that these low-mass members are clustered is correct, they will not be evenly distributed across the sky, so there is no reason why we should expect to find the same number of probable members in each 1 square degree. Instead, we considered the numbers of background and foreground objects, the 90 non-members with adjustments for known background features such as more distant clusters not related to Vela OB2, in each 1 square degree. We counted the number of objects that lie in our G-K vs G area selection, subtract our expected number of background/foreground

objects, and the remainder shall be our number of probable cluster members in that box of sky.

A basic expectation for our numbers of background/foreground objects would be to predict uniformity, and expect 90 non-members in each square degree. But due to the large area of the association and its proximity to the Galactic disk it is likely that there will be significant variation in levels of contamination over the whole area. We attempted to make a more accurate estimate by using measurements of background object density and background dust levels in each area of sky. We used the Besançon galaxy model (Robin et al. 2003) to produce photometric data in V, I, J, H and K bands for objects at a greater distance than the Vela OB2 association. The Gaia G-band data was then calculated using a polynomial transformation from the V and I magnitudes (Jordi et al. 2010). For each square degree of sky, the Besançon data was then plotted in a G-K vs G diagram (Fig. 3.8 *right*) with the exact same selection box as the observational data, and the number of model objects within the area was recorded. The number of contaminants in the 1 square degree area around γ Vel predicted by the model was significantly larger than that predicted by the number of known non-cluster members from GES. This was likely due to the number of objects removed from our sample by our photometric quality filters earlier, so when using the Besançon model numbers we applied a scaling factor based on this difference in predicted contaminants. This process was then repeated for 1 degree boxes in the surrounding area (Fig 3.8 *left*).

3.3.3   The infrared selection

We then designed a second selection box in the H-K vs J-H diagram, in order to filter out any remaining contaminating giants. The H-K vs J-H diagram in Fig. 3.7 *right* shows the same objects as in the G-K vs G diagram. Distant giants will be
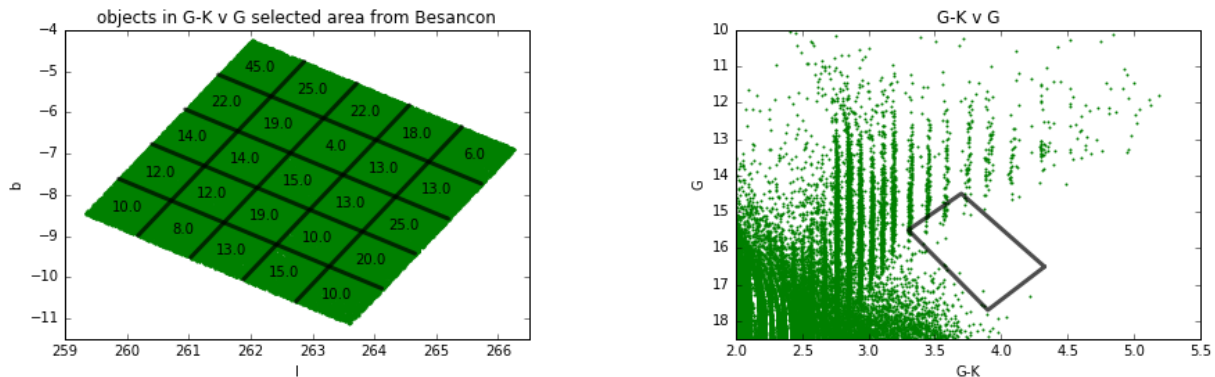
Figure 3.8: *Left* : The 5 square degree area of sky around γ Vel is divided into 1 square degree sections, with the number of Besançon objects that appear in our box of the G-K vs G diagram for each section. *Right* : An example of how the Besançon data looks in a G-K vs G diagram and where our box lies (this is the 1 square degree section at the top of the left hand plot, with 45 objects found in the box). The quantised appearance of the data is a result of a step-wise procedure in the model.

reddened away from PMS stars in this diagram and so we employ the selection box indicated to select just the PMS stars. Combining these two selection methods allows the selection of young, low-mass stars with a much lower rate of contamination. 81 spectroscopically identified members and 4 non-members appear within both selection boxes, so including this second filter should reduce our contamination rate from $\sim 35\%$ to $\sim 5\%$.

This second selection was also applied to the Besançon model and greatly reduced the number of model contaminants, essentially eliminating variation in galactic longitude. We adapted our method for estimating contaminants with the Besançon model by calculating the average number of contaminants to fulfil both the colour-magnitude and colour-colour selections in a 1 square degree area of sky for a given galactic latitude (Fig. 3.9). The average number of contaminants varies very little over the range of galactic latitude of the association. Thus we decided to use the
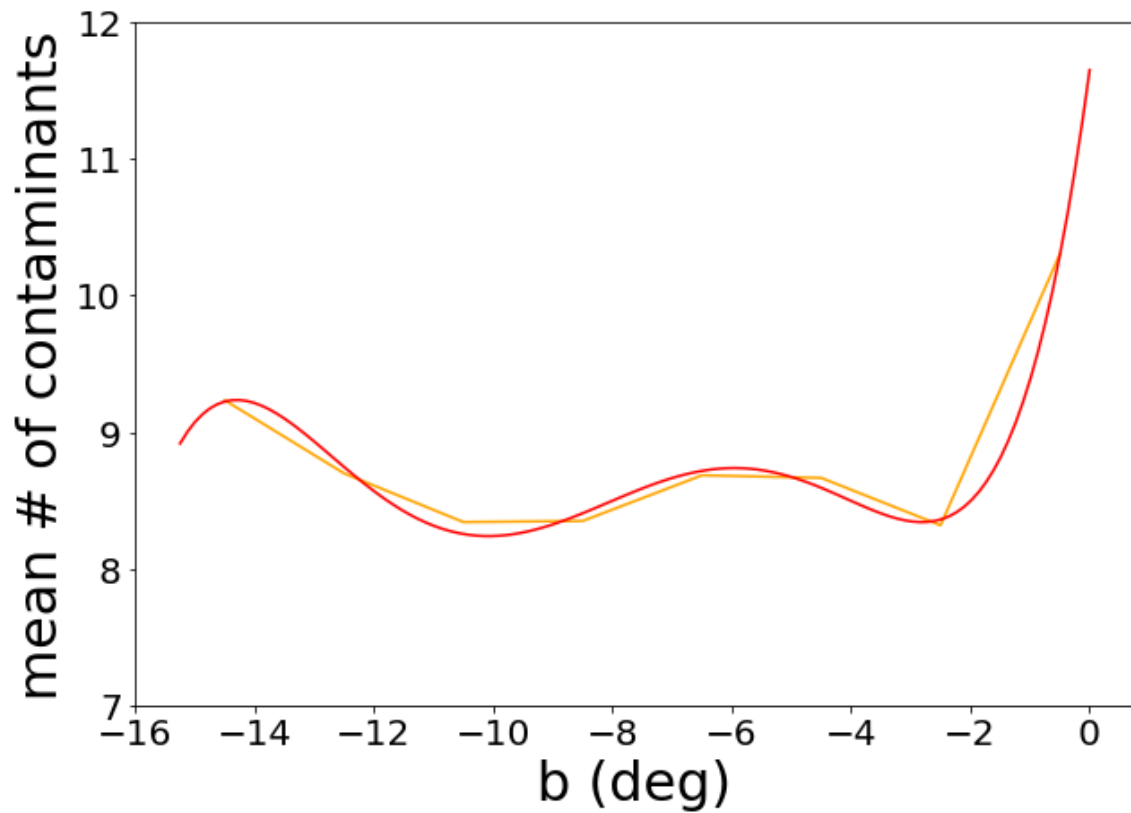
Figure 3.9: Average number of Besançon model field stars to fulfil both G-K vs G and H-K vs J-H filters in a 1 square degree area for a given galactic latitude over the area of Vela OB2. Plotted are the average values (yellow) and a polynomial fit (red).

average value across the area of the map, which resulted in a mean contaminant level of $\sim 8.8 \pm 0.6$ deg^{-2}, reasonably consistent with the number of spectroscopic non-members found within the 0.9 degree^2 area around γ^2 Vel by Jeffries et al. (2014) and Prisinzano et al. (2016). According to the Besançon model $\sim 98\%$ of the remaining contaminants are at distances < 200 pc and are main sequence M-dwarfs in the foreground of Vela OB2.

3.4 Creating a map of likely low-mass association members

We were now able to select probable PMS stars at the distance of the association with reasonable accuracy and have a method for estimating contamination levels, allowing us to investigate the structure of the low-mass population of the association by plotting the numbers of likely members per unit area. This density map went through several iterations, first using only the G-K vs G filter and selecting a small area around γ Vel in a celestial coordinate grid (Fig 3.10), to incorporating both photometric selection criteria, subtracting the expected contamination rate from the Besançon model and covering the whole area of the association in a galactic coordinate grid (Fig 3.11).

The density maps were created by dividing the area of sky to be plotted into a square grid and counting the number of Gaia DR1 + 2MASS sources to fulfil the photometric selection criteria within a given radius from the center of each square. The contamination rate was subtracted and the relevant area on the grid coloured by the number of expected PMS stars in the region. Coloured squares on the grid overlapped to improve the smoothness of the map in later versions, as well as using a finer grid to improve detail. The final version of the map published in Armstrong,
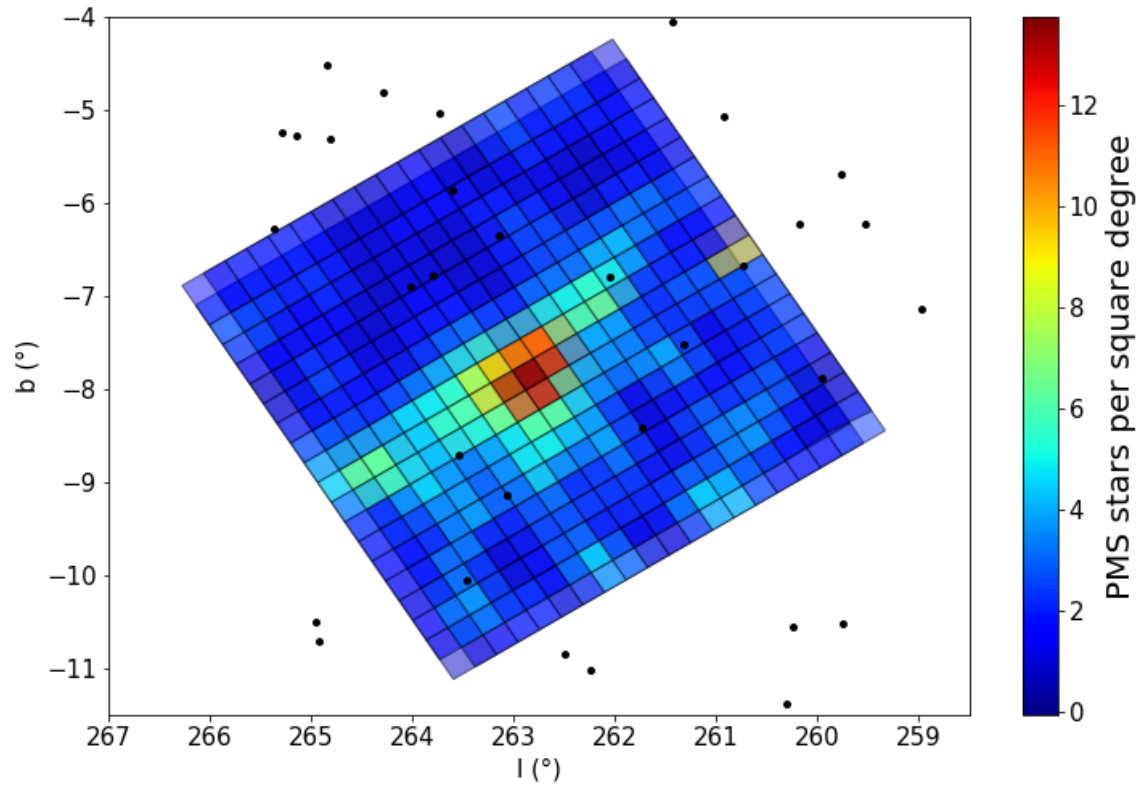
Figure 3.10: The 25 square degree area of sky around γ Vel divided into a 20×20 grid of 0.25 deg^2 squares, with colour indicating the number of G-K vs G selected objects per square. Black dots indicate positions of OB members (de Zeeuw et al. 1999). The area of greatest PMS candidate density coincides with the approximate location of the γ Vel cluster.
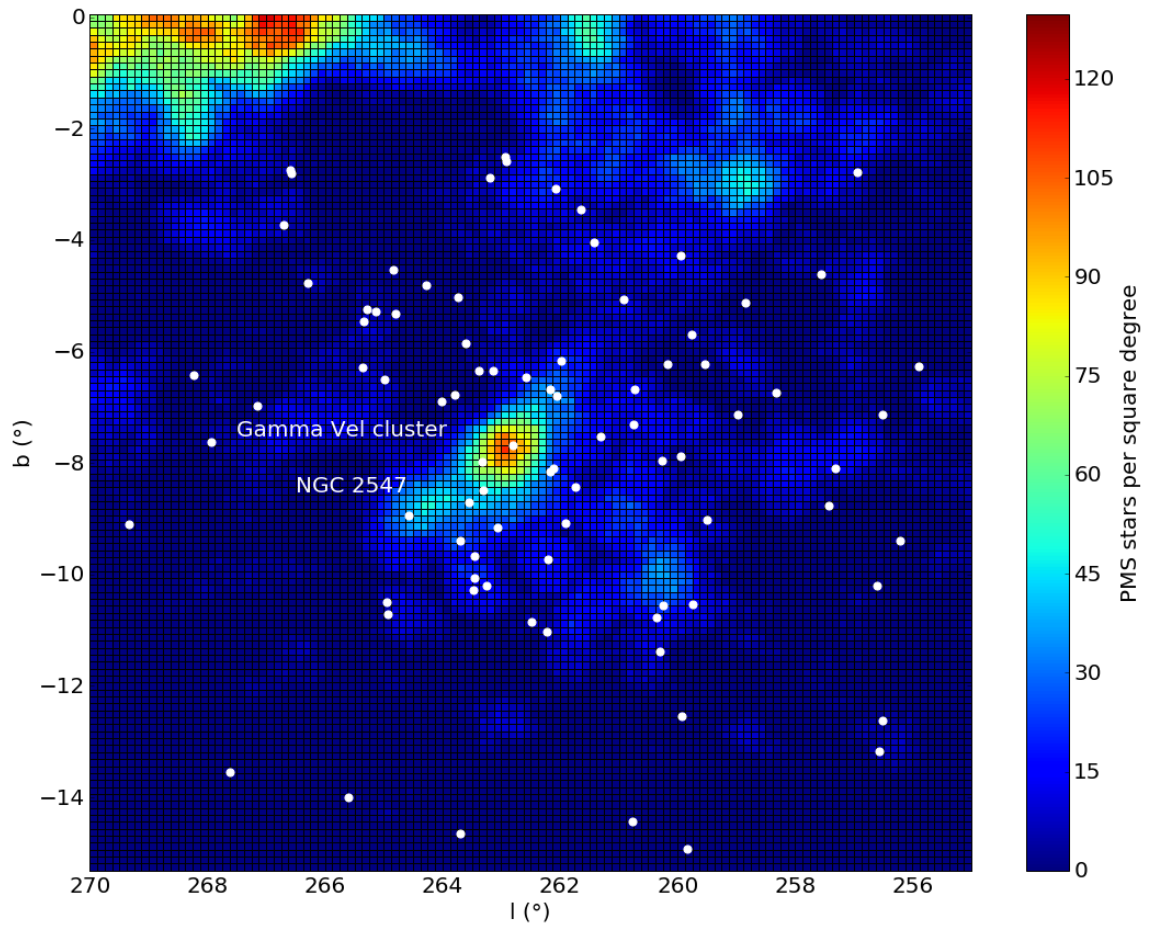
Figure 3.11: A 225 square degree area map of the wider association divided into 0.25 deg^2 squares, with colour indicating the number of G-K vs G and H-K vs J-H selected objects per degree. OB members are shown as white dots and the over-densities indicating the γ Vel cluster and NGC 2547 are labelled.

Wright & Jeffries (2018) is seen in Fig. 3.12. This version differs from Fig. 3.11 in that known members of NGC 2547 from Sacco et al. (2015) have been removed, OB members from de Zeeuw et al. (1999) who have inconsistent parallaxes and B-V colour are removed (Section 3.1) and Galactic latitude is capped at b=-2°. In this final low-mass PMS star density map, the γ Vel cluster is detected and appears as the region of greatest density of young low-mass stars in the association.

In order to remove contamination from the older and more distant NGC 2547 cluster (age $\sim$ 35 Myr, Jeffries & Oliveira 2005, distance modulus 8.10 mag, Naylor et al. 2002) we match known cluster members from Jeffries et al. (2004) to Gaia DR1 and 2MASS and perform the same photometric selection tests. 30 NGC 2547 members pass both tests and thus contribute to contamination in our sample. Accounting for the incompleteness of this sample using the incompleteness estimates in Jeffries et al. (2004), we subtract these sources from the relevant areas of the density map in Fig. 3.10. Jeffries et al. (2004) estimate that $\sim$ 100 members of NGC 2547 exist beyond the area of their observations. Based on the fraction of Jeffries et al. (2004) sources that passed our selection tests, we estimate that only 6% of these will appear in the density map. Their contribution is therefore not significant.

After specifically removing the NGC 2547 cluster, there remains a lower-density extended population around γ Vel and towards the Galactic plane. Two other regions of high density appear at (l = 260.25°, b = -10.25°) and (l = 259.0°, b = -3.25°). In Caballero & Dinis (2008) a young cluster was identified in the first of these regions by use of the DBSCAN clustering algorithm on blue *Hipparcos* stars and was named the 'P Puppis' cluster after the brightest member star. This cluster also coincides with cluster 1 of Beccari et al. (2018). Otherwise the low-mass population appears to be spread sparsely over the Vela OB2 association, albeit with considerable substructure. Notably, the open cluster IC 2395 located at (l = 266.63°, b = -3.58°) at a distance of 800 pc and of comparable age to Vela OB2 (9 ± 3 Myr, Balog et al. 2016) is hardly visible in Figure 3.12, indicating that our selection method is effective in excluding
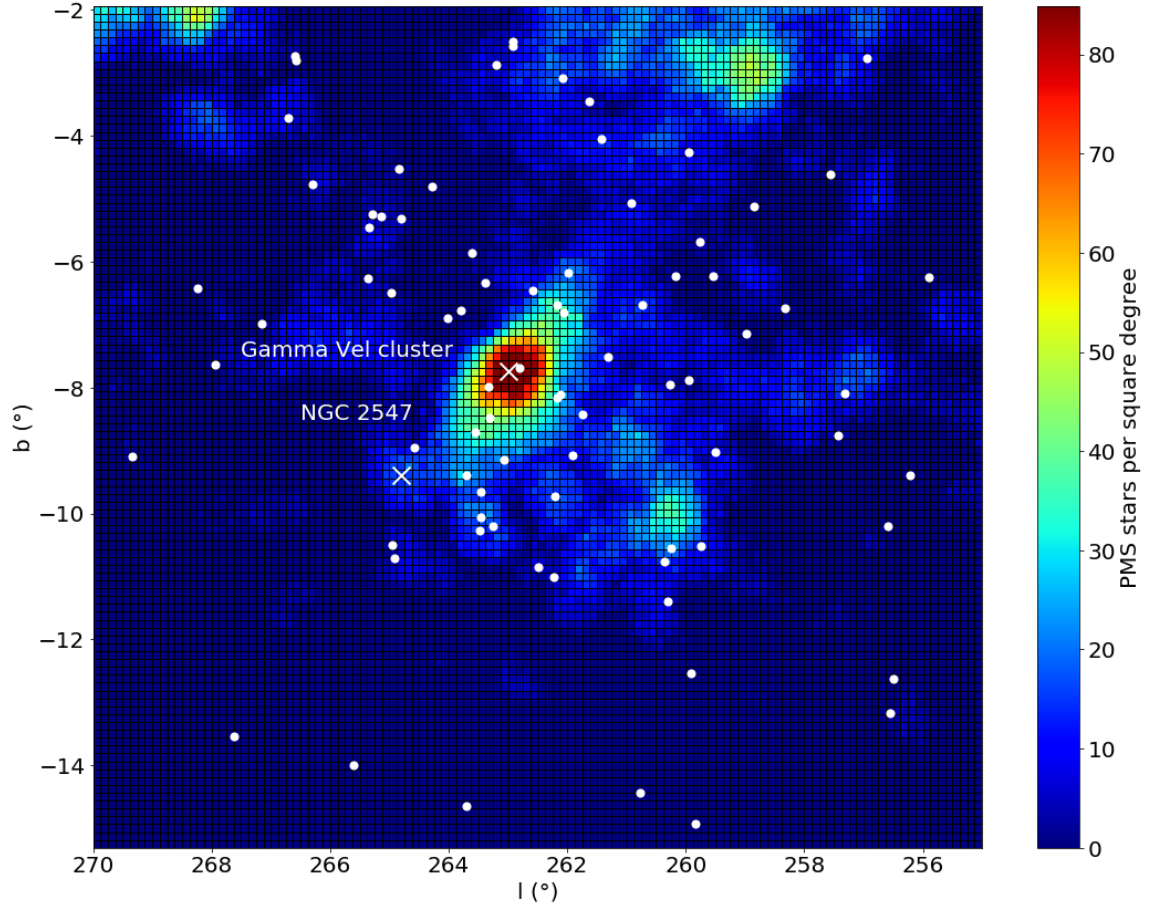
Figure 3.12: From Armstrong, Wright & Jeffries (2018), PMS density map of the area around Vela OB2, with the Besançon model contaminant level subtracted and with the 82 OB members (de Zeeuw et al. 1999) in white. The γ Vel cluster is clearly visible as the high density area in the centre of the map. We also mark the position of the NGC 2547 cluster which we have subtracted from the density map.

young objects at much greater distances.

3.4.1   Analysis of the density map

Figure 3.12 shows that our photometric YSO selection method has successfully detected a widespread population across the Vela OB2 region. This is in good agreement with Sacco et al. (2015), who speculated the existence of a widespread PMS population with similar kinematics to the γ Vel cluster.

We calculated the numbers of PMS stars shown in the final density map (Fig. 3.12). 4882 Gaia+2MASS sources are selected in total, giving 995 PMS stars after applying background subtraction. The differences between our IMF predictions and density map estimations are reasonable given the uncertainty over the low-mass form of the IMF.

It is also apparent from Figure 3.12 that the high-mass stars are not preferentially located in areas with high densities of low-mass stars. In particular, we noted that the two dense regions at (l = 260.25°, b = -10.25°) and (l = 259.0°, b = -3.25°) have no high-mass stars within them, whilst the high-mass stars at the lowest latitudes appear isolated from the low-mass population. The latter may be associated with the star forming region RCW38 in the Galactic plane, though younger regions near the Galactic plane are unlikely to be selected because they will be reddened out of the H-K v J-H selection box, but the former region appears to be a previously-unknown cluster of low-mass stars.

In order to estimate a statistical significance to the difference in the distributions of the high- and low-mass populations in Fig. 3.12, a two sample Kolmogorov-Smirnov test was performed on the projected YSO density distributions of the high-and low-mass populations. We calculate the cumulative distribution of YSO densities upon which the high- and low-mass stars are projected. The cumulative distributions
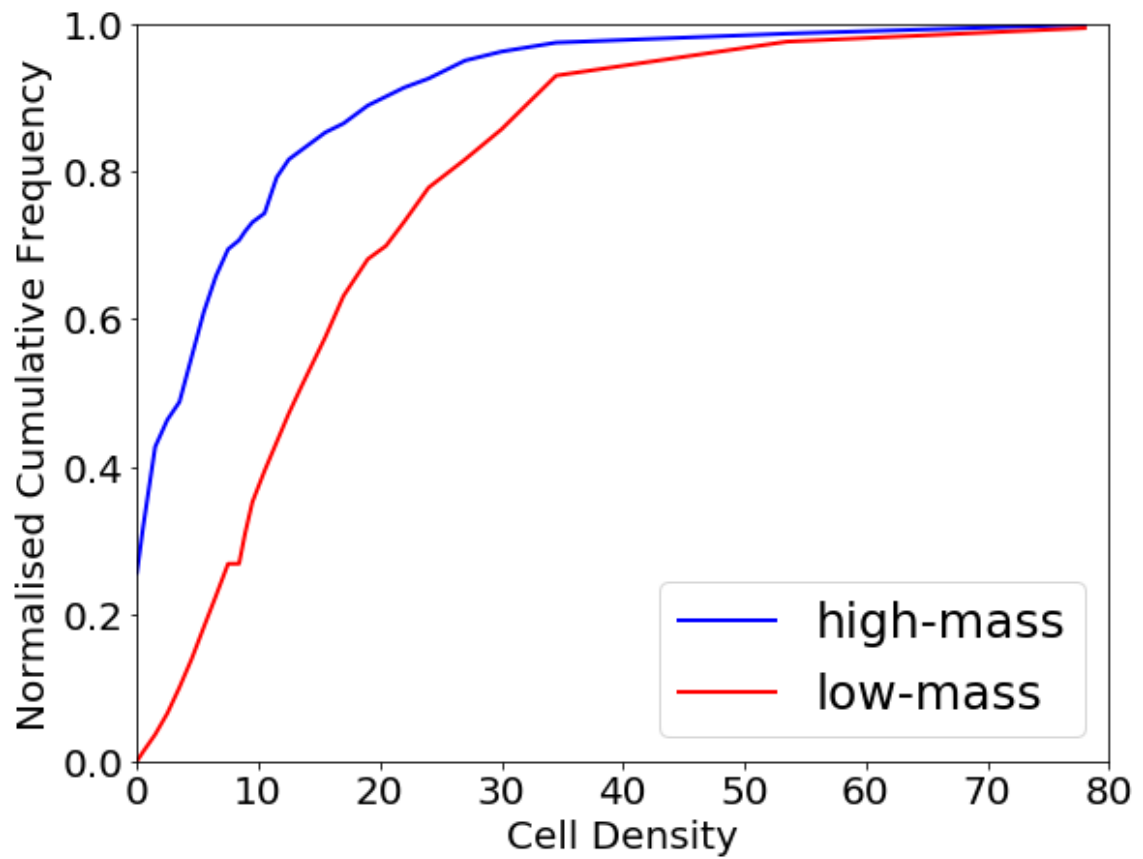
Figure 3.13: Cumulative distributions of cell densities of high-mass (blue) and low-mass (red) populations, from Armstrong, Wright & Jeffries (2018).

calculated are plotted in Figure 3.13, showing that the high-mass stars are preferentially projected against regions of low density compared to the low-mass stars, with a KS-test P-value of 0.0077, i.e. at a 99.23% confidence level. More than$\sim 26\%$ of the high-mass stars are projected against cells with low-mass PMS stellar densities of 0.

The low number of high-mass stars will introduce some stochasticity in this comparison, but we expect the effect to be small given that the high-mass population is reasonably well sampled.

3.5   Discussion

Sacco et al. (2015) found 15 stars with similar kinematics and age to the γ^2 Vel cluster members identified by Jeffries et al. (2014), but located 2 degrees (~ 10 pc) from γ^2 Velorum, well outside the area studied by Jeffries et al. (2014), and speculated that they might belong to a widespread PMS star population associated with Vela OB2. They also commented on the discrepancy between the total mass of the cluster ($\sim 100 M_\odot$) and the total cluster mass predicted by the mass of γ^2 Velorum alone ($\sim 1000 M_\odot$, Weidner, Kroupa & Bonnell 2010). Damiani et al. (2017) also identified multiple proper motion populations within the higher-mass members of Vela OB2 that they associated with γ^2 Vel and NGC 2547.

Figure 3.12 shows that our photometric selection has detected a widespread population across the whole area of the association, confirming the speculation of Sacco et al. (2015). The agreement between the numbers of PMS stars found in this mass range and the numbers predicted by a standard IMF suggest we have identified the low-mass content of Vela OB2. It shows notable concentrations around γ^2 Vel and the NGC 2547 cluster, but Fig. 3.12 shows that in general the high mass stars

are not closely correlated with the location of the PMS stars.

There are a few possible explanations for the different spatial distributions of the low- and high-mass stellar population: (a) either the high-mass stars were born in relative isolation - in regions with IMFs that are quite different to the canonical IMF; (b) the high mass stars have moved away from the low-mass population (in many cases) on timescales of ~ 10 Myr; or (c) that members of the high-mass population do not belong to Vela OB2, but to other populations which are not sensitive to given the choices of distance and age that are used to identify this low-mass population.

Using this photometric selection method we have successfully detected $\sim$1000 likely PMS stars across a 225 square degree area, including 3 open clusters. The success of this method in identifying stars in a narrow range of distance and age demonstrates its potential usefulness for identifying stellar populations in other regions, given a pre-existing sample to calibrate the selection criteria. In particular, other nearby associations with samples of known members may be studied in similar detail to this study, allowing us to learn about the distribution and structure of low-mass populations in multiple associations. The work in this chapter represents one of the first investigations to combine Gaia and IR photometry to detect young PMS stars over a large area of sky.

After these results were published in Armstrong, Wright & Jeffries (2018), Cantat-Gaudin et al. (2019a) used Gaia DR2 astrometry to identify 7 distinct populations in the Vela-Puppis region, the youngest of which (population VII) includes the γ Vel cluster and most of the Vela OB2 members of de Zeeuw et al. (1999). The spatial distribution of this population strongly correlates with the distribution of PMS stars shown in Fig. 3.12 supporting the approach we used. The cluster NGC 2547 and therefore the PMS sources we removed from Fig. 3.12 are included in their population IV, which is older and more distant then population VII, consistent with NGC 2547 being older and more distant than γ Vel. A more detailed comparison to this study is made in Section 6.2.2.

4 Spectroscopic observations of YSOs in Vela OB2

This chapter contains a description of the target selection and observation of candidate YSOs across Vela OB2. Observing time was obtained on the Australian Astronomical Telescope (AAT) in service time in January 2018 and in visitor mode in January 2019. Analysis of the data are presented in Chapters 5 and 6.

Most of the material in this chapter is taken from Armstrong et al. 2020.

4.1 The 2018 sample of spectra

In our photometric selection for creating the density map we expect that the majority of selected objects will be PMS stars at the distance of the association, but we still expect some amount of contamination. Our sample of association members can be cleaned further by selecting stars with a significant photospheric Li abundance, determined by measuring the Li equivalent width, EW(Li), which is a known indicator of youth in PMS stars (see Section 1.4). To measure the Li equivalent width and and also measure radial velocities (RVs) to complete our kinematic data for these stars, we need to obtain spectroscopy.

4.1.1 The AAT

To obtain spectroscopic data for stars located in the southern hemisphere, we applied for observing time on the AAT using the 2 Degree Field (2dF; Lewis et al. 2002) and High Efficiency and Resolution Multi-Element Spectrograph (HERMES; Sheinis
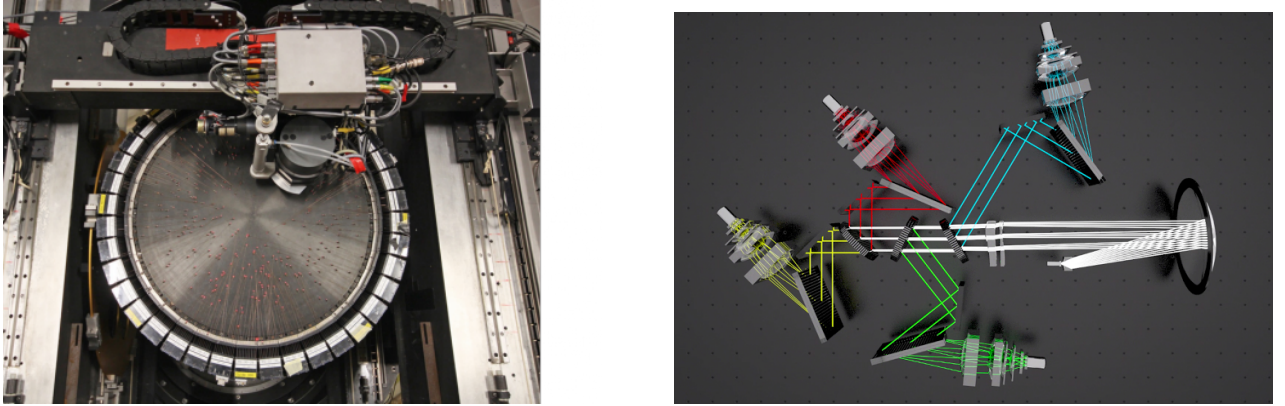
Figure 4.1: *Left* : The robotic arm of 2dF places optical fibres on a field plate. Credit: Ángel R. López-Sánchez *Right* : A model representation of HERMES showing how the light is split and channeled down 4 paths for the different optical bands. Credit: AAO.

et al. 2015) instruments.

2dF is the fibre positioning instrument that places the magnetic mounts at the ends of the optical fibres onto a field plate with a precision of 0.3 arcseconds (Fig. 4.1). There are two field plates, which allows fibres to be positioned on one while the other is being used for observing. HERMES consists of two plates each with 400 fibres to be configured for observing 360-370 science targets at a time, as well as the necessary sky fibres for calibration.

4.1.2 Target selection

Targets were selected from Gaia DR1 within a 2 degree diameter field centered on l = 262.8°, b = -7.7° (see Fig. 4.2), which overlaps the GES γ Vel field as seen in Fig. 4.3, as well as a field centered on NGC 2547 (l = 264.4°, b = -8.9°) and a third field centered on the P Puppis cluster at l = 260.4°, b = -10.3° (Fig. 4.2). These 3

fields are the areas of highest density of PMS stars in our density map (Fig. 3.12). Targets in these fields are required to have Gaia-magnitudes (G) within the range $14.5-17.5$ mag, as the 2dF manual recommends that targets are within a 3 mag range for instrument effectiveness. They were then matched by position with the 2MASS catalogue (Skrutskie et al. 2006) with a matching radius of 0.5 arcseconds. Sources with J, H, K photometric uncertainties > 0.05 mag or with possible contamination (as indicated by the "Cflg" flag) were excluded. We then filter these sources through a G-K vs G colour-magnitude diagram selection and a H-K vs J-H colour-colour diagram selection using the method described in Section 3.3 (Armstrong, Wright & Jeffries 2018), producing a sample of 800 likely PMS stars per field as targets for observation. We allocated these targets to 4 priority levels based on their proximity to a Baraffe et al. (2015) 20 Myr PMS isochrone in G-K vs G, and selected 350 of the highest priority targets per field for the final list (Fig. 4.2).

4.1.3   Preparing for the observations

An additional 20-30 fibres were allocated to empty regions of sky in order to measure the "sky spectra" so that it may be subtracted from the spectra measured for science targets. The method we used to determine coordinates for empty sky was to gather a list of all Gaia sources in the area of the field, select $\sim$40 sources uniformly distributed over the area, offset their positions by 1 arcsecond and cross match these new coordinates to the Gaia list. Coordinates that do not cross-match to any Gaia sources can be used as sky fibre coordinates.

Guide stars were selected from the Gaia catalogue in the magnitude range 12.5 - 13 mag.
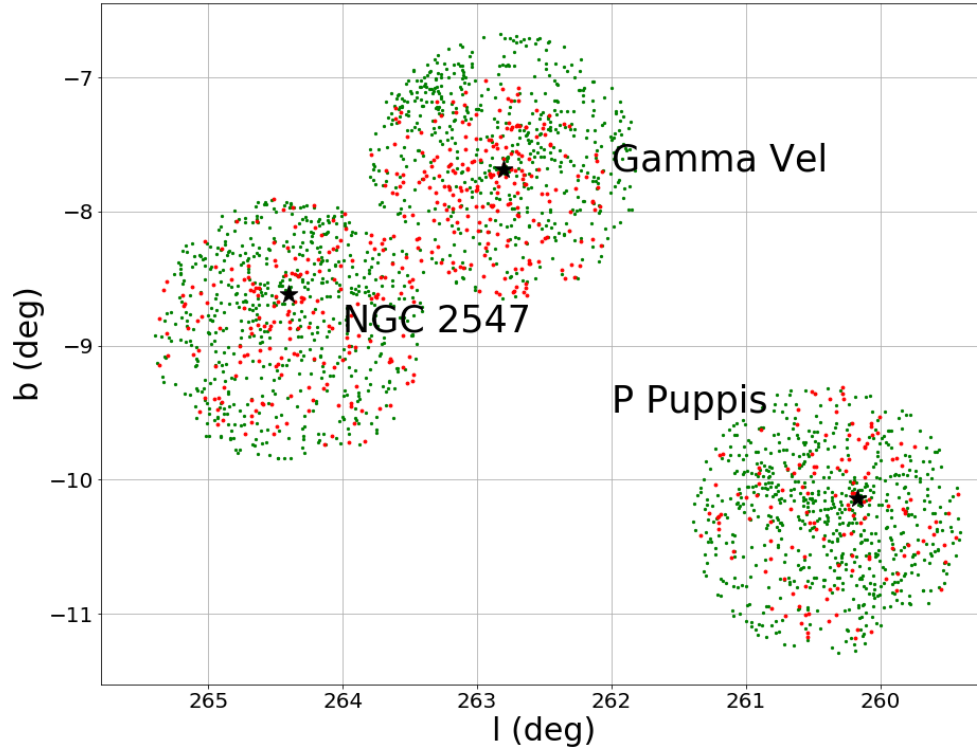
Figure 4.2: Positions of targets in 3 fields centered on the γ Vel cluster, NGC 2547 and P Puppis cluster (Caballero & Dinis 2008) as selected for our January 2018 observations. Targets are allocated high (red) or low (green) priority for the 2dF fibre-allocation software based on their proximity to the G - K PMS isochrone. In the end, the γ Vel field was the only field observed with multiple exposures.
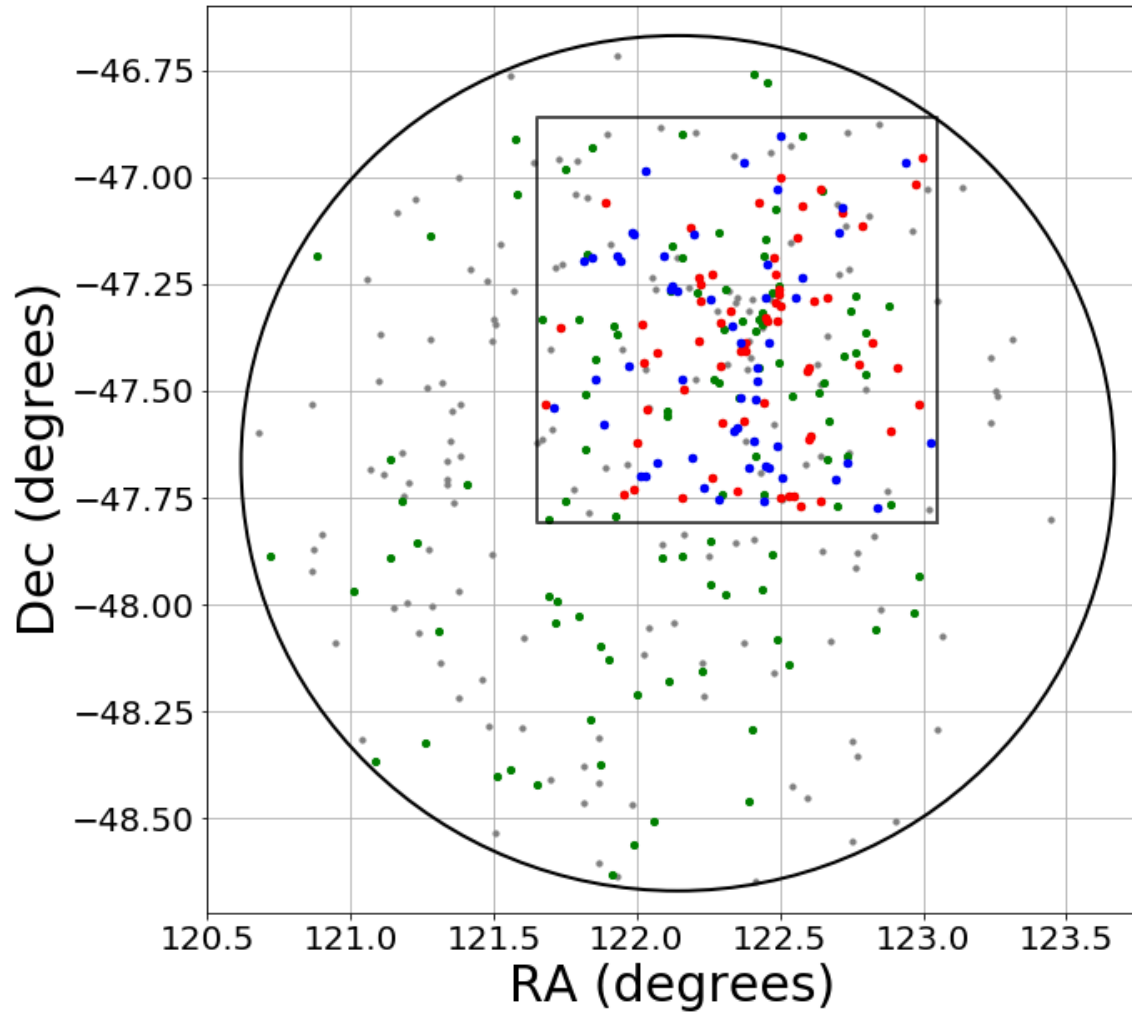
Figure 4.3: Positions of combined GES (square area) and AAT (circular area) sources. Sources with EW(Li) > 150 mÅ (green) along with population A (red, γ Vel cluster) and B (blue, Vela OB2) members with membership probabilities > 0.75 from Jeffries et al. (2014).

4.1.4 Data reduction

Due to poor weather conditions during the nights allocated for our service observing, only the field around γ Vel was observed for enough time to produce spectra of sufficient SNR. 3 x 40 minute exposures were taken for this field with 365 science targets.

Data reduction involves two main steps. Firstly is the combination of raw spectra science frames, sky spectra frames, dark frames, multi-fibre flat field frames and arc exposure frames. The Australian Astronomical Observatory (AAO) have produced a software package called 2dFdr (2dF data reduction AAO Software Team 2015) to facilitate the process of combining these frames, removing contamination and instrument bias to extract the spectra for the science targets. The software also allows a variety of settings for the model used when combining spectra from multiple exposures. We tested several settings but found that, in general, only a few made any significant difference to the output.

The sequence of the reduction process in 2dfdr is as follows:

- Debiassing: If a bias frame is available it is subtracted from the data. Bias frames were taken each night before observing (see Table 4.1 for the 2019 sample), and so were available for subtraction for all our target spectra.

- Dark subtraction: If a dark frame is available it is subtracted, after scaling for the relative exposure times. Dark frames were also taken each night before observing (see Table 4.1), and so were available for subtraction for all our target spectra. These two initial stages produce a reduced image file.

- Tramline map generation: A tramline map is a map of the fibre profile centroids on the CCD. They can be used to correct for any distortion in the spectrograph affecting image positions on the CCD. If a suitable tramline map is available it is matched with the data by determining the relative shift

between the map positions and the peaks found in the data, for a series of cuts through the image. A linear fit is performed to determine shift and rotation angle and the tramline map is adjusted accordingly. The tramline map is best produced using a fibre flat field because of their high signal-to-noise, so we used the fibre flat fields which we took for each field each night (Table 4.1) to produce tramline maps for all of our observations.

- Fibre extraction: Using the tramline map and reduced image, the spectrum of each fibre is extracted. There are two available methods. The TRAM method is a simple extraction, which sums the pixels along each fibre over a width equal to the distance between adjacent fibres (Sharp & Birchall 2010). The FITS method performs an optimal extraction by fitting profiles determined from a flat field frame and can produce better signal-to-noise than the TRAM method. We took flat field frames for each field observed each night see (Table 4.1) and so were able to use the FITS extraction method.

- Wavelength calibration: The data are rebinned onto a linear wavelength scale, which is the same for all fibres. The wavelength shift and dispersion determined from a wavelength calibration lamp exposure (arc exposure frames) are used. Lines in the exposures of CuAr, He and FeAr lamps are found by a peak finding algorithm. The wavelength shift is determined by comparing the positions of these lines to their true wavelengths and a cubic fit is performed to these, the polynomial coefficients of which are used to rebin the data per fibre. Arc frames were taken for each field observed each night (Table 4.1) allowing us to calibrate the entire sample of exposures.
The wavelength range to which the data is rebinned is determined by the central wavelength provided in the FITS header of the data frames which is itself determined by the spectrograph setup. This can lead to 10-20 bad pixels at one end of the wavelength range for all the data if this central wave-

length is slightly incorrect. However, these pixels at the end of the spectra will have a negligible effect on our derivations of RV and EW(Li) (see Section 4.1.5), as the Li 6707.8Å line is well within the wavelength range of the HERMES Red camera ($6478 - 6737$Å) and RVs are determined from a cross-correlation function spanning the whole wavelength range.

In private communication with members of the GALAH survey team (Kos et al. 2017; Martell et al. 2017) we were warned that 2dfdr can sometimes produce an unstable wavelength solution from field-to-field at the level of a few Å ($\sim 0.1 \mathrm{kms}^{-1}$) and were advised to visually inspect our reduced spectra for signs of poor calibration. Our inspection revealed no significant miscalibration.

- Sky subtraction: Per exposure, a certain number of fibres are allocated to regions of empty sky (sky fibre spectra). The data are first corrected for the relative fibre throughputs, based on a throughput map derived from the offset sky exposures or from the relative intensities of night skylines. The sky fibre spectra in the data frame are then combined and subtracted from each fibre. We visually inspected our sky spectra for quality and found no significant issues.

- Combining reduced runs: Individual runs may be combined with cosmic ray ejection, which is based on the spatial profile across a fibre. Per pixel, the spatial profile is compared with the median profile of pixels on either side of the current one, and if the profiles differ by 20σ (default) the pixel is flagged in the output spectrum.

4.1.5 Deriving equivalent widths and radial velocities

Secondly, after combining all frames and extracting the target spectra, measurement of spectroscopic parameters was done using IDL (Interactive Data Language) pipelines written by Richard Jackson, following the procedures of Jackson, Deliyannis & Jeffries (2018) and Jeffries et al. (2021) (Fig. 4.4).

We match our AAT targets by position with the Vista Hemisphere Survey catalogue (VHS, McMahon et al. 2013) and combine the VHS and 2MASS K-band measures by taking the 2MASS value for K $<$ 12 and the mean of the two measures for 12 $<$ K $<$ 13, and use the VHS magnitude for K $>$ 13. We then use Gaia DR2 G magnitudes to calculate the G - K colour for these sources and perform SED fitting using the method outlined in Section 6.1.1 to estimate effective temperatures (T_{eff}).

In order to determine RVs and EWs for the Li 6707.8Å feature, we used a spectral subtraction technique that required template spectra of similar effective temperature (T_{eff}) to the targets (but without lithium absorption) in order to isolate the contribution of Li. Target spectra are matched to template spectra with the closest T_{eff}. Templates were synthesised for $\log g = 4.5$ at 100 K steps with a minimum of 4000 K, using the MOOG spectral synthesis code (Sneden et al. 2012), with the Kurucz (1992) solar-metallicity model atmospheres. The extraction profile accounted for both the instrumental resolution, rotational broadening and offset in RV. The linelists and atmosphere models do not include the strong molecular contributions that become important at low temperatures. For that reason, the lowest T_{eff} used for the templates was 4000 K, which leads to a systematic (but consistent) zeropoint error in EW(Li) for stars cooler than this. However, this offset appears to be small (see Fig. 4.5; some sources have negative EW(Li)s, but only down to -100 mÅ and are consistent with 0 mÅ considering their uncertainties), and these EWs are accurate enough to enable the selection of Li-rich objects (see Section 5.3.3).

RVs were measured by cross-correlating the combined spectra of individual tar-
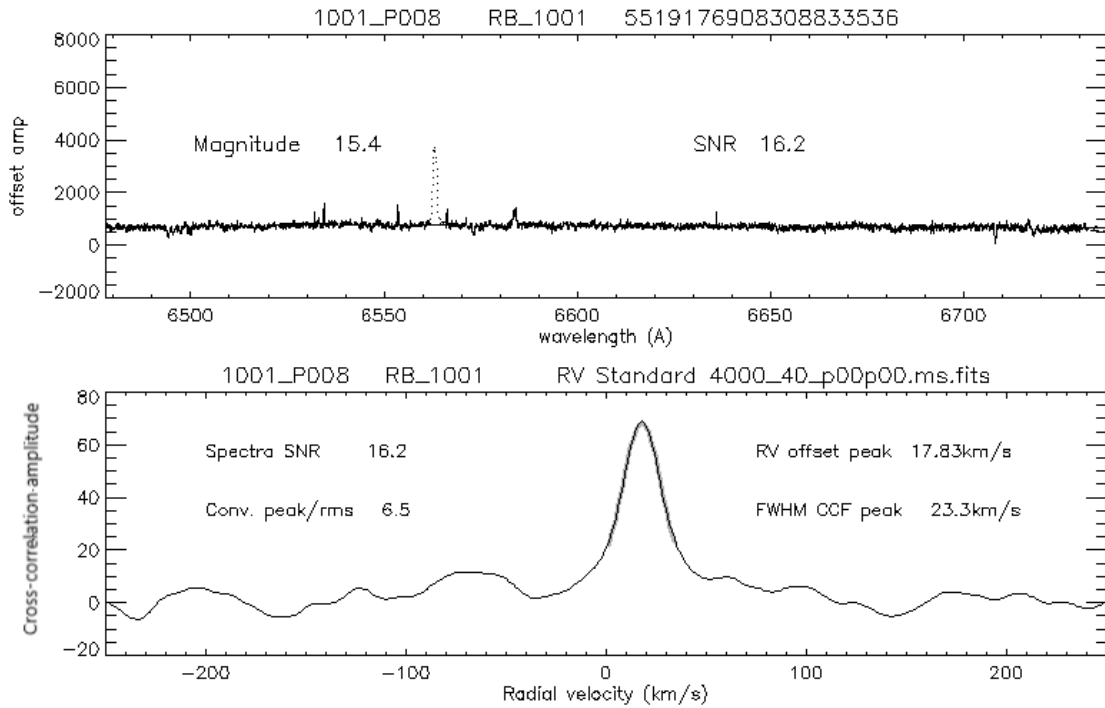
Figure 4.4: Example output of RV determination by Gaussian function fitting using Richard Jackson's IDL pipelines (Jackson, Deliyannis & Jeffries 2018). *Top* : The reduced spectrum for an example target star in our sample with the G-band magnitude and SNR of the target indicated. *Bottom* : The cross-correlation function (CCF) of the target spectrum and synthetic spectrum with a Gaussian function fit to the peak of the CCF, the position of which indicates the target's RV.

gets with the synthetic spectra and then fitting a Gaussian function to characterize the peak in the cross-correlation function (CCF). RVs were determined from the position of this peak. Sources for which a Gaussian function cannot be satisfactorily fitted to the peak in the CCF (such as spectroscopic binaries) are not given valid RVs and are rejected from our sample.

RV uncertainties were determined empirically from the change in RV between separate exposures of the same target ($E_{RV} = \Delta RV/\sqrt{2}$). The RV uncertainties are normalised per field using a scaling function

$$S_{RV} = FWHM\sqrt{A^2 + (B/SNR)^2} \tag{4.1}$$

where A and B are determined per field as the gradient and intersect of a linear best fit to $1/SNR\ vs\ \Delta RV/\Delta FWHM$. Normalised RV uncertainties are then calculated as E_{RV}/S_{RV} and these are used in the following analyses (Chapters 5 & 6).

The equivalent width of the Li 6707.8Å line (EW(Li)) was measured by subtracting the synthetic spectrum ($S_C(\lambda)$) from the target spectrum ($S_T(\lambda)$) and then integrating under the relevant profile $P(\lambda)$ as follows;

$$EW(Li) = \int[S_C(\lambda) - S_T(\lambda)]P(\lambda)d\lambda \int P(\lambda)^2 d\lambda \tag{4.2}$$

where $P(\lambda)$ is a Gaussian profile with the FWHM of the CCF. EW(Li) uncertainties are taken as the RMS value of the EWs measured using the same procedure with $P(\lambda)$ centred at five wavelengths either side of the Li 6707.8Å line. Blended with the Li line is a weak Fe I line at 6707.4Å which, though the template subtraction should account for this, may mean that EW(Li)s are underestimated by a few mÅ if the targets have subsolar metallicities.

If the SNR (signal-to-noise ratio) for a science target is low enough to indicate significantly poor quality of the spectra (SNR < 5) such that measured RVs and EW(Li)s will be unreliable, the process is halted for that target and the spectra not used for scientific analysis.
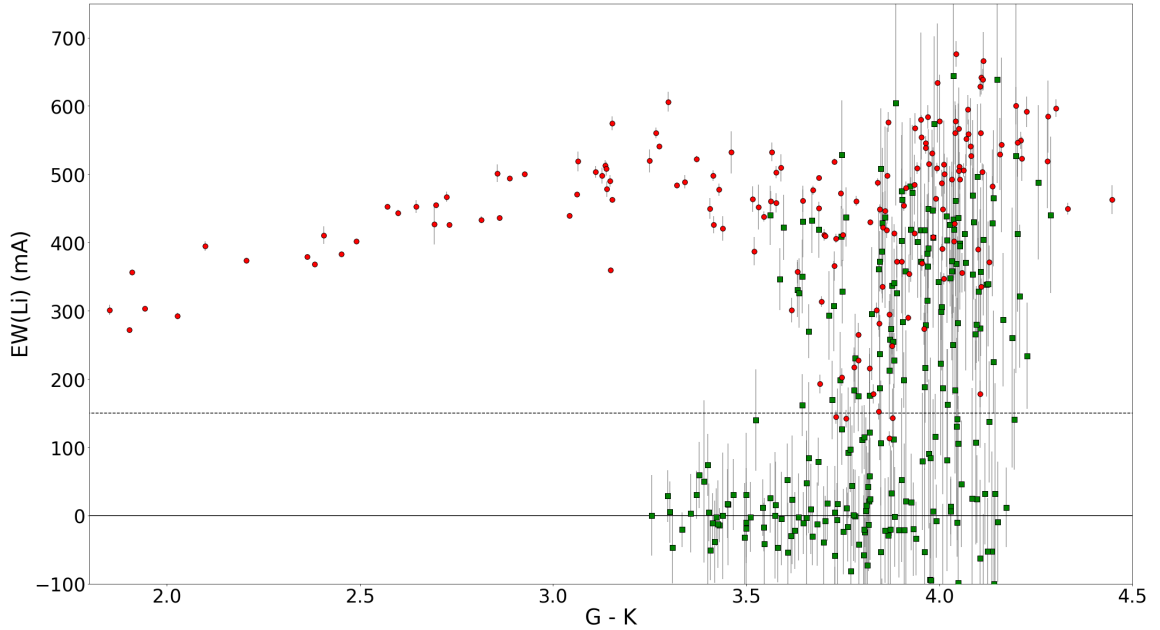
Figure 4.5: Gaia DR2 G magnitude - combined 2MASS and VHS K magnitude versus EW(Li) for 248 AAT targets (green) with 'AAA' quality (Section 3.3.1) infrared photometry and EW(Li) measurements and 170 GES members (red) from Jeffries et al. (2014) with 'AAA' quality infrared photometry. The threshold for significant EW(Li) we set at $150 \, \mathrm{m\AA}$ is shown (see Section 2.4). With the combination of the two samples, a Li depletion pattern becomes apparent with a dip in the range G-K $\approx 3.7 - 4.2$, where most of our AAT sample is located.

We obtained spectra for all targets in this field, extracting RVs and EW(Li)s for 248 (68.9%) of these with spectroscopy of sufficient quality (SNR > 5). Of these, the median uncertainty in RV is $1.88 \, \mathrm{kms^{-1}}$ and in EW(Li) is 80.26 $\mathrm{m\AA}$. The EW(Li) for these 248 targets are shown in Fig. 4.5, compared with Li-rich members of γ Vel defined in Jeffries et al. (2014). The analysis of these spectra are presented in Chapter 5.

4.2 The 2019 sample of spectra

We applied for more observing time at the AAT and were allocated 4 nights from 10-13 January 2019 to obtain spectroscopic data for PMS stars in Vela OB2. With this increase in time compared to the previous year we would be able to observe more fields across a greater area of the association to investigate the wider population of Vela OB2.

4.2.1 Improved PMS star selection

Gaia DR2 included data from Gaia's blue and red photometers G_{BP}, G_{RP}, for more than 1.38 billion objects in the catalogue, as well as parallax measurements for more than 1.33 billion. With the availability of this data for the vast majority of likely PMS stars selected by our previous CMD and CCD filters we decided to incorporate this data into an improved selection method. We created an absolute CMD using G_{BP} - G_{RP} as the colour axis, and absolute G magnitude as the magnitude axis and designed a selection box on this diagram to be used as the primary filter. We also employed a parallax cut, removing objects with $\varpi > 4$ and $2 > \varpi$ (respectively for sources with > 500 pc and < 250 pc), effectively eliminating foreground and background contamination. These new selection criteria eliminate the need to use the 2MASS catalogue in conjunction with Gaia, which allows us to select objects that were either not present in the 2MASS catalogue or had large uncertainties in 2MASS photometry. Furthermore, the parallax cut is effective at eliminating background contamination and thus removes the need for a contamination estimate with the Besançon Galaxy model. As a result, a density map produced by the new selection method (Figs. 4.6, 4.7) shows a slightly different picture to the DR1 + 2MASS version (Fig 3.12). The three open clusters in the region (γ Vel, NGC 2547 and P
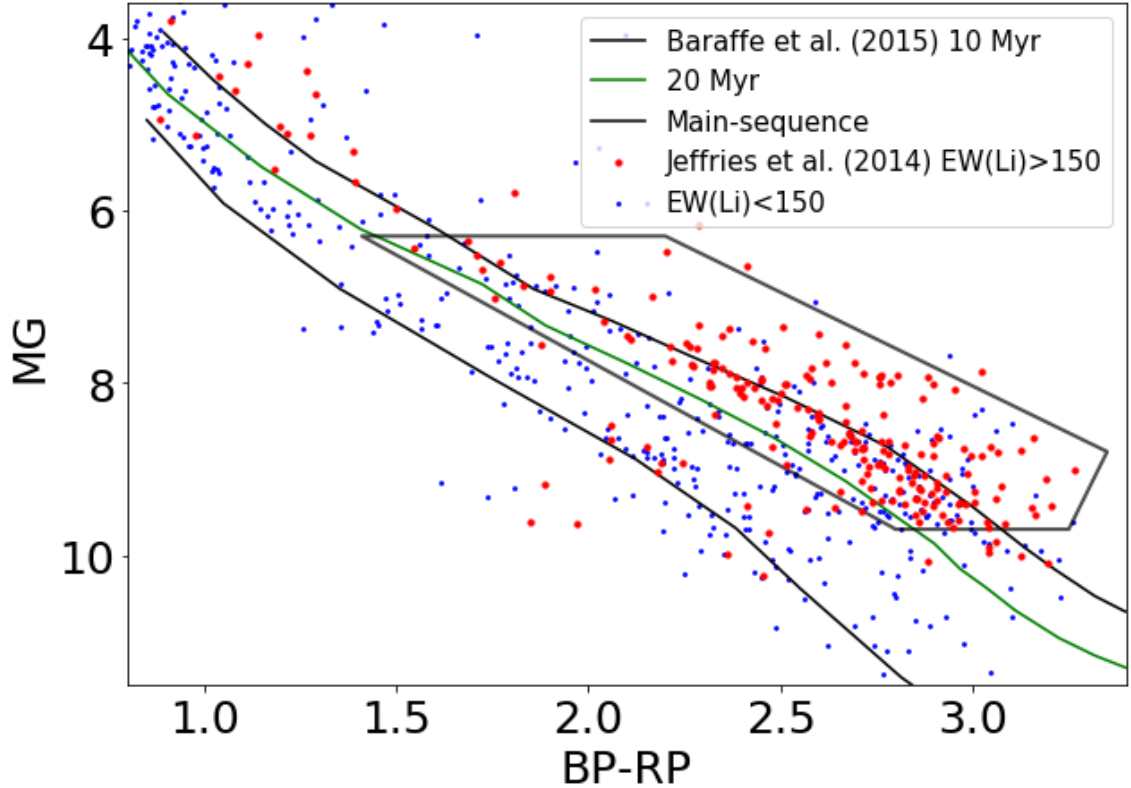
Figure 4.6: A Gaia DR2 BP-RP vs MG colour - absolute magnitude diagram showing sources from Jeffries et al. (2014) with EW(Li)$> 150\,$mÅ (red) and EW(Li)$< 150\,$mÅ (blue) using distance estimates from Bailer-Jones et al. (2018), compared to 10 and 20 Myr PMS isochrones (Baraffe et al. 2015). The PMS selection box shown is designed to surround the majority of confirmed YSOs (red) above the 20 Myr (Baraffe et al. 2015) isochrone within the range $6.5 < MG < 9.5$. This selection box is used to produce the updated density map (Fig. 4.7).

Puppis) are the highest density areas detected. Regions of moderate density at $b \approx 2°$ in Fig 3.12 are no longer detected, likely due to the use of the parallax cut.

This density map shows the γ Vel cluster and NGC 2547 as the densest regions of PMS stars, as well as a smaller cluster to the east (l = 260° , b = -10°) which
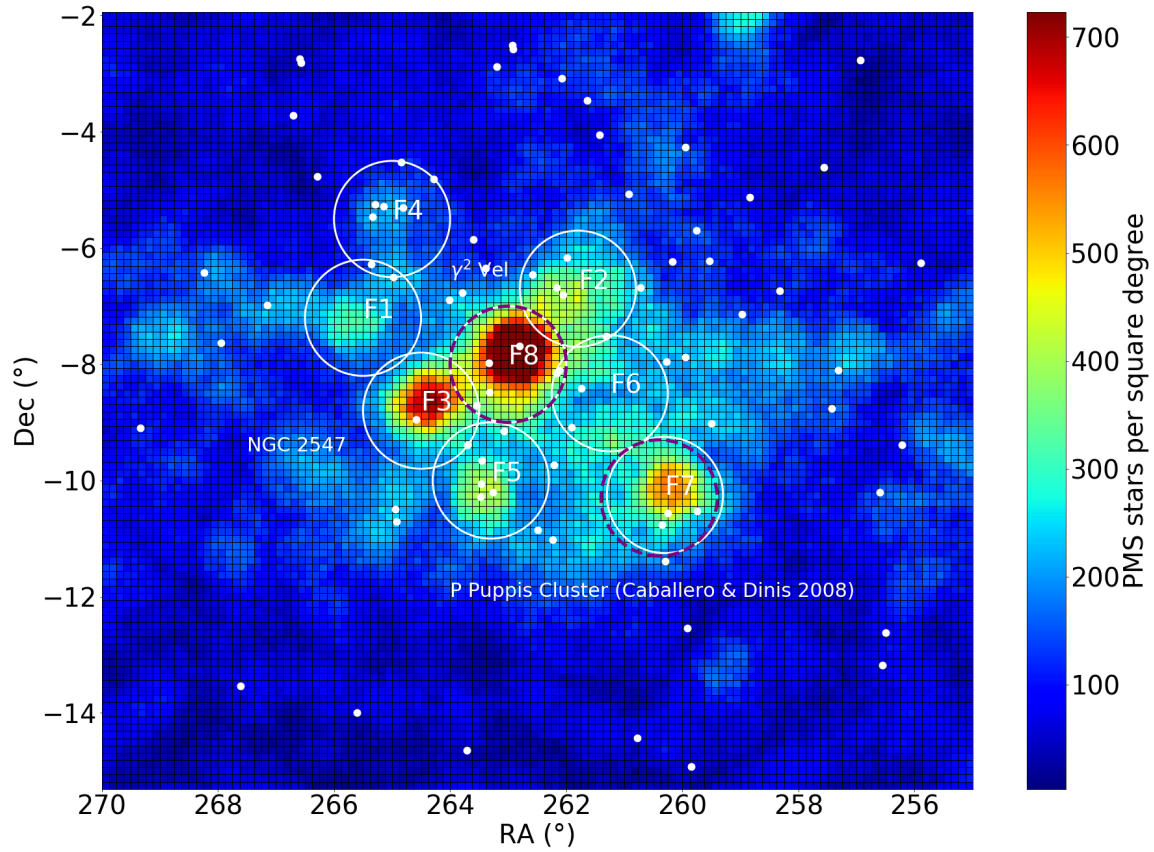
Figure 4.7: A density map produced using Gaia DR2 G_{BP}, G_{RP} and G band photometry as well as parallaxes. Vela OB2 members (de Zeeuw et al. 1999) are shown as white dots. Fields chosen for observation are shown by white circles, the fields previously observed in 2018 are shown by dashed circles and the GES field of γ Vel is shown by the white square.

seems to coincide with the P Puppis cluster identified by Caballero & Dinis (2008), and perhaps another small cluster at l = 263.5°, b = -10°. There does not appear to be a general correlation between the high regions of PMS stars and the locations of the OB association members.

4.2.2 Target selection

Using this density map we selected the positions for 8 target fields (white circles in Fig 4.7), covering all regions of high PMS star density. For each field we aimed to select 360 - 370 targets to make use of all available fibres on 2dF. Using published distances estimated from DR2 parallaxes (Bailer-Jones et al. 2018) we plotted sources within the 8 fields on a colour - absolute magnitude diagram (CaMD). Targets were separated into 4 priority groups per field based on their proximity to the 10 Myr PMS in the CaMD (Fig 4.8). Preparation of the instrument configuration files followed the same procedure as in Section 4.1.3.

4.2.3 Observations

Over the four observing nights at the AAT, we had overall good conditions with little cloud cover, and an instance of instrument failure on 11 January which was resolved within 2 hours (see Table 4.1). We successfully obtained multiple exposures for all 8 fields and took additional exposures for the fields we deemed had the most scientific interest (fields 6 and 7).
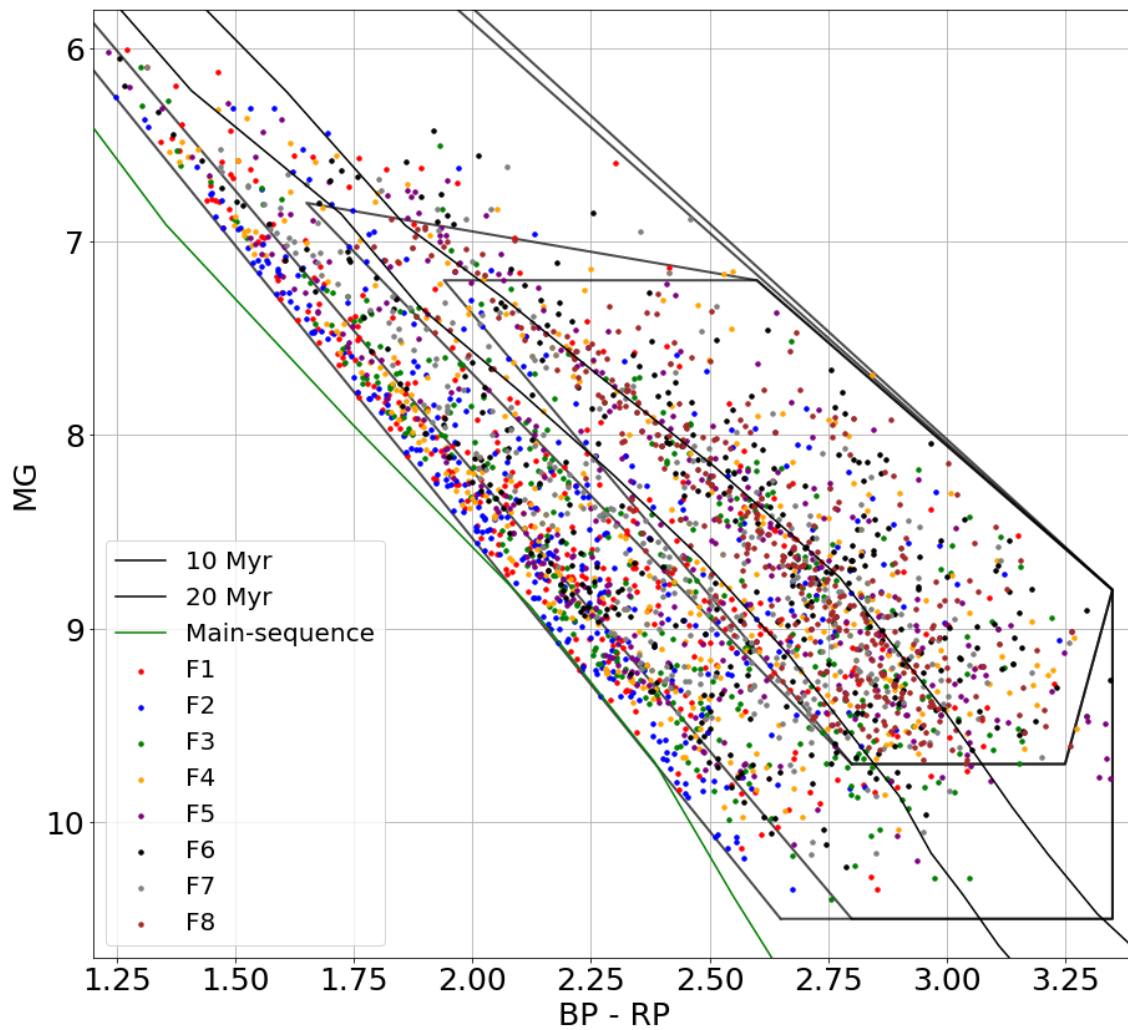
Figure 4.8: A colour - absolute magnitude diagram showing likely PMS targets selected from each of the 8 fields and using distance estimates from Bailer-Jones et al. (2018), compared to 10 and 20 Myr PMS isochrones (Baraffe et al. 2015). The four quadrilaterals indicate the four priority levels for targets, the smallest area contains highest priority targets, the largest area lowest priority. The coloured points indicate which fields the targets are selected from.

Date	Field	Run	Obs Type	Blue	Green	Red	Seeing	Local Time	Notes
10/01/2019		3 - 23	BIAS	0				16:15	
		24	DARK	2400				20:30	
		25	BIAS	0				21:40	
		26 - 29	DARK	2400				21:42	Clouds
	Field 6	30	OBJ	2400				01:42	
		31	OBJ	2400				02:23	
		32	OBJ	2400				03:05	
		33	OBJ	2400				03:46	
		34	ARC	180				04:29	
		35	FLAT	180	120	90		04:34	Twilight
11/01/2019		1 - 6	BIAS	0				16:15	
		7 - 15	DARK	2400				16:35	
	Field 5	16	ARC	180			1.5"	00:15	
		17	FLAT	180	120	90		00:19	
		18	OBJ	2400				00:30	HERMES crash
	Field 6	19	OBJ	2400				02:58	
		20	OBJ	2400				03:39	
		21	OBJ	2400				04:21	
		22	ARC	180				04:52	
		23	FLAT	180	120	90		04:55	
12/01/2019		1 - 10	BIAS	0				16:28	
		11 - 15	DARK	2400				16:54	
		16	DARK	2400				20:15	Might be affected by twilight light
	Field 5	17	ARC	180			1.2"	21.04	
		18	FLAT	180	120	90		21:08	
		19-20	OBJ	2400				21:24	
	Field 4	21-23	OBJ	2400				22:50	
		24	ARC	180				00:53	
		25	FLAT	180	120	90		00:57	
	Field 3	26-28	OBJ	2400				01:03	
		29	ARC	180				03:07	
		30	FLAT	180	120	90		03:12	
	Field 7	31-32	OBJ	2400				03:16	
		33	ARC	180				04:39	
		34	FLAT	180	120	90		04:44	
13/01/2019		1 - 11	BIAS	0				16:18	
		12 - 15	DARK	2400				17:40	
	Field 7	16	ARC	180			1.2"	21.04	
		17	FLAT	180	120	90		21:08	
		18	OBJ	2400				21:24	
		19	OBJ	1200				21:24	
	Field 8	21-23	OBJ	2400				22:50	
		24	ARC	180				00:53	
		25	FLAT	180	120	90		00:57	
	Field 1	26-28	OBJ	2400				01:03	
		29	ARC	180				03:07	
		30	FLAT	180	120	90		03:12	
	Field 2	31-32	OBJ	2400				03:16	
		33	ARC	180				04:39	
		34	FLAT	180	120	90		04:44	

Table 4.1: Table displaying specifications of observations, including the date of observation, the field observed (see Fig. 4.7 for location), the number of the exposure(s), the type of frame observed, durations of exposure (seconds) for colour bands, seeing / visibility, local time at beginning of exposure(s) and notes on problems experienced.

4.2.4 Data reduction

Reduction of the spectra to obtain RVs and EW(Li)s followed the same process as explained in Section 4.1.4. Sources in the overlap regions of the 8 fields which were observed in multiple fields were reduced for each field and their RVs and EW(Li)s were combined by taking a weighted mean (Section 5.1.1). This gave us 1972 out of 2680 unique sources with spectroscopic RVs and EW(Li)s. The analysis of the 2019 observations is presented in Chapter 6.

4.2.5 Data Calibration

There is an RV offset of 1.21 kms^{-1} between the 2018 sample and sources in the GES sample of γ Vel (see Section 5.1.1). Offsets between RVs from different samples can be due to differences in the zero points of the instruments used or to differences in calibration of spectra and methods used to calculate RVs. For example, Simpson et al. (2017) found differences in RV measurements of order $\sim$1 kms^{-1} between observations using HERMES and AAOmega. Also Huang et al. (2018) found systematic RV offsets of -2.6 kms^{-1} and -3.92 kms^{-1} between APOGEE and LAMOST pipelines LSP3 and LASP respectively, which they attribute to differences in wavelength calibration. On the other hand, RVs measured as part of the GALAH survey (Zwitter et al. 2020; Buder et al. 2021), which also uses the HERMES spectrograph, have very little offset from RVs from Gaia and APOGEE, though the authors have indicated (in private communication) that there is a noticeable offset between GALAH and GES RVs. This suggests that a likely source of the RV offset we find between our AAT and GES RVs is due to the calibration of the GES sample.

We also compare RVs and RV uncertainties for sources observed multiple times in our AAT samples. Firstly, there are 36 sources which are located in overlapping regions between fields in the 2019 sample with valid RVs and RV uncertainties
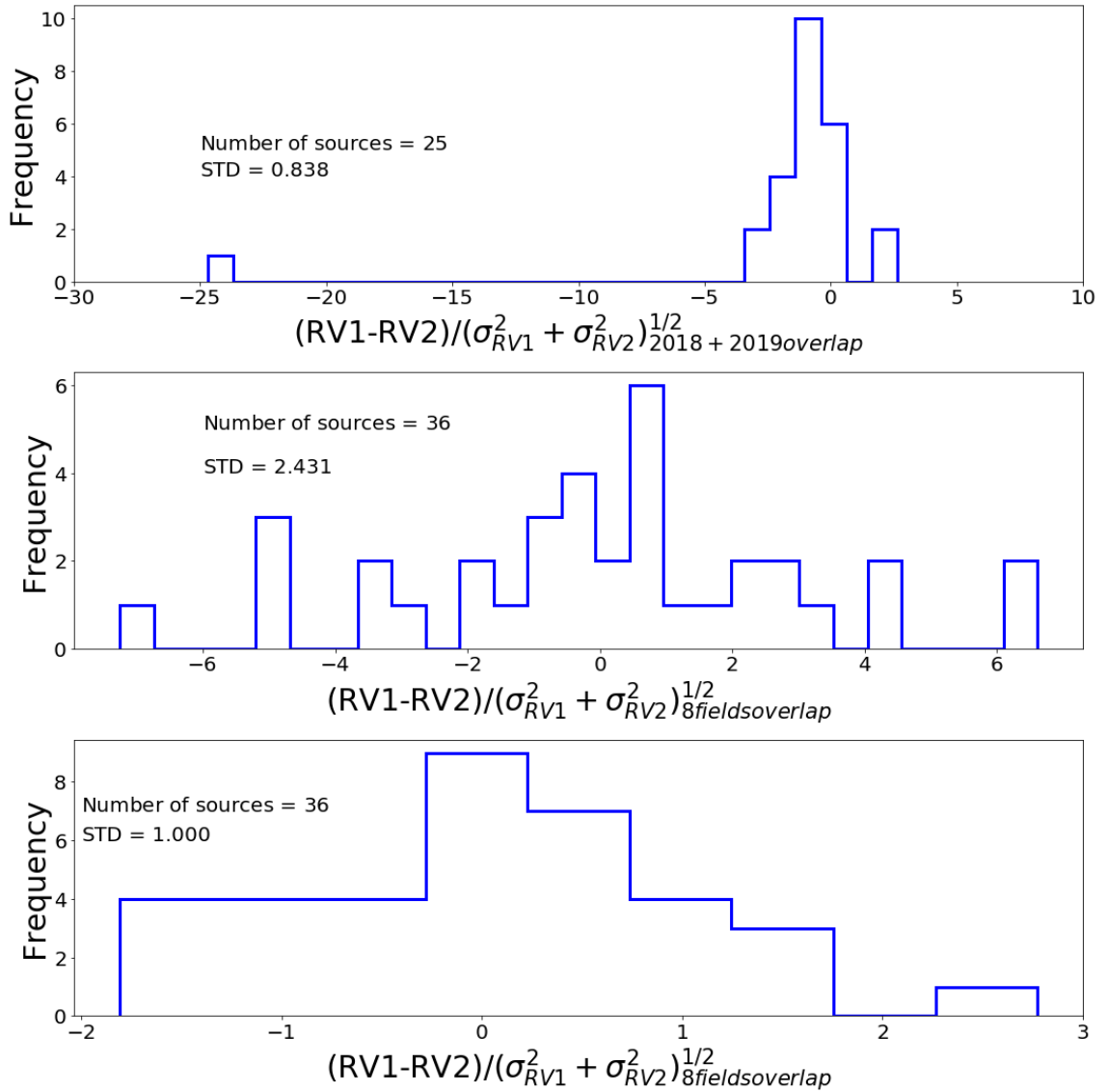
Figure 4.9: *Top* : Histogram showing the differences in RV measurements scaled by their combined uncertainties for the 25 sources observed in both the 2018 and 2019 samples with valid RV uncertainties. The number of sources and the standard deviation of the scaled RV difference are shown. *Middle* : Histogram showing the differences in RV measurements scaled by their combined uncertainties for the 36 sources observed in multiple fields of the 2019 sample with valid RV uncertainties. *Bottom* : Histogram showing the differences in RV measurements scaled by their combined uncertainties for the 36 sources observed in multiple fields of the 2019 sample with valid RV uncertainties after applying an additional uncertainty factor of 0.575 kms^{-1}.

derived separately from exposures of each field. The standard deviation of the scaled RV difference (standardised difference) is 2.431 with the uncertainties calculated using the method described in Section 4.1.4. If the RV uncertainties of the multiply observed sources were calibrated, we would expect to see the standard deviation of this standardised difference ≈ 1, so a standard deviation of 2.431 indicates that RV uncertainties in the 2019 sample are underestimated, possibly due to calibration error. In order to correct this, an additional factor of uncertainty $= 0.575$ kms^{-1} has been added in quadrature to bring the standard deviation $= 1$ as shown in Fig. 4.8. The median is close to 0 and the distribution approximately Gaussian, indicating that there is no substantial bias between multiple observations in this sample.

In order to check that radial velocity measurements are consistent between the 2018 and 2019 samples and between individual fields in the 2019 sample, we compare the radial velocities and uncertainties of sources which are observed in both samples and sources observed in multiple fields in the 2019 sample. There are 25 sources which were observed in both the 2018 and 2019 samples with valid RVs and RV uncertainties in each sample. In Fig. 4.9 we show a histogram of the difference between RV measurements for a source, scaled by the combined uncertainties of each measurement. The standard deviation of the difference in RVs being consistent with 1 (= 0.838) suggests that after the RV uncertainty correction applied to the 2019 sample, these samples are now in good agreement.

5 Analysis of the 2018 data: Dynamics of the Vela OB2 association

Most of the material in this chapter is taken from Armstrong et al. (2020) with some results updated using revised techniques. Here we discuss combining the GES and AAT spectra to analyse the dynamics of stars in Vela OB2 with a particular focus on the expansion of the association.

5.1 Sample compilation and identification of young stars

In Jeffries et al. (2014) two kinematic populations were identified in the GES γ Vel field using spectroscopic RVs. In order to best analyse the kinematics of these populations we want to distinguish between them using a combination of GES RVs, our new AAT RVs and Gaia DR2 astrometry.

5.1.1 Combining the spectroscopic data

We take the GES sample of the γ Vel cluster (Jeffries et al. 2014) of 208 sources in a 0.9 square degree area and concatenate this with our AAT sample of 248 sources. 52 sources have repeat observations in both GES and AAT samples and have measurements of RV and EW(Li) for both, so we calculated mean values weighted by the square of the inverse measurement uncertainty. We removed 8 sources with $> 3\sigma$ difference between GES and AAT RV measurements that suggested these were binary systems and measured a median offset of 1.21 kms^{-1} between GES and AAT RV measurements for the remaining 44 sources. Since measurements from the GES

sample have lower RV uncertainties than our AAT measurements, we add this median RV offset to all AAT RVs to bring the samples into agreement. At this stage we have a sample of 396 unique sources with spectroscopic RVs and EW(Li).

5.1.2   Gaia DR2 data

On 27th April 2018 the second Gaia data release (DR2) became available, containing proper motion and parallax data for $\sim 97\%$ of our sample. 12 sources lack DR2 5-parameter astrometry so we discard these. Sources were matched to the Gaia DR2 catalogue and then filtered on the suggested quality criteria to avoid using sources with spurious astrometric solutions (eqs. 1, 2 and 3 from Arenou et al. 2018). We also calculate renormalised unit weight error (RUWE) values for these sources (using Gaia DR2 RUWE data, see technical note GAIA-C3-TN-LU-LL-124-01) and discard those with RUWE > 1.4 as advised by Lindegren et al. (2018b). Removing these leaves 341 unique sources with spectroscopic RVs, EW(Li) and 5-parameter astrometry.

5.1.3   Selection of young stars

Distance estimates were taken from Bailer-Jones et al. (2018) for all 341 sources with clean and complete spectroscopy and astrometry and these are shown in Fig. 5.1 for the 327 sources with distance < 600 pc, plotted against their EW(Li). There is a clear group apparent at 300 - 400 pc with significantly higher EW(Li) measurements than the rest of the sample that suggests these are young stars at the distance of the γ Vel cluster. The distinction between the young stars and the contaminating field stars becomes unclear for EW(Li) < 150 mÅ. In Jeffries et al. (2014), the criterion
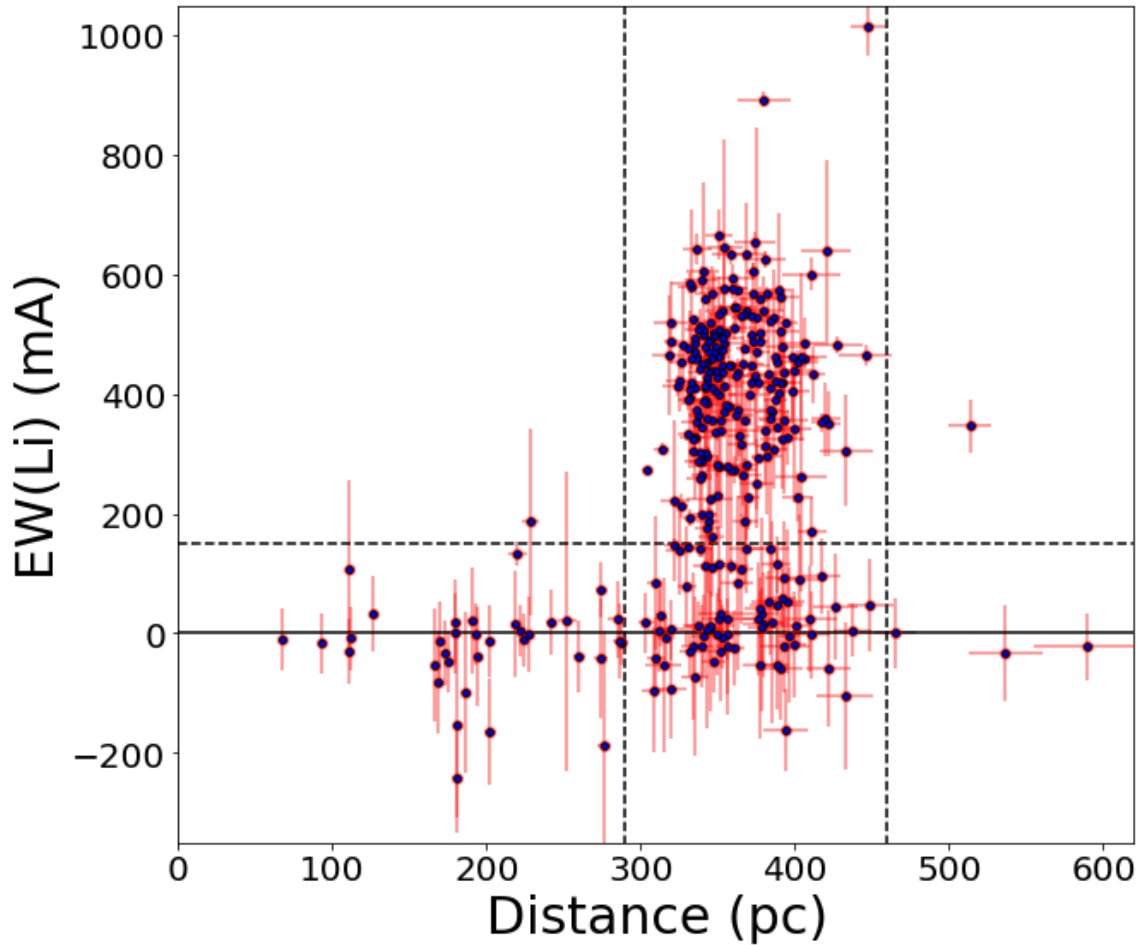
Figure 5.1: Distance estimates from Bailer-Jones et al. (2018) versus measured EW(Li) for 327 sources with distance < 600 pc from the combined sample of AAT targets and sources from Jeffries et al. (2014). The clear group between 290 - 460 pc with significant EW(Li) (>150 mÅ) are likely young stars in Vela OB2.

for GES sources to be considered young stars was EW(Li) $> 100 \, \text{mÅ}$, but since our AAT measurements have a lower precision than the GES data we set the threshold at $150 \, \text{mÅ}$ (see Figs. 4.5 and 5.1). There could be a few highly Li-depleted objects that are filtered out from the sample at this stage, though they are likely $< 10\%$ of γ Vel cluster members (Prisinzano et al. 2016; Jackson et al. 2020). We end with a sample of 216 unique Li-rich sources with full DR2 astrometry and spectroscopic RVs for our analysis.

5.1.4   Separating γ Vel and Vela OB2

Since we decided to use data cuts to separate the two populations, we use the Jeffries et al. (2014) membership information as a guide to help identify the differences in position and velocity between the two populations, and then define the boundaries using our new, larger sample.

We start by plotting RV against parallax for Li-rich (EW(Li)$> 150 \, \text{mÅ}$) sources in our combined sample (Fig. 5.2 *top*). We expect that this is where we will see the clearest separation between members of the two populations since Jeffries et al. (2014) first noticed the two-components in RV. Also throughout recent literature it has been established that γ^2 Vel itself (and thus likely the cluster around it) is significantly closer than the Vela OB2 association (γ^2 Vel - 334^{+40}_{-32} pc; van Leeuwen 2007, 336^{+8}_{-7} pc; North et al. 2007, Vela OB2 - 410 ± 11 pc; de Zeeuw et al. 1999).

In Figure 5.2 the two populations defined by the high probability members of Jeffries et al. (2014) are quite distinct. Population A (red) occupies a small, densely packed range in both RV and parallax, correlating with the small distance range occupied by Li-rich stars shown in Fig. 5.1, whereas members of population B are more sparsely distributed across a wider range in each axis.

Based on previous estimates of distance to the γ Vel cluster and Vela OB2, and
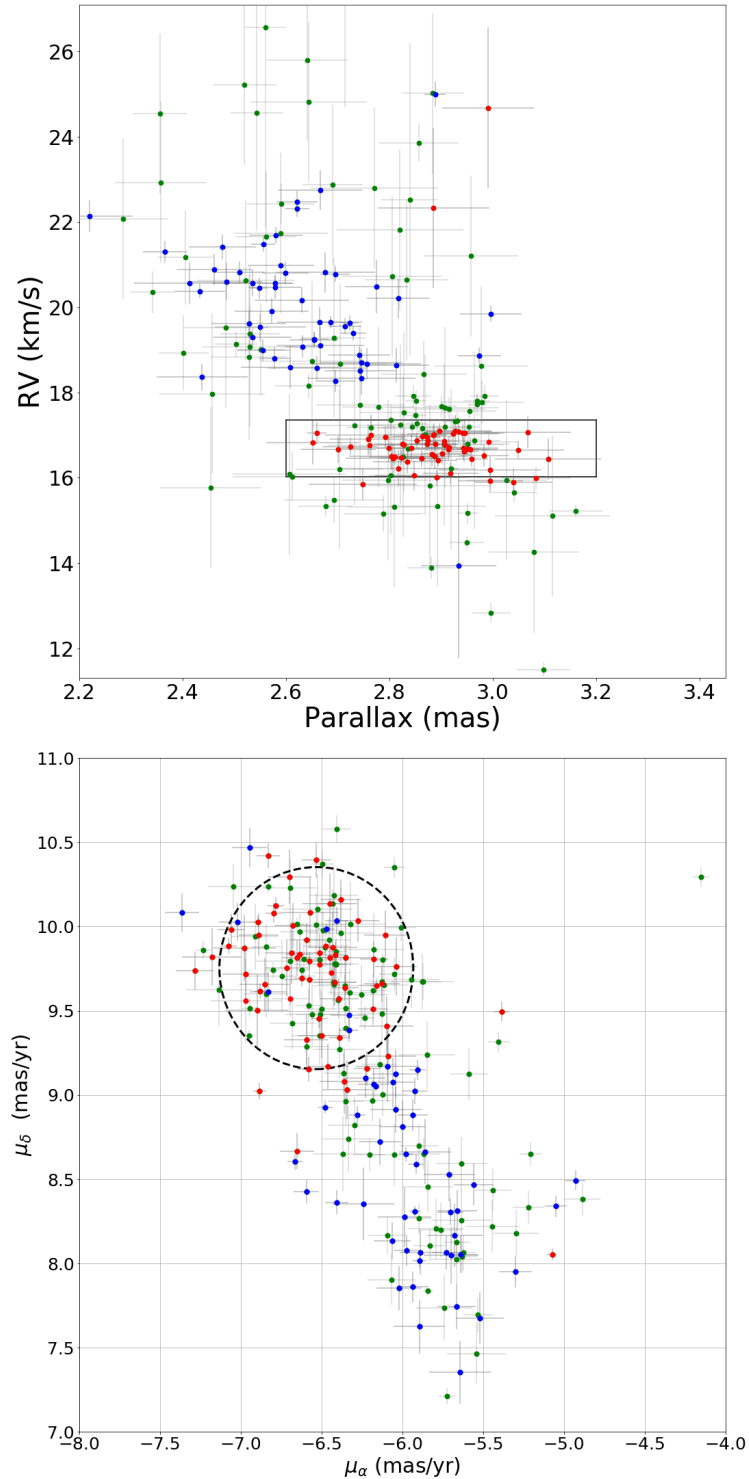
Figure 5.2: *Top* : Parallax vs RV of sources with EW(Li) > 150 mÅ (green) from our spectroscopic survey along with population A (red) and B (blue) from Jeffries et al. (2014), showing the boundaries we use to allocate sources to population A. 15 sources are beyond the RV range shown. *Bottom* : Gaia DR2 proper motions of the same sources, with a dashed circle showing the radius used to allocate sources to population A.

the parallax range occupied by Li-rich stars in Fig. 5.2 *top*, we require that sources be within $2.2 < \varpi < 3.45$ mas ($\sim 290 - 455$ pc) to be included in the analysis. This requirement is already fulfilled by all the high probability members of Jeffries et al. (2014), therefore we believe that it is a safe limit to impose in order to remove sources with distances inconsistent with γ Vel or Vela OB2. Some Li-rich stars may be discarded as distance outliers by this cut, but they would otherwise be discarded in Section 5.2.1.

In Fig. 5.2 *top* we define a box in parallax and RV space around the population A (red) members, within which we select new sources as population A candidates. The edges are defined by $15.69 < $ RV / kms$^{-1} < 17.69$, which are the values 3σ from the median RV of sources in population A, and $2.6 < \varpi < 3.2$ mas. We also require that for a source to be a member of population A it must lie within the circle in proper motion space illustrated in Fig. 5.2 *bottom*, of radius 0.6 mas yr^{-1} centred on $(\mu_\alpha, \mu_\delta) = $ (-6.532, 9.753) mas yr^{-1}. This selection circle was chosen as it includes the majority (49/62) of population A members identified by Jeffries et al. (2014). Any other Li-rich target that is not located in both the parallax and RV box, and the proper motion circle is assigned to population B. Some red points in Fig. 5.2 *bottom* are significant outliers from this selection area and are likely population B members misidentified by Jeffries et al. (2014), but some lie only just outside the selection area and are not significantly different from sources that will be identified as belonging to population A. Sources must therefore be selected in both RV-parallax and proper motion criteria in order to be identified as belonging to population A. Uncertainties were not taken into account to judge if sources are inside or outside selection boxes. This will lead to some uncertainty in the exact membership, but this effect is likely to be small.

We favour more selective criteria for assigning sources to population A since we seek to find a clean sample of population A members rather than a complete sample.

5.1.5 The final sample of population members

After this selection process we find 57 (26.4%) sources consistent with being members of population A and 159 members of population B, in contrast to the results of Jeffries et al. (2014) who allocate 73 (52.5%) sources to population A and 66 to population B. We end up with fewer sources in population A than Jeffries et al. (2014) due to imposing tighter restrictions on the membership of sources in Population A from proper motion, and because not all of their original members are included in our final sample due to our Gaia DR2 astrometry cuts. In our final populations, 18 of the 159 population B members are GES sources that were allocated to population A by Jeffries et al. (2014), 40 of our population A members are Jeffries et al. (2014) population A members, 53 of our population B members are Jeffries et al. (2014) population B members. The other 105 sources are new additions, 17 for population A and 88 for population B.

5.2 Results

Figure 5.3 shows the positions of sources allocated to populations A (red) and B (blue). Figure 5.4 shows histograms of the proper motions, RV and parallaxes of our final samples, with 3σ outliers from the sample median removed, with population A members in red and population B members in blue. The clustered population A stands out as the peak at RV $\approx$ 17 mas yr^{-1} and $\mu_\delta \approx 9.8$ mas yr^{-1}, but the distinction is not clear in μ_α or parallax where the two populations largely overlap.

Seven sources allocated to population A that lie outside the GES field are apparent in Fig. 5.3, though, due to the overlap of the two populations seen in Fig. 5.4, these may in fact be population B members. Otherwise, the majority of population A members are located within the original GES field, confirming the suggestion
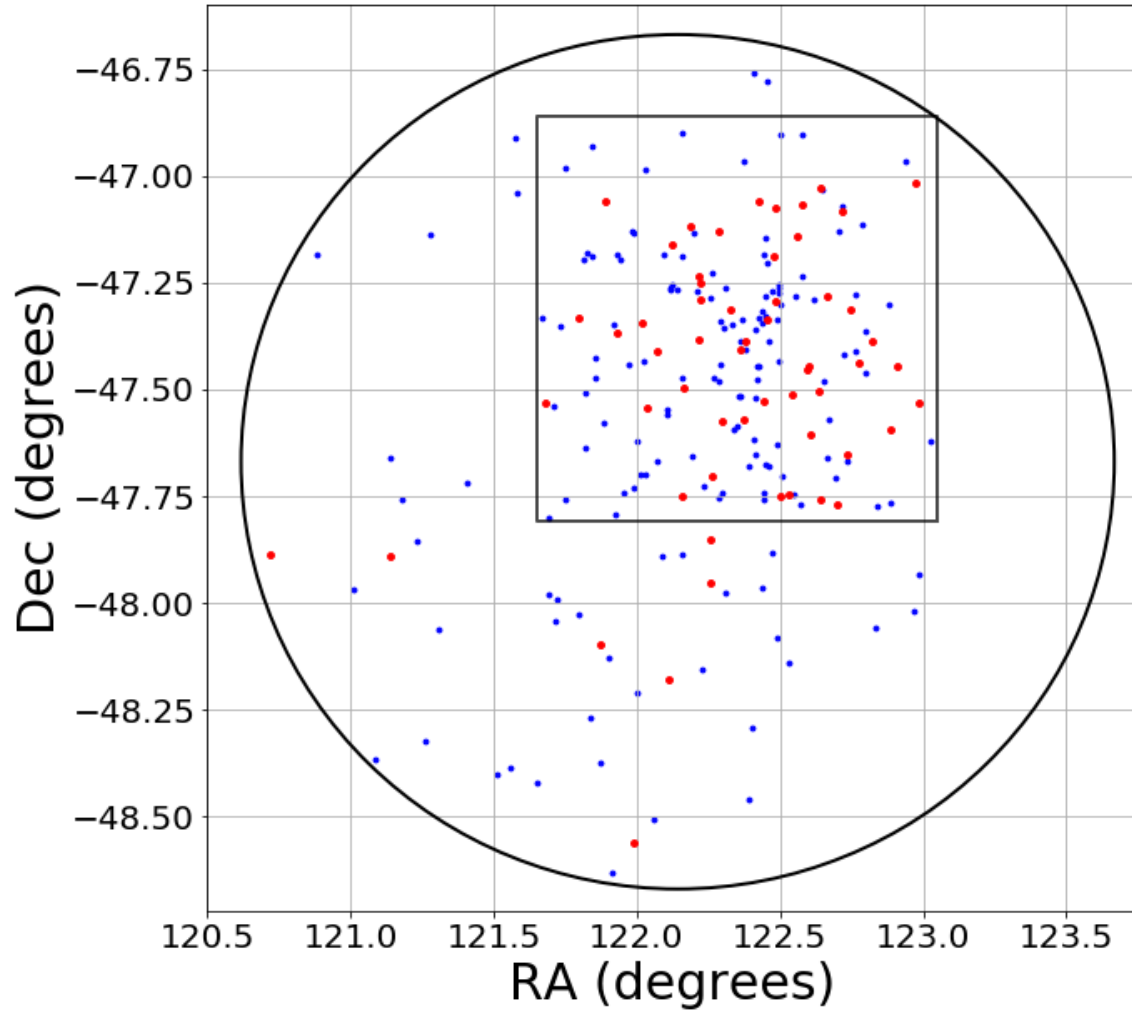
Figure 5.3: Positions of 57 population A (red) and 159 population B (blue) members from our final sample. The majority of population A members lie within the 0.9 degree square area observed by GES (Jeffries et al. 2014) but we also identify 7 new population A members further south.
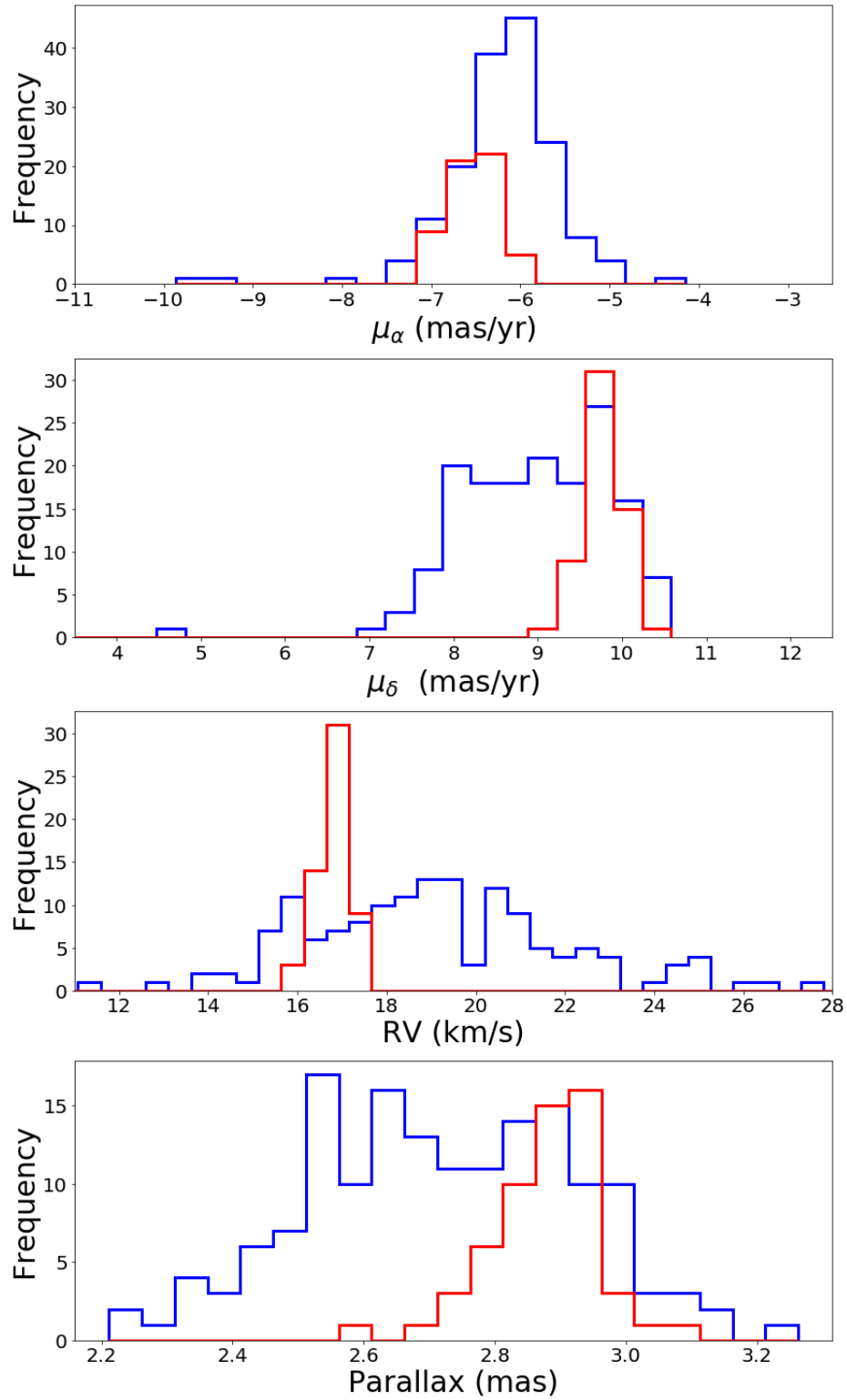
Figure 5.4: Histograms of the proper motion, radial velocity and parallax data for sources from our sample with EW(Li) > 150 mÅ without 3σ outliers in any dimension which belong to populations A (red) and B (blue).

made by Jeffries et al. (2014) that this is a much more compact population than the widely spread population B.

5.2.1 Searching for expansion in the two populations

Now that we have successfully separated our sample into a clean population A group and a widespread population B group we can look for trends between the positions and velocities of sources in each group in order to detect the signatures of group expansion, contraction and rotation. This will be easier to accomplish if we transform our kinematic data into a Cartesian coordinate system, so that we can analyse the data in three independent dimensions. We can calculate positions X,Y,Z and velocities U,V,W in the Galactic Cartesian coordinate system, from Gaia DR2 positions, parallaxes, proper motions and our RVs, using a Bayesian inference method.

We forward model the observed kinematic data from model Cartesian kinematic data using the coordinate transformation matrices from Johnson & Soderblom (1987). To sample the posterior distribution function we use the MCMC sampler *emcee* (Foreman-Mackey et al. 2013). For each star we perform 1000 iterations with 100 walkers in an unconstrained parameter space with flat and wide priors (distance priors of 0 - 10 kpc and UVW velocity priors of -200 - 200 kms^{-1}). We discard the first half of our iterations as a burn in and from the second half we report the medians of the posterior distribution function as the best fit and use the 16th and 84th percentiles as the 1 σ uncertainties (similar to the method used in Wright & Mamajek 2018).

This method is preferable to calculating X,Y,Z,U,V,W from the measured quantities since measurement uncertainties are correlated and distance uncertainties, if derived from parallaxes, do not follow a Gaussian distribution (Bailer-Jones 2015). Also, measurement uncertainties of different quantities may be correlated.

We then compare each dimension of position versus each dimension of velocity for each of the two populations, discarding 3σ outliers from the mean position or velocity in each group. Positive or negative correlations between positions and velocities of the same dimension in a group indicate either expansion or contraction of the group, while correlations between positions and velocities of different dimensions indicate components of rotation. Fig. 5.5 shows plots of position versus velocity in the same dimension for all three dimensions of each population. We also calculate lines of best fit for each using MCMC. We model the gradient and intersect of the linear fit and the fractional amount by which the uncertainties are underestimated (m, b, f). We assume that errors follow a Gaussian distribution and are independent, and use linear least squares for maximum likelihood estimation. The likelihood function is given as

$$lnp(y|x, \sigma, m, b, f) = -\frac{1}{2} \sum_n [\frac{(y_n - mx_n - b)^2}{s_n^2} + ln(2\pi s_n^2)] \qquad (5.1)$$

where

$$s_n^2 = \sigma_n^2 + f^2(mx_n + b)^2 \qquad (5.2)$$

and where σ_n are velocity uncertainties for n data points (Hogg, Bovy & Lang 2010). Uncertainties in position are accounted for by varying the measured position according to it's uncertainties. This is repeated for 2000 iterations with 200 walkers, half of which are discarded as burn in, the second half from which medians and 16th and 84th percentiles are reported from the posterior distribution function as the linear best fit gradient and uncertainties. The gradients of best-fit lines in these plots indicate the rates of expansion (negative for contraction) with the units $kms^{-1}pc^{-1}$. The gradients and their uncertainties for each combination of position against velocity are given in Table. 5.1.

For X versus U, Y versus V and Z versus W, positive or negative gradients are an indication of expansion or contraction of the group. We find evidence of expansion for population B of at least 4σ significance in all three directions (gradients
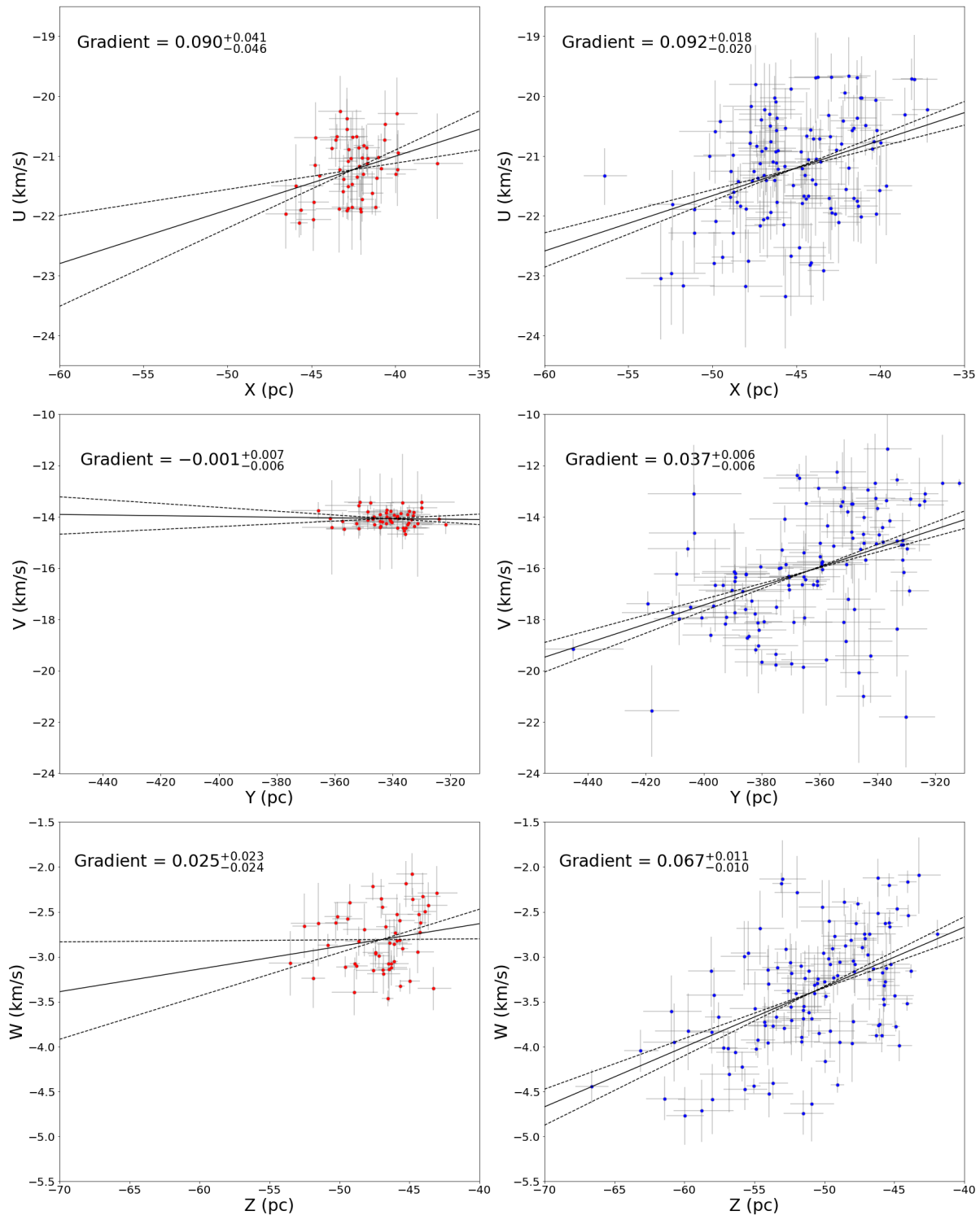
Figure 5.5: Cartesian position - velocity plots of populations A (red) and B (blue) with MCMC best fit correlation gradients and uncertainties plotted as solid and dashed lines centered on the mean values of each axis. Note that the ranges plotted in each row are different due to the different dispersions along each axis, but we kept the same range for plots along the same axes so the gradients can be compared.

Velocity	Position	Pop A Gradient $(\mathrm{kms}^{-1}/\mathrm{pc})$	Pop B Gradient $(\mathrm{kms}^{-1}/\mathrm{pc})$
U	X	$0.090^{+0.041}_{-0.046}$	$0.092^{+0.018}_{-0.020}$
V	X	$-0.040^{+0.027}_{-0.023}$	$0.267^{+0.047}_{-0.040}$
W	X	$0.036^{+0.029}_{-0.032}$	$0.080^{+0.015}_{-0.014}$
U	Y	$0.021^{+0.006}_{-0.007}$	$0.009^{+0.003}_{-0.003}$
V	Y	$-0.001^{+0.007}_{-0.006}$	$0.037^{+0.006}_{-0.006}$
W	Y	$0.003^{+0.005}_{-0.006}$	$0.011^{+0.002}_{-0.002}$
U	Z	$0.032^{+0.036}_{-0.036}$	$0.034^{+0.016}_{-0.017}$
V	Z	$0.003^{+0.024}_{-0.025}$	$0.218^{+0.037}_{-0.038}$
W	Z	$0.025^{+0.023}_{-0.024}$	$0.067^{+0.011}_{-0.010}$

Table 5.1: Gradients of MCMC linear best fit models for both A and B populations of the γ Vel cluster for every combination of Cartesian position and velocity dimensions, as well as uncertainties given by the 16% and 84% percentiles of MCMC fits.

of $0.092^{+0.018}_{-0.020}$, $0.037^{+0.006}_{-0.006}$, $0.067^{+0.010}_{-0.010}$ kms^{-1}/pc), but this expansion is significantly anisotropic, the rate of expansion in the X direction being more than twice the rate in the Y direction. Using a two-tailed z test we establish that the difference between the largest and smallest of these gradients is of at least 5σ significance. We also find some evidence of expansion for population A in the X and Z directions ($0.090^{+0.041}_{-0.046}$, $0.025^{+0.023}_{-0.024}$ kms^{-1}/pc), but this is less significant.

5.2.2 Cluster rotation

Rotation is evidenced by correlations between positions X, Y, Z and velocities U, V, W in different directions. There is some evidence for rotation in population A in several dimensions (see Table 5.1) but the most significant signature is found in Y vs U at 3σ significance ($0.021^{+0.006}_{-0.007}$ kms^{-1}/pc, Fig. 5.6). However, interpreting signatures of rotation is more complex than linear expansion or contraction, the same motion may have signatures in multiple dimensions depending on the orientation of the axis of rotation, so we do not draw physical conclusions from this here. Rotation in bound clusters has been observed previously but not frequently. In Hénault-Brunet et al. (2012) evidence for rotation was discovered in the cluster R136, and it was argued that clusters may form with at least $\sim$20% of their kinetic energy in rotation. It will be difficult to put a precise angular velocity to the γ Vel cluster without further data and modelling.

5.2.3 Testing for uncertainty correlation

Since our analysis is based on observed quantites with correlated uncertainties, we want to be able to quantify the contribution to our expansion and rotation trends
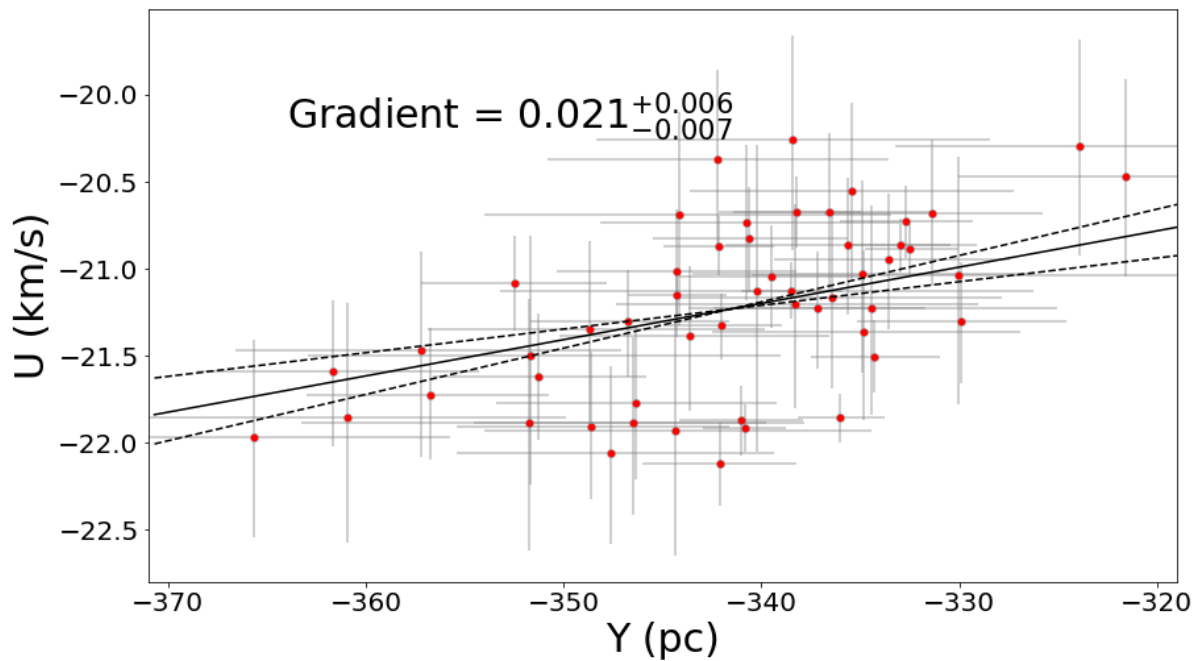
Figure 5.6: Cartesian position Y - velocity U of population A with MCMC best fit correlation gradient and uncertainty plotted as solid and dashed lines centered on the mean values of each axis. The significant (3σ) positive gradient is strong evidence of rotation in this direction.

from these correlations. We expect that estimating Cartesian values using Bayesian inference will minimise the bias caused by correlated uncertainties, but we cannot be sure that the effect is eliminated completely. In particular, due to γ Vel's position in Galactic longitude ($\sim$263°) the line-of-sight direction for our sample is very close to the Y axis, hence a source's parallax uncertainty will contribute to its uncertainty in X, Z, U and W and may create correlation between X and U values and between Z and W values which would obscure the dynamical signatures we are trying to find.

We investigated the effect of this bias on our results by simulating a population of stars without expansion with Gaussian distributions of parameters based on our sample. We generate 1000 sources with 3D Cartesian positions and velocities, apply the coordinate transformation matrices of Johnson & Soderblom (1987) to calculate observed positions and velocities and then add random errors to these values sampled from the uncertainties of our sample. We then calculate Cartesian values incorporating uncertainties and apply the MCMC linear best-fit to quantify the effect of uncertainty correlations. We found that any trends introduced by this effect are very small in comparison to the measured gradients (typically < 0.01 kms^{-1}pc^{-1}), which is too small to affect the significance of our measured expansion gradients.

5.3   Discussion

The results of the previous section strengthen the hypothesis that population A belongs to the γ Vel cluster and that population B belongs to the wider Vela OB2 association, and has interesting implications for the possible formation and evolution mechanisms of these groups.

If population B is indeed part of the wider Vela OB2 association, the expansion trends in each dimension would be expected following residual gas expulsion. Ac-

cording to some models (e.g., Baumgardt & Kroupa 2007), such expansion trends are expected to be isotropic, but the velocity gradients of this group are in fact strongly anisotropic. However, more recent studies (e.g., Kruijssen et al. 2012) suggest that residual gas expulsion may not necessarily produce isotropic expansion patterns and therefore more theoretical work exploring the predicted expansion patterns due to residual gas expulsion is needed. Numerical simulations of residual gas expulsion will be needed to determine whether this mechanism can produce the kinematic behaviour we have found.

Such strong evidence for expansion in an association is by no means commonplace. Other recent studies using Gaia astrometry have not found evidence for expansion in other associations (e.g., Wright et al. 2016; Wright & Mamajek 2018; Ward & Kruijssen 2018). Cantat-Gaudin et al. (2019a) also studied the Vela complex and identified signatures of anisotropic expansion in many of the populations present there. Unlike the previously mentioned studies, Cantat-Gaudin et al. (2019a) used the unsupervised classification scheme UPMASK to differentiate between multiple populations in their sample differing in position, proper motion and parallax. Likewise, we have used the two-component model of the γ Vel population from Jeffries et al. (2014) to separate two kinematically distinct populations in our sample. The results from these studies may indicate a need to identify and distinguish subgroups present in associations in order to detect the kinematic signatures of expansion that exist, though the distinction between different groups is not always obvious. For example, population 7 of Cantat-Gaudin et al. (2019a) contains the majority of sources in our two populations, so they fail to distinguish between the expansion of Vela OB2 and the γ Vel cluster.

However, we note that if we instead treat our sample as one group, rather than dividing it into two populations, we still find significant signatures for expansion in each dimension ($0.078^{+0.017}_{-0.017}$, $0.048^{+0.004}_{-0.005}$, $0.079^{+0.009}_{-0.009}$ kms^{-1}/pc), similar to those identified for population B (Fig. 5.7).
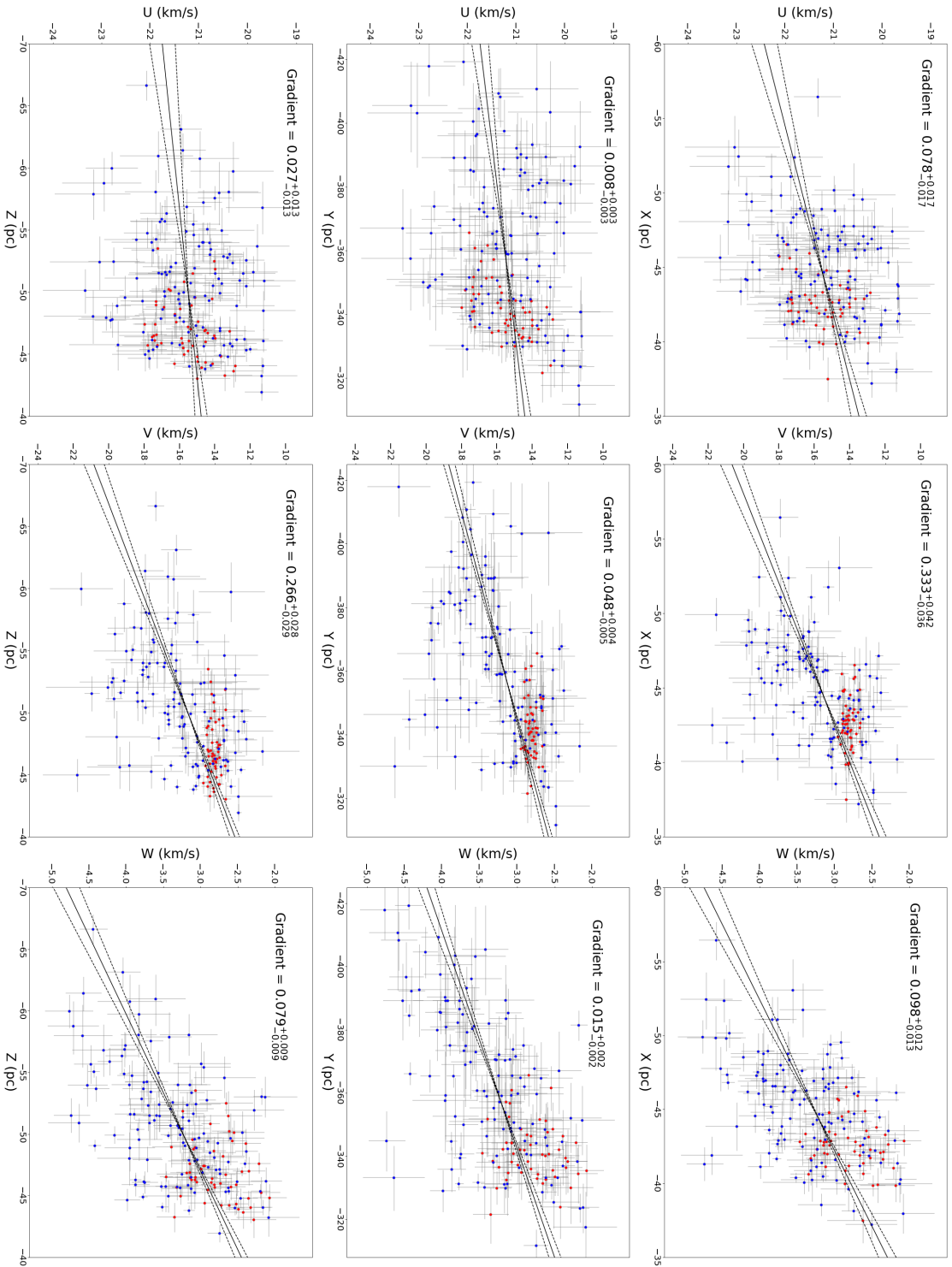
Figure 5.7: Cartesian position - velocity plots of populations A (red) and B (blue) with MCMC best fit correlation gradients and uncertainties plotted as solid and dashed lines centered on the mean values of each axis, where the two populations are treated as a single group.

6   Analysis of January 2019 data

Here we discuss the analysis of our second sample of sources in multiple fields across the Vela region. We identify the different kinematic groups present and analyse their dynamics, looking for expansion trends, candidate runaway stars and the past motion of the subgroups.

6.1   The data

In this section we explain how the sample was compiled; what data we gathered for the sources and from which surveys, our criteria for cleaning the sample and the numbers of sources included after each stage.

6.1.1   Compiling the spectroscopic, photometric and astrometric data

After reducing the spectra of our AAT sources we have 1971 unique sources with spectroscopic RVs and EW(Li)s in 8 fields across the Vela OB2 region. These sources all have 5-parameter astrometry from Gaia DR2. We calculate RUWE values for these sources (see Section 5.1.2) and 1857 sources satisfy the RUWE < 1.4 requirement (Lindegren et al. 2018b), and sources that do not meet this requirement are not included in further analysis. Though their EW(Li)s and astrometry seem to suggest that they are members of these groups of young stars, the high RUWE value indicates some problems with their Gaia DR2 astrometry, which may bias any kinematic analysis we perform on them. This is why we remove them from our sample. We then use Bayesian inference to obtain Cartesian positions and velocities (see Section

5.2.1).

In order to estimate stellar ages and masses for these sources, we cross-match our sample with the 2MASS and VISTA Hemisphere Survey (VHS) catalogues to obtain K band photometry for 1581 sources. For sources with K-band magnitudes in both catalogues we select the photometry as follows; for $K_{2MASS} < 12$ we use the 2MASS K band, for sources with $K_{VHS} > 13$ we use the VHS K band, otherwise we use the mean of both values. The 276 sources without any infrared photometry still have Gaia DR2 photometry, so we can still obtain stellar ages and masses for these. As these sources are nearby and the stellar density of the region is low, we don't expect the difference in resolution of the 2MASS and VHS surveys to introduce any significant bias.

This photometry, coupled with Gaia parallaxes, is used to estimate effective temperatures, stellar masses and stellar ages by fitting SEDs to those predicted by PMS models. The SED fitting is performed using the MCMC sampler *emcee* (Foreman-Mackey et al. 2013) and works by sampling values of initial mass and age and then using the PARSEC stellar evolution models (Marigo et al. 2017) to derive effective temperature, luminosity, and unreddened photometry. The model SED is reddened by applying a fixed extinction of $A_V = 0.131$ mag (Jeffries et al. 2014) and the Gaia DR2 parallaxes are used to place these sources at their observed distances (varying the distance according to the parallax uncertainties). The SEDs use photometry in the Gaia G, BP, RP and combined 2MASS and VHS K (see above) bands, covering a wavelength range of $\sim 0.4 - 2.2 \mu m$. The MCMC sampler iterates over different values of effective temperature and luminosity, estimating goodness of fit of the synthetic photometric profiles to the observed profiles, and outputs a posterior distribution of masses and ages. The median of the posterior distribution is taken as the best fit, and the 16th and 84th percentiles as the 1σ bounds. The stellar evolution models are valid for PMS and main-sequence stars within the mass range $350\,M_\odot$ - $0.1\,M_\odot$ and relate mass and age to effective temperature and luminosity,

while also providing model photometry. The resulting ages and masses may be biased by uncertainties due to binarity, variability, etc., which are not accounted for in these models. This may introduce a bias in the best-fit ages derived, though the relative ages of the different groups of stars will still be useful. Binarity in particular will mean that observed sources appear more luminous and redder than single stars of the same mass and age, causing their masses to be overestimated and their ages underestimated. This then creates a tail in the age distribution of sources in our sample towards younger ages, likely biasing the mean ages of our groups towards younger ages too.

6.1.2   Identifying young stars

In the investigation of the 2018 data we set the threshold for a significant EW(Li) value at $150\,\text{m\AA}$ (see Section 5.1.4), but here we decided to make the requirement $EW(Li) - \sigma_{EW(Li)} > 100\,\text{m\AA}$ as a more robust selection (see Figure 6.1). In contrast to the previous criteria, this criteria will reject sources with larger EW(Li) uncertainties but include sources with accurate EW(Li) between $100 - 150\,\text{m\AA}$ i.e. we can be more confident of the youth of a source with $EW(Li) = 130 \pm 20\,\text{m\AA}$ than a source with $EW(Li) = 151 \pm 120\,\text{m\AA}$. We have 395 sources that pass this criteria for significant EW(Li).

6.2   Overview of the sample

We plot the spatial positions of all sources with significant EW(Li) and show their proper motions relative to the mean of the whole sample as either points or vectors
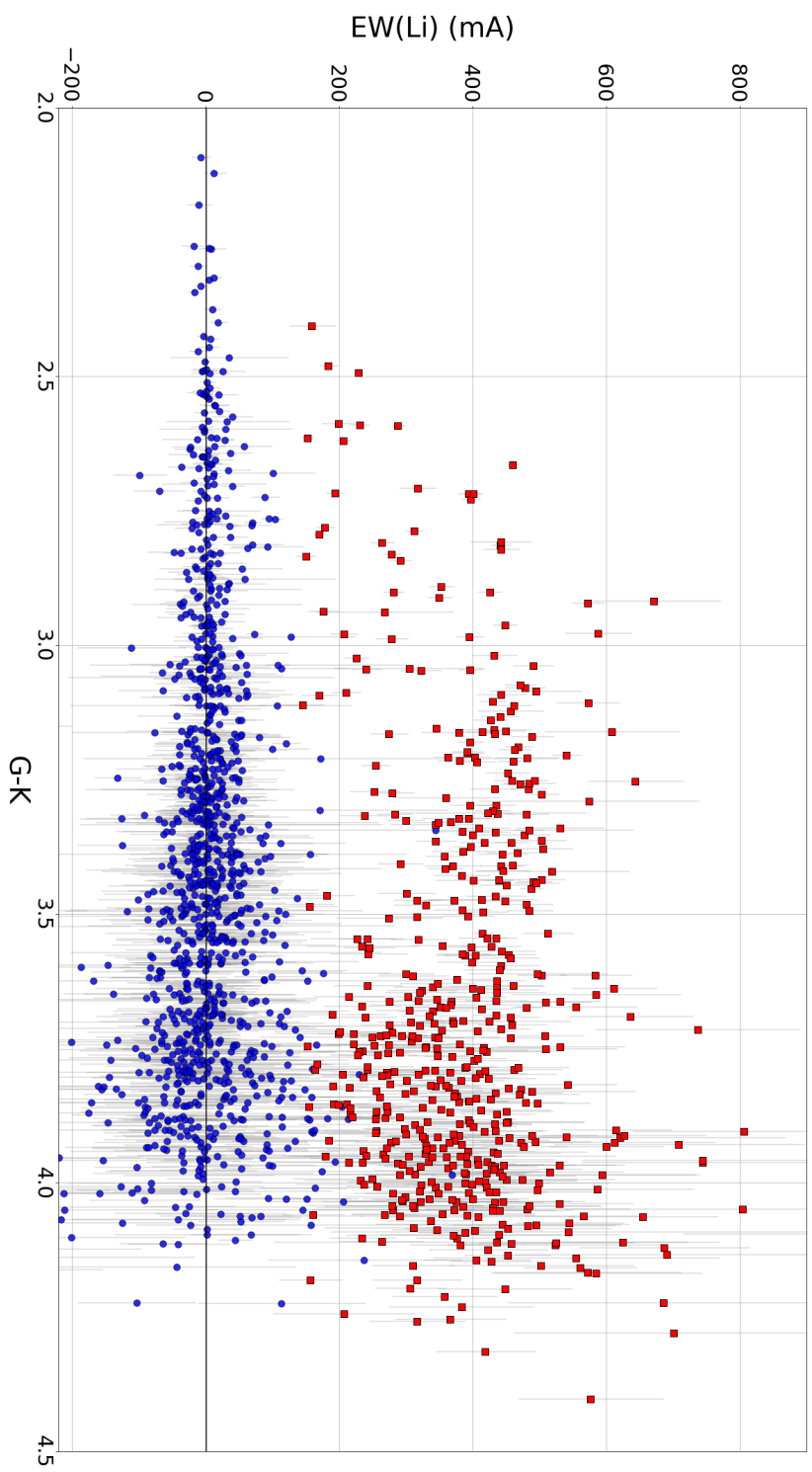
Figure 6.1: G-K (combined 2MASS and VHS) colour versus EW(Li) for sources with spectroscopic EW(Li)s. Sources that pass our threshold for significant EW(Li) are plotted in red, sources that fail are plotted in blue.

colour-coded by the position angle of their proper motions (Fig. 6.2, 6.3). Multiple subgroups are immediately apparent, in particular the dense group of purple-coloured sources at $(8^h 10^m, -47.5°)$ which corresponds to the γ Vel cluster, the sparser group of yellow-coloured sources at $(8^h 10^m, -49°)$ which correlate to the open cluster NGC 2547 and the group of cyan-coloured sources at $(7^h 50^m, -46.5°)$ which correlate to the P Puppis cluster (Caballero & Dinis 2008; and see discussion in Section 4.1.2). Other substructure is apparent, such as the sparse group of green-coloured sources in the two western-most fields and a group of green-coloured sources in the NGC 2547 field, the γ Vel field and the field east of them. There are also a number of sources across all fields with proper motions different to the nearest significant groups, some of which might possibly be runaway stars ejected from the clusters in this region.

We plot these sources in proper motion space (Fig. 6.4). Again, our sample can be divided into distinct groups. We find that the densest region of sources at $(\mu_\alpha, \mu_\delta) \sim$ (-6.5, 9.5) mas yr^{-1} correlates to the γ Vel cluster, the smaller dense group at $(\mu_\alpha, \mu_\delta) \sim$ (-4.5, 9) mas yr^{-1} correlates to the P Puppis cluster and the swathe of sources around $(\mu_\alpha, \mu_\delta) \sim$ (-6, 8) mas yr^{-1} correlates to the wider Vela OB2 association. Sources belonging to NGC 2547 are located at $(\mu_\alpha, \mu_\delta) \sim$ (-8.5, 4.5) mas yr^{-1}.

In Fig. 6.5 we plot parallax against RV for these sources. The γ Vel and P Puppis clusters are not as distinct from the Vela OB2 association in this plot, but are located at around $(\varpi = 2.85$ mas, RV $= 17$ kms$^{-1})$ and $(\varpi = 2.5$ mas, RV $= 21$ kms$^{-1})$ respectively. NGC 2547 is a distinct group at $(\varpi = 2.6$ mas, RV $= 14$ kms$^{-1})$.

We also notice the presence of a more distant population $(\varpi < 2.25)$ that is inconsistent with belonging to the Vela OB2 association or its subclusters, and so we suggest this may be another distinct group of young stars.
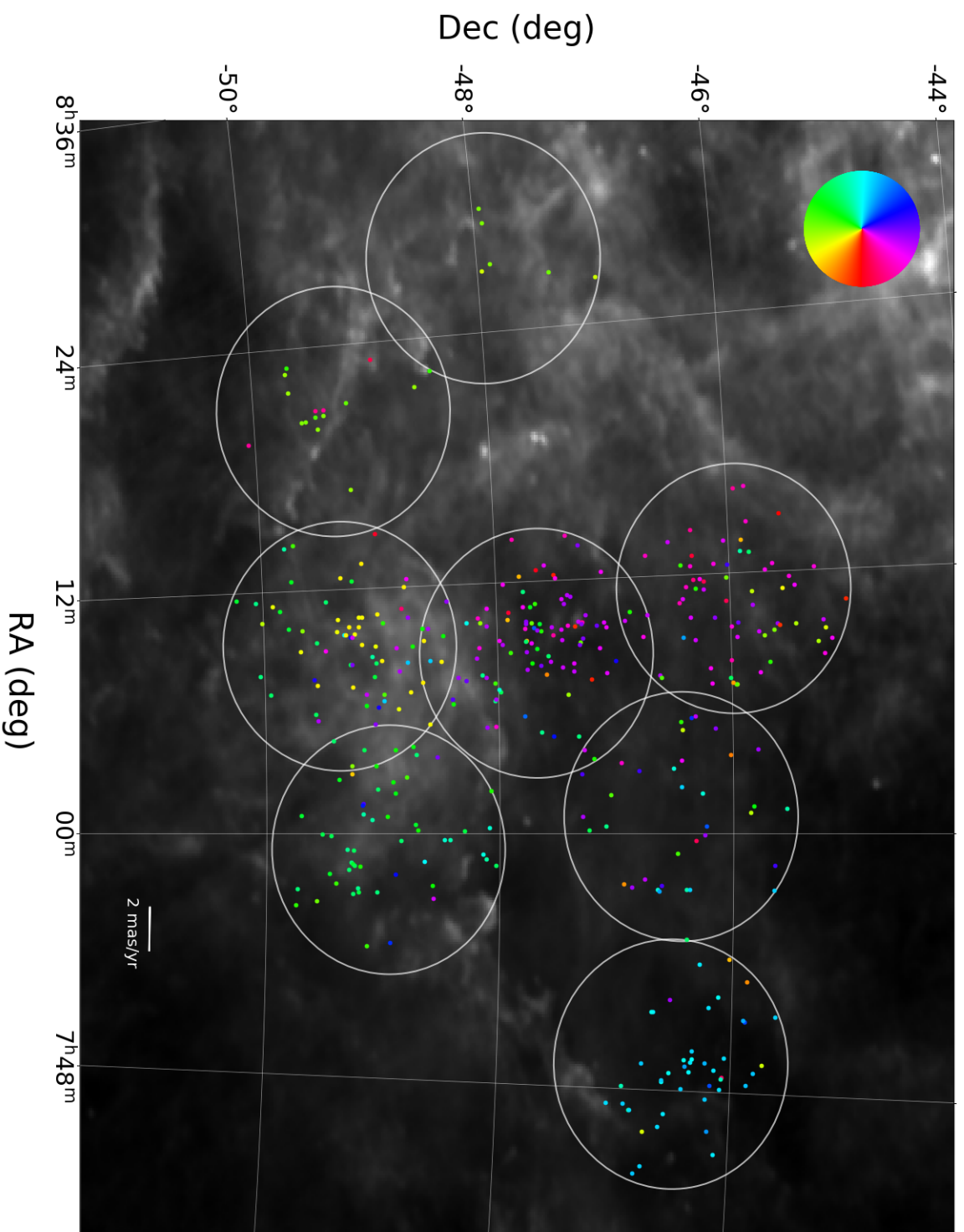
Figure 6.2: Positions of targets in 8 fields with significant EW(Li). Points are colour-coded based on the orientation of their proper motion vectors relative to the group mean. The black and white background is an IR map of the region from IRIS (Improved Reprocessing of the IRAS Survey) (Miville-Deschênes & Lagache 2005).
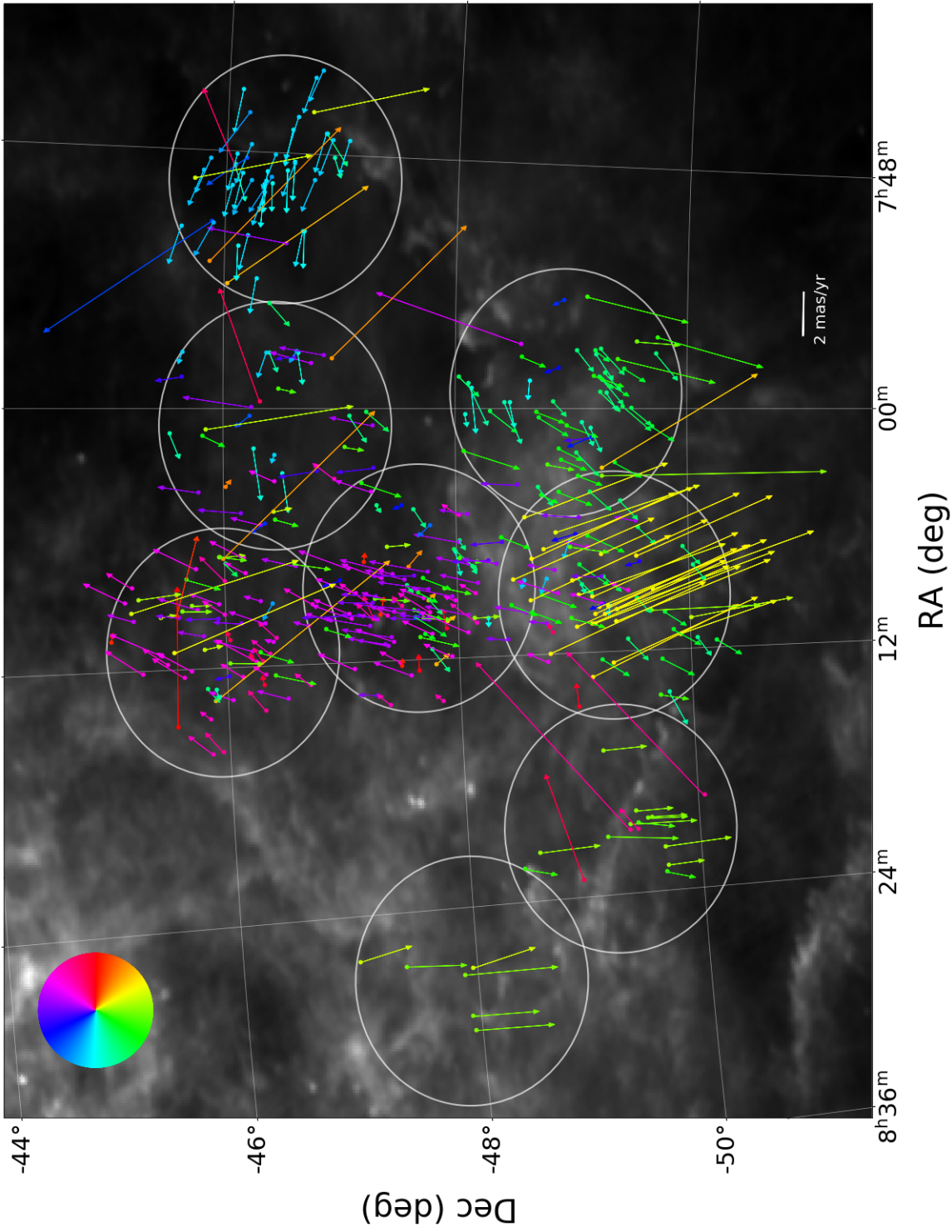
Figure 6.3: Positions of targets in 8 fields with significant EW(Li). Vectors indicate their proper motions relative to the group mean. Points are colour-coded based on the orientation of their proper motion vectors. The magnitude scale (mas/yr) of proper motion vectors is indicated by the scalebar in the bottom right. The black and white background is an IR map of the region from IRIS (Improved Reprocessing of the IRAS Survey) (Miville-Deschênes & Lagache 2005).
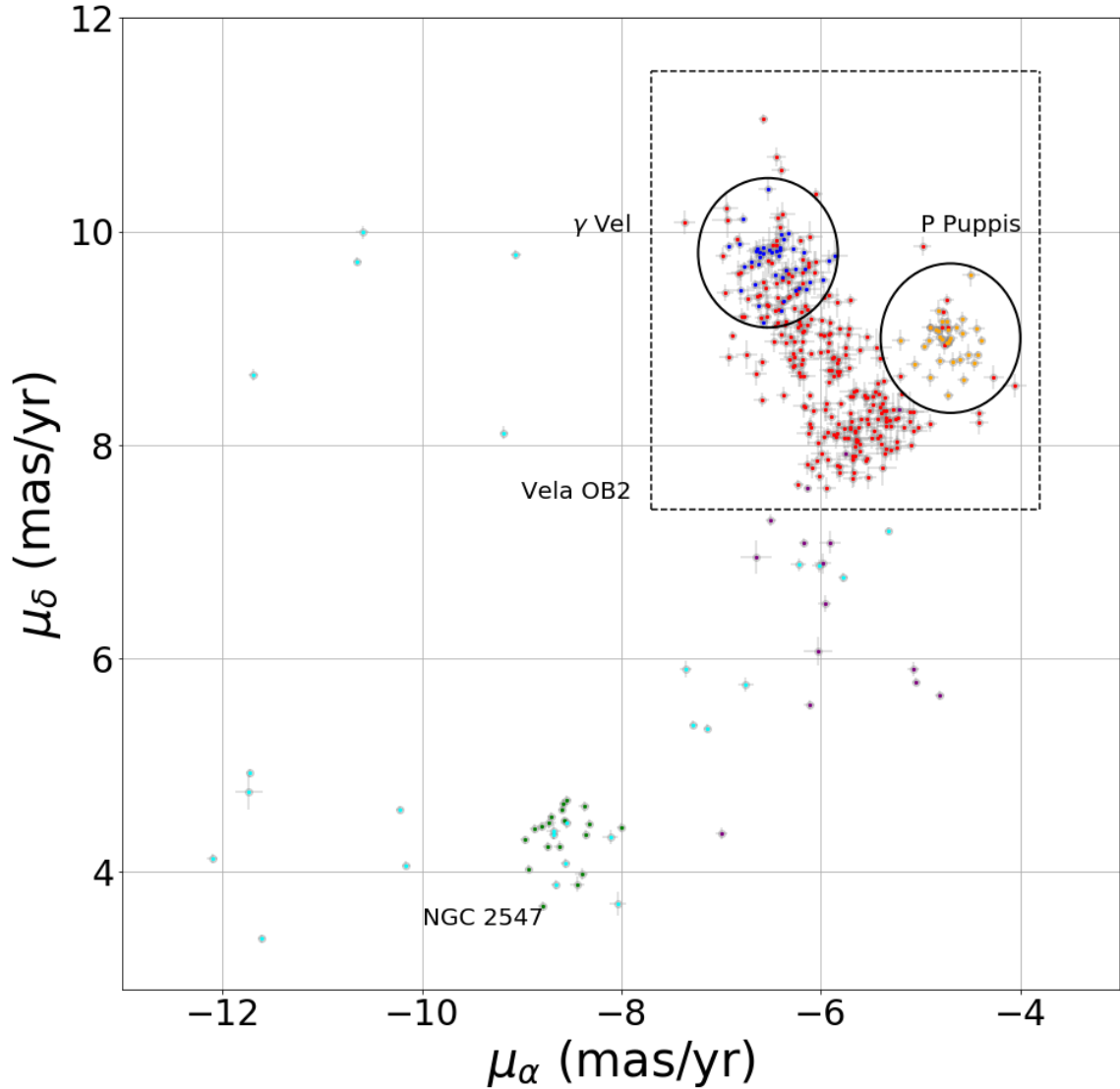
Figure 6.4: Proper motions of targets divided into our suggested groups. Coloured points are sources with significant EW(Li). Green points correlate to NGC 2547, yellow points correlate to the P Puppis cluster, blue points correlate to the γ Vel cluster (population A; Armstrong et al. 2020), red points correlate to the wider population of the Vela OB2 association (population B; Armstrong et al. 2020), purple points are sources with significant EW(Li) and distance > 440 pc, cyan points are other sources with significant EW(Li). Selection areas for the γ Vel and P Puppis clusters are shown.
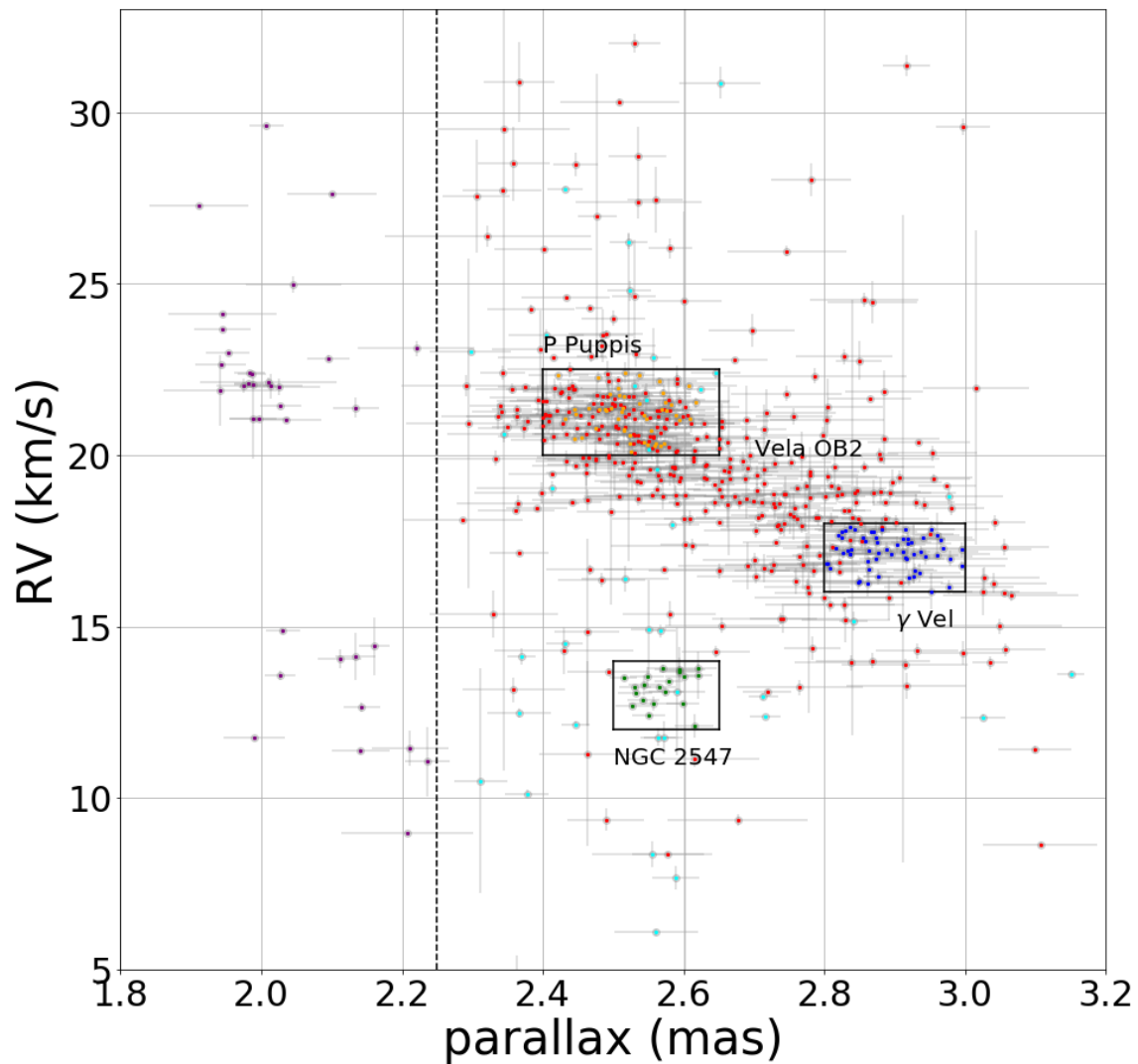
Figure 6.5: Parallax versus RV of the sources selected in Fig. 6.4 highlighting the groups identified. Colour coding is the same as Fig. 6.4. Selection areas for the γ Vel, NGC 2547 and P Puppis clusters are shown. The anti-correlation between RV and parallax for Vela OB2 sources is evidence of expansion in the association (see Section 6.3).

6.2.1 Identifying subgroups in the sample

In order to facilitate the analysis of the subgroups in our sample we need to establish criteria for sources to be allocated to different groups, in such a way so as to avoid introducing selection biases into the kinematic analysis. Firstly, we identify the regions of proper motion space occupied by the main clusters. Figure 6.4 shows sources with significant EW(Li)s (coloured). We define a selection area for the γ Vel cluster of radius 0.7 mas yr^{-1} centred at (μ_α, μ_δ) = (-6.53, 9.8) mas yr^{-1} (similar to that for population A in Section 5.1.6), an area for the P Puppis cluster of radius 0.7 mas yr^{-1} centred at (μ_α, μ_δ) = (-4.7,9) mas yr^{-1} and an area for NGC 2547 within $-9.6 < \mu_\alpha$ / mas yr^{-1} < -7.5 and $3 < \mu_\delta$ / mas yr^{-1} < 5.5. We also define boundaries for these clusters in RV and parallax (Fig. 6.5). For γ Vel we require sources to have $2.8 < \varpi/mas < 3.0$ and $16 < $ RV / kms^{-1} < 18, for P Puppis we require sources to have $2.4 < \varpi/mas < 2.65$ and $20 < $ RV / kms^{-1} < 22.5 and for NGC 2547 we require sources to have $2.5 < \varpi/mas < 2.65$ and $12 < $ RV / kms^{-1} < 14.

These boundaries for membership of the clusters are designed to be strict, at the risk of not including all possible members. We emphasise cleanness of the samples over completeness so that the analysis of their dynamics in sections 6.3 - 6.5 are as accurate as possible. As a consequence it is likely that the sample for the Vela OB2 association will then contain sources which are really members of these clusters. However, as it is by far the most populous group, a small amount of contamination will affect the results much less than possible contamination in the cluster groups.

There is a distinct group of more distant sources at $\varpi < 2.25$ which we plot in purple in Figures 6.4 and 6.5. Sources which are not allocated to the γ Vel cluster, P Puppis cluster or the distant group but are within the large overdensity in proper motion space ($-7.7 < \mu_\alpha$ / mas yr^{-1} < -3.8 and $7.4 < \mu_\delta$ / mas yr^{-1} < 11.5) are allocated to the Vela OB2 association group and are plotted in red in Figures 6.4

and 6.5. This is the largest group in our sample. Any other source with significant EW(Li) not in these five groups is plotted in cyan in Figures 6.4 and 6.5. It is these sources with kinematics unlike the main groups that we investigate to identify candidate runaway stars.

It is also worth noting that there are many sources without significant EW(Li) that are located in the overdensities associated with our selected groups. In particular, the NGC 2547 group has relatively few sources with significant EW(Li), but there are many sources without significant EW(Li) which form a dense group in this area of proper motion space. This is likely due to the age of NGC 2547 ($\sim$35 Myr, Jeffries & Oliveira 2005) being closer to the age at which YSOs of this mass range begin to deplete their Li.

6.2.2   Comparing the sample to other works

Of the 395 sources with significant EW(Li), 377 are included in Cantat-Gaudin et al. (2019a) as candidate young stars, which we can now confirm. The populations of Cantat-Gaudin et al. (2019a) represent groups of young stars in the extended Vela-Puppis region which are distinguished by their different ages and kinematics, but together suggest a prolonged period of connected star formation events from a turbulent molecular cloud.

In Table 6.1 we give the numbers of these sources allocated to each of our groups and the populations of Cantat-Gaudin et al. (2019a) that they match with. Notably, all sources in the γ Vel and P Puppis clusters and all but one in the Vela OB2 association match to population 7 of Cantat-Gaudin et al. (2019a), the youngest population of theirs (10-15 Myr) known to contain the main part of Vela OB2. Also, all our sources for NGC 2547 match to their population 4, an older population (35-40 Myr) known to contain NGC 2547 as well as several other open clusters.

Sources in our 'distant' group are shared between several populations of Cantat-Gaudin et al. (2019a). Most belong to their population 6, a young population associated with the cluster BH 23, but most of which is located outside our area of observation, and 3 sources belong to population 3 of Cantat-Gaudin et al. (2019a), a population not associated with any known clusters. Among our possible runaway sources, the majority belong to population 4, the same population as NGC 2547, but 5 sources belong to population 3, an older ($\sim$ 30 -40 Myr) population also not associated with any known clusters. The identities of these populations without clusters are unclear and so in turn are the identities of our distant and runaway groups.

Overall, the membership of sources in the Vela OB2 association and the three clusters agrees very well with the populations of Cantat-Gaudin et al. (2019a), and it is our groups that are not identified with a specific cluster or association that have a mix of sources from populations other than those of Vela OB2 or NGC 2547. In order to thoroughly investigate the membership of these sources, a larger spectroscopic survey would be required across the whole region studied by Cantat-Gaudin et al. (2019a), to confirm the ages of these populations and to break them up into more detailed substructure, as we have done with Vela OB2.

6.2.3   Ages of the subgroups

In Fig 6.6 we plot histograms of sources' SED ages in each group, with arrows indicating the position of the group weighted mean age. The weighted mean values are 10.5 Myr for the Vela OB2 group, 27.2 Myr for NGC 2547, 9.8 Myr for P Puppis, 14.5 Myr for γ Vel and 17.1 Myr for the distant population.

These ages are in good agreement with literature ages for groups that have been studied previously. Jeffries & Oliveira (2005) report an LDB (Li depletion boundary) age of $\sim$ 35 Myr for NGC 2547, which is in good agreement with other values in open cluster catalogues (e.g. 50 $\pm$20 Myr Netopil et al. 2016) and the
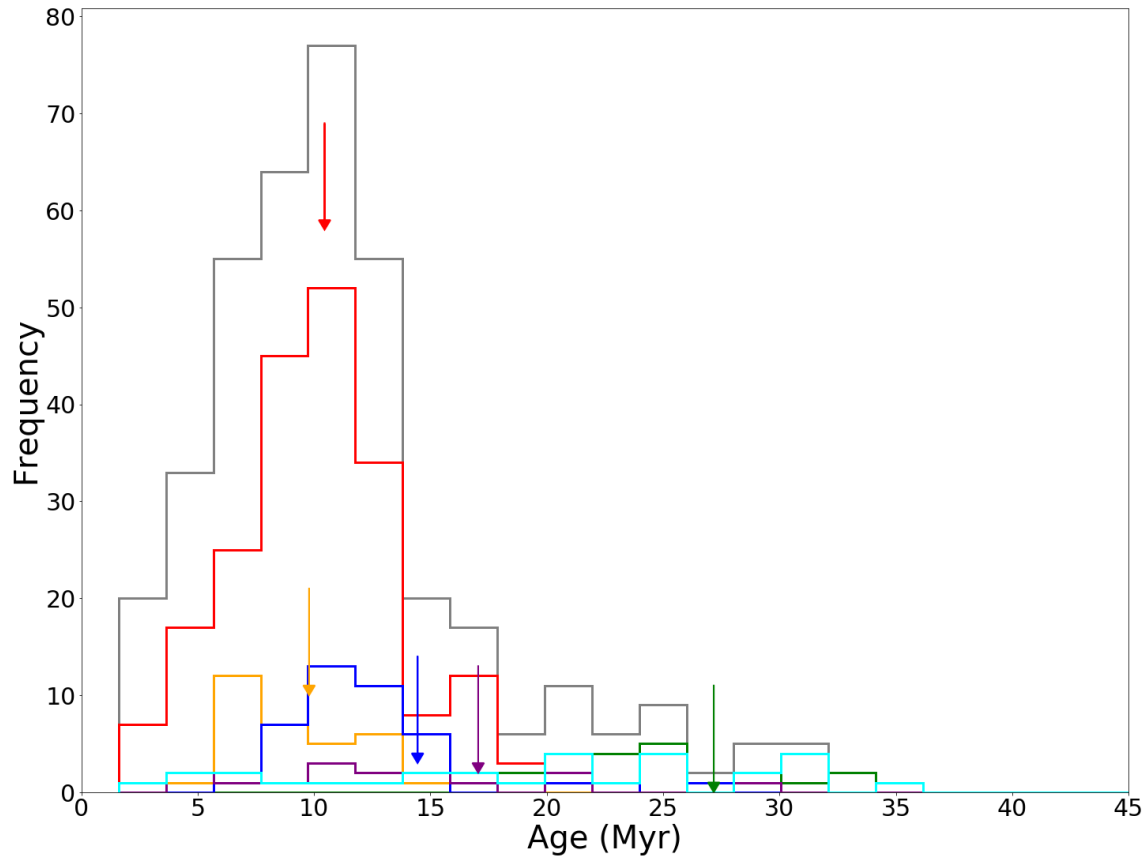
Figure 6.6: Histogram showing the numbers of sources per bin of SED ages (Myr). Histogram colours indicate the populations of sources using the same colour-coding as Fig 6.4, with the grey histogram indicating the total per bin. Weighted mean ages for each group are indicated by coloured arrows. The weighted mean ages are 12.1 Myr for the Vela OB2 group (red), 31.1 Myr for NGC 2547 (green), 9.9 Myr for P Puppis (yellow), 15.4 Myr for γ Vel and 15.8 Myr for the distant population (purple).

CG population	Vela OB2	γ Vel	NGC 2547	P Puppis	Distant	Runaways
3	0	0	0	0	0	5
4	0	0	19	0	0	13
5	0	0	0	0	3	0
6	1	0	0	0	7	0
7	244	42	0	32	1	1

Table 6.1: Numbers of sources in our identified groups that match with populations from Cantat-Gaudin et al. (2019a).

recent kinematic study of the region by Cantat-Gaudin et al. (2019a) ($\sim$37 Myr, population 4). For γ Vel Jeffries et al. (2017) report an age of 18-21 Myr (LDB and CMD estimates in agreement) while Cantat-Gaudin et al. (2019a) give an age of $\sim$ 9-14 Myr for the population containing both γ Vel and Vela OB2. Vela OB2 has not had a specific age estimation since Sahu (1992) (20 Myr), though Jeffries et al. (2014) conclude that their population A (γ Vel) is 1-2 Myr older than population B (Vela OB2) based on Li depletion, which suggests an age of 16-20 Myr for the association.

If we take $\sim$ 35, 18-21 and 16-20 Myr as the literature ages for NGC 2547, γ Vel and Vela OB2, our SED ages are in good agreement but are systematically slightly lower. Raising our SED ages by 25 - 30% allows us to match our γ Vel SED age with the literature age, a scaling-up that is necessary because isochronal ages have recently been found to be too young due to radius inflation (Jeffries et al. 2017). This scaling then allows us to calculate ages for the P Puppis cluster (12.5 Myr) and the distant population (20 Myr) that are on the same scale as the literature ages

for these groups. We do not report uncertainties on these SED ages since there are many factors which could contribute bias which are not modelled (Section 6.1.1).

Notably, while γ Vel and Vela OB2 have similar ages, the P Puppis cluster is distinctly younger, indicating a timescale of star formation in this region spanning up to $\sim$10 Myr. Without clear indication of a smooth age gradient, however, it is unclear whether this star formation was a continual or episodic process. Searching for an age gradient in the original spatial distribution of sources is a possible area of future work though.

Fig. 6.7 shows a histogram of the ages of sources in the kinematically distinct group compared to the sources belonging to NGC 2547. It is clear that a large proportion of these kinematically distinct sources are of a similar age to NGC 2547, as well as having similar proper motions (Fig 6.4) and belonging to population 4 of Cantat-Gaudin et al. (2019a) (Section 6.2.2). However, we do not include them in NGC 2547 due to their different parallaxes and RVs (Fig 6.5). We revisit these sources in Section 6.5 to consider whether they may be possible runaways from some of the clusters in the region.

6.3   Expansion trends of subgroups

Our first goal is to search for evidence of expansion or contraction in the identified groups in order to ascertain their dynamical state. We use the same MCMC forward modelling approach with coordinate transformation matrices from Johnson & Soderblom (1987) to calculate Galactic Cartesian positions X, Y, Z and velocities U, V, W, as explained in Section 5.2.1. We then use an MCMC approach to calculate lines of best fit to the various position - velocity combinations (section 5.2.1) in order to find evidence of expansion, contraction or rotation. In each case, we removed
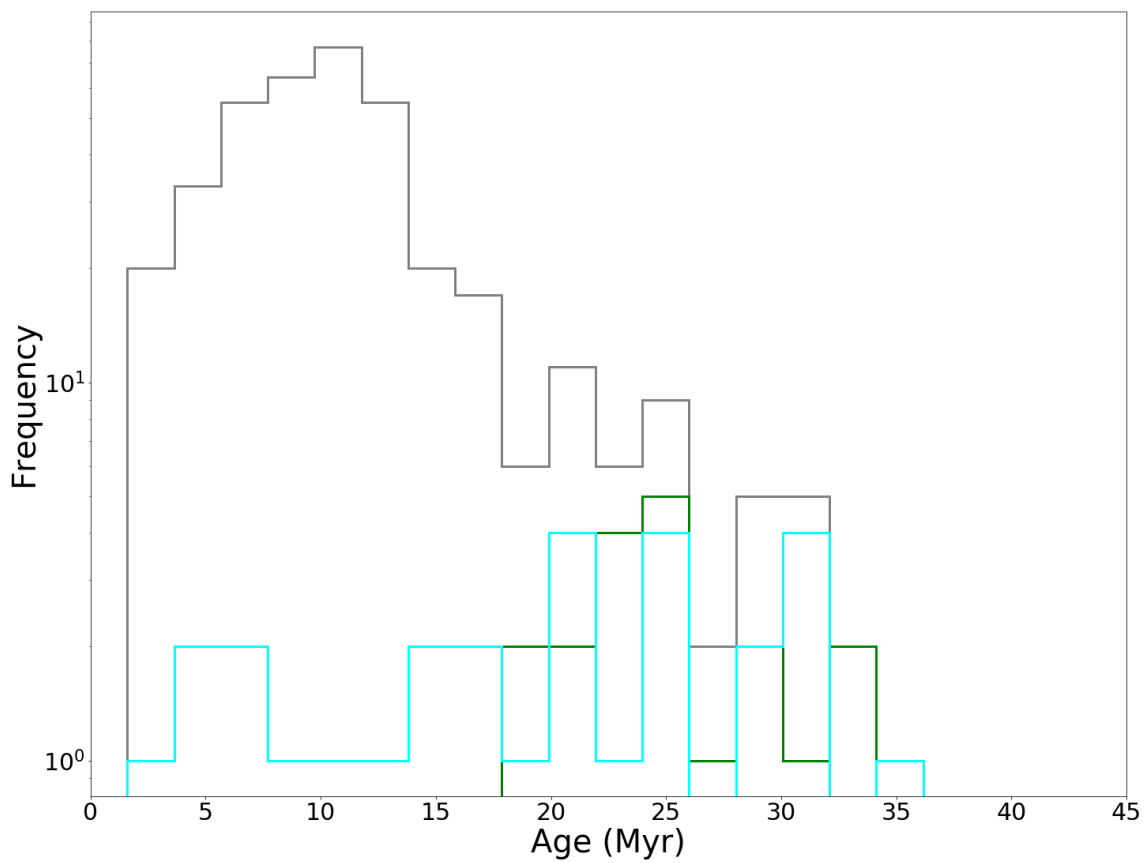
Figure 6.7: Histogram showing the numbers of sources per bin (in logarithmic scale) of SED ages (Myr) of the NGC 2547 sources (green), the sources distinct from the main kinematic groups (cyan) and the grey histogram indicating all sources (same as Fig 6.6).

Group	Velocity	Position	Gradient ($\mathrm{kms^{-1}/pc}$)	Significance
Vela OB2	U	X	$0.078^{+0.005}_{-0.005}$	15σ
	V	Y	$0.044^{+0.004}_{-0.005}$	9σ
	W	Z	$0.052^{+0.004}_{-0.004}$	12σ
P Puppis	U	X	$0.136^{+0.031}_{-0.029}$	4σ
	V	Y	$-0.015^{+0.017}_{-0.017}$	-
	W	Z	$0.058^{+0.012}_{-0.012}$	4σ
γ Vel	U	X	$0.041^{+0.017}_{-0.018}$	2σ
	V	Y	$0.015^{+0.017}_{-0.017}$	0σ
	W	Z	$0.032^{+0.012}_{-0.012}$	2σ

Table 6.2: Expansion gradients of MCMC linear best fit models for the sample populations of the Vela OB2 association, NGC 2547, P Puppis and γ Vel clusters for combinations of cartesian position and velocity dimensions, as well as uncertainties given by the 16% and 84% percentiles of MCMC fits.

sources that differ in position or velocity by $> 3\sigma$ from the mean of their identified group. Figures 6.8 - 6.11 show diagrams of co-directional Cartesian positions X, Y, Z versus velocities U, V, W for each of the Vela OB2, NGC 2547, P Puppis and γ Vel groups. Tables 6.2 and 6.3 contain the gradients and uncertainties for the MCMC linear best-fits.

We find strong evidence for expansion in the Vela OB2 group (Fig. 6.8) as evidenced by the significant positive gradients of the MCMC linear best-fits. These are of $> 9\sigma$ significance in all directions ($0.078^{+0.005}_{-0.005}$, $0.044^{+0.004}_{-0.005}$, $0.052^{+0.004}_{-0.004}$), but is notably greater in the X direction, similar to the anisotropic trends found for population B (Vela OB2) in Section 5.2.1 (Fig 5.3). The expansion gradients we find here for X vs U and Z vs W are not as steep as those in Fig. 5.5 for population B
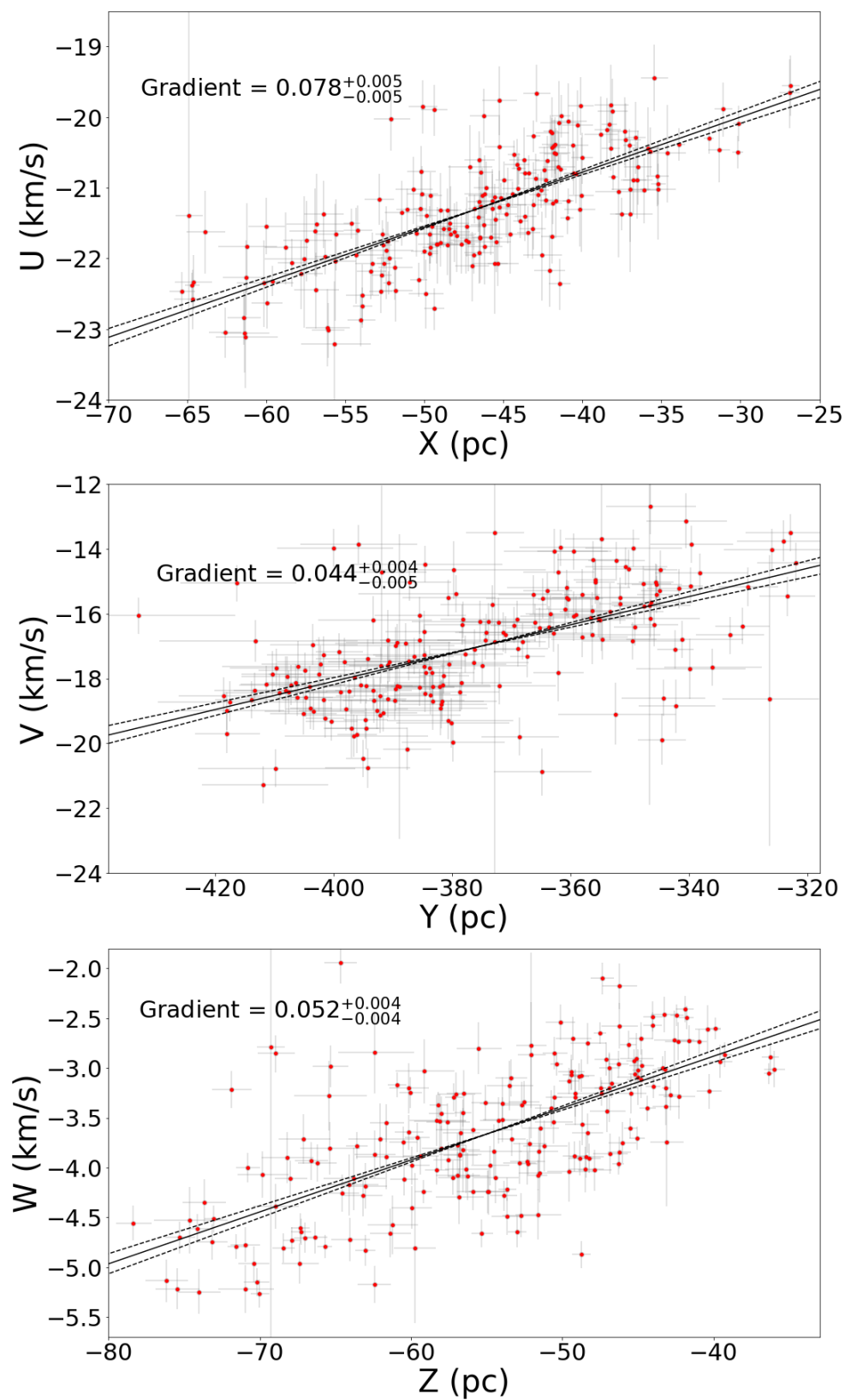
Figure 6.8: X vs U, Y vs V and Z vs W for sources in the Vela OB2 association population (red) with uncertainties. The MCMC linear best fit and 16th and 84th percentiles are shown as solid and dashed lines respectively.
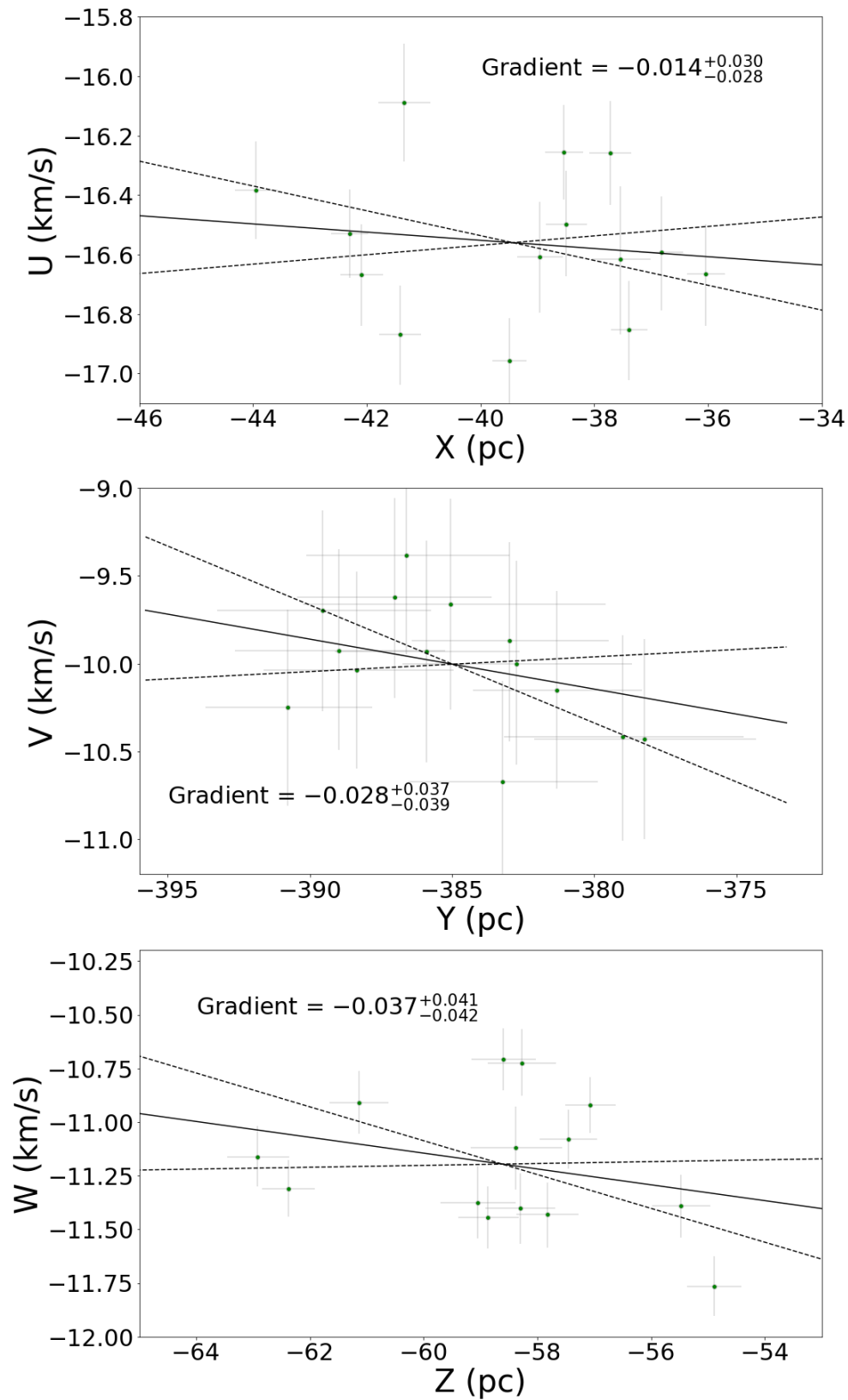
Figure 6.9: X vs U, Y vs V and Z vs W for sources in the NGC 2547 cluster population (green) with uncertainties. The MCMC linear best fit and 16th and 84th percentiles are shown as solid and dashed lines respectively.
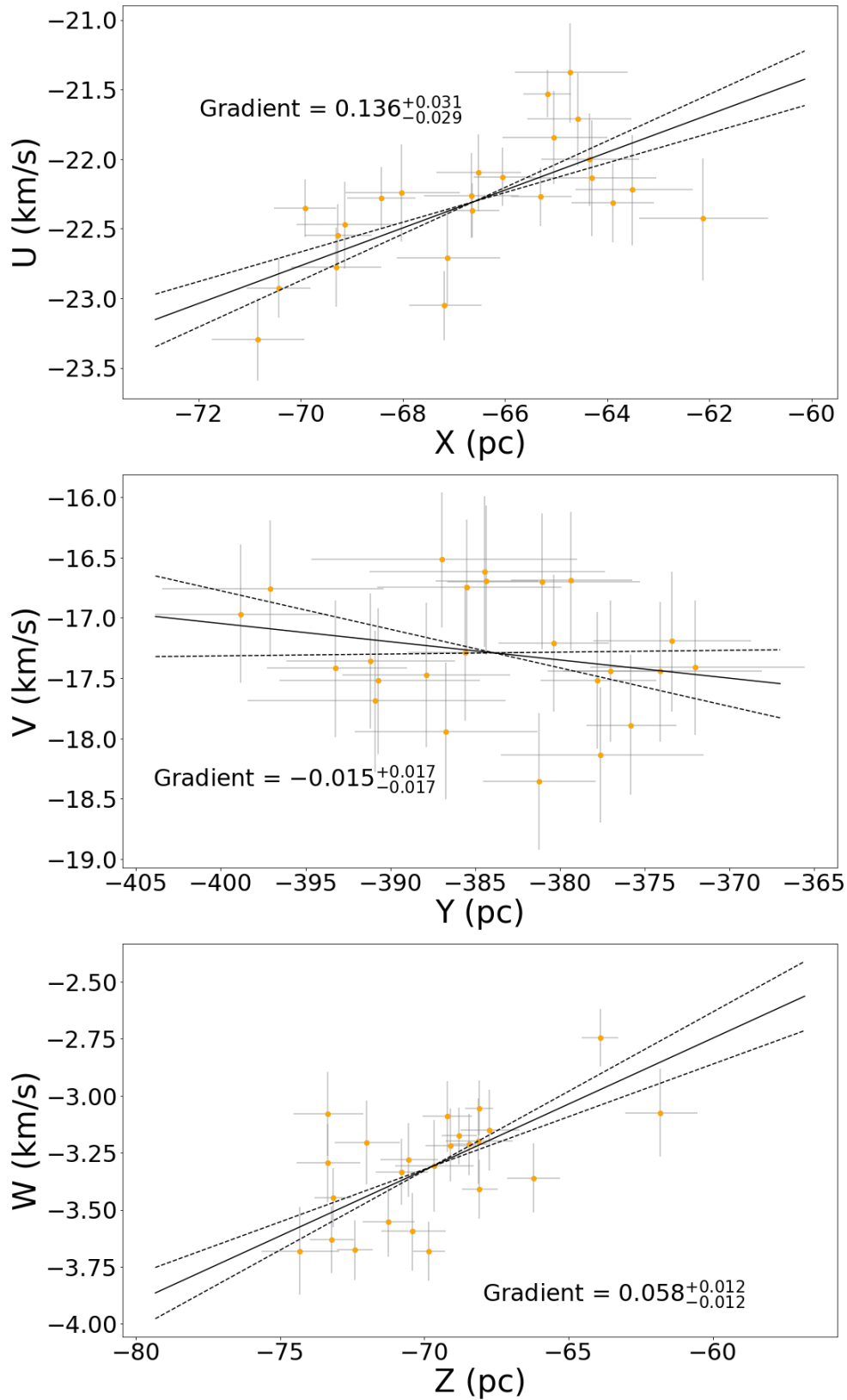
Figure 6.10: X vs U, Y vs V and Z vs W for sources in the P Puppis cluster population (yellow) with uncertainties. The MCMC linear best fit and 16th and 84th percentiles are shown as solid and dashed lines respectively.
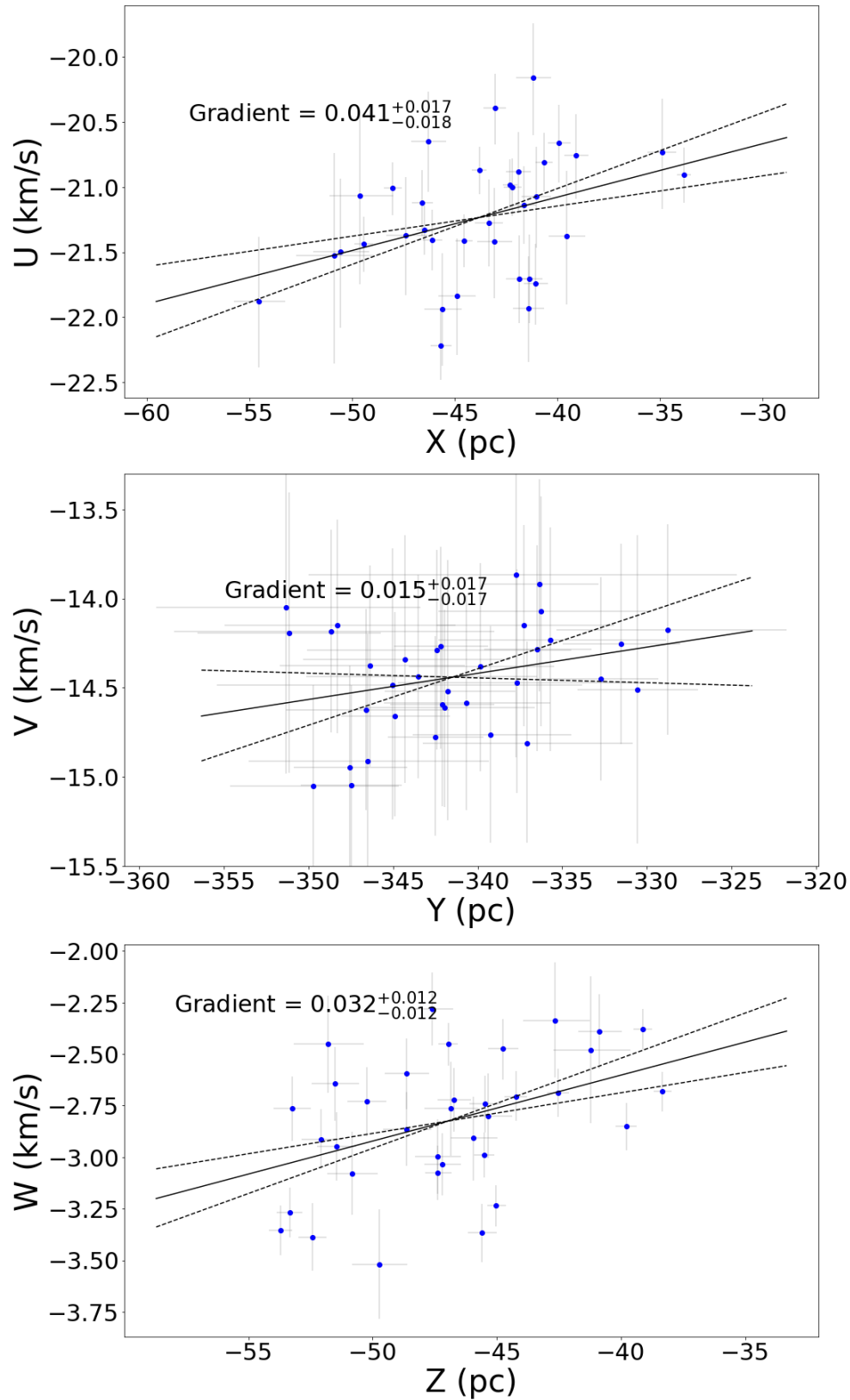
Figure 6.11: X vs U, Y vs V and Z vs W for sources in the γ Vel cluster population (blue) with uncertainties. The MCMC linear best fit and 16th and 84th percentiles are shown as solid and dashed lines respectively.

(0.078 and 0.052 respectively, rather than 0.098 and 0.069). The difference is most likely because our new sample contains many more members spread over a wider area, but the significance of the gradients have increased dramatically, from 4σ in X vs U to $> 15\sigma$.

We do not find significant expansion trends for NGC 2547 (Fig. 6.9), due to the small size of our sample for this cluster. The trends we find for the P Puppis (Fig. 6.10) and γ Vel (Fig. 6.11) clusters are quite similar. For both groups there is evidence for expansion in the X vs U direction, of 2σ significance for γ Vel and $> 4\sigma$ significance for P Puppis ($0.041^{+0.017}_{-0.018}$ and $0.136^{+0.031}_{-0.029}$ respectively).

There is also some evidence for expansion in the Z direction, of 2σ significance for γ Vel and 4σ significance for P Puppis ($0.032^{+0.012}_{-0.012}$, $0.058^{+0.012}_{-0.012}$), though it appears that this trend in the P Puppis cluster may be due a few outlying sources. There is little evidence for expansion (or contraction) in the Y direction for either group.

The evidence for expansion is expected in Fig. 6.8 since Vela OB2 is a sparse, unbound association. But the expansion seen in Fig. 6.10 and 6.11 is not, since P Puppis and γ Vel are compact clusters, and therefore expected to be gravitationally bound. In Fig. 5.3 expansion in X vs U and Z vs W was suggested by the gradients for population A, but they were not significant enough to be confident of. Figure 6.11 confirms this expansion.

It is also possible that these samples are contaminated, so that the expansion trends are due to sources that really belong to Vela OB2 and so the association's expansion is imprinted on these groups. Fig. 6.12 *left* shows the distribution of γ Vel sources (blue) in X vs U compared to the distribution of Vela OB2 sources (grey) with the MCMC linear best fits for each group. The distributions of the two groups overlap, so there is the possibility that the γ Vel group is contaminated with sources that should belong to Vela OB2, and that the steep gradient in X vs U for γ Vel is the result of these contaminants. We also made sure in Section 6.2 that membership criteria for the clusters was as strict as possible to reduce contamination
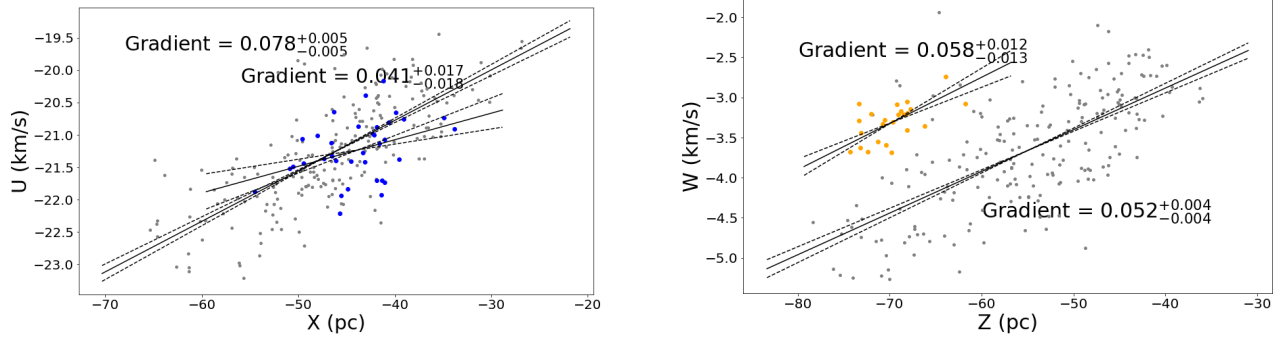
Figure 6.12: *Left* : X vs U of γ Vel sources (blue) and VelaOB2 sources (grey) with MCMC linear best fits and 16th and 84th percentiles shown as solid and dashed lines respectively. *Right* : Z vs W of P Puppis sources (yellow) and VelaOB2 sources (grey) with MCMC linear best fits and 16th and 84th percentiles shown as solid and dashed lines respectively.

to a minimum. Fig. 6.12 *right* shows the distribution of P Puppis sources (yellow) in Z vs W compared to the distribution of Vela OB2 sources (grey) with the MCMC linear best fits for each group. The two groups are clearly separated, which indicates that the P Puppis group is unlikely to be highly contaminated by Vela OB2 sources, and that the expansion gradients for this group do represent its physical state.

There are a number of scenarios that may produce such results. Firstly, the clusters may be gravitationally unbound and expanding. This would be surprising for a cluster as compact as γ Vel however, and for P Puppis the expansion is strongly anisotropic (Fig. 6.10 even suggests contraction in the Y direction). In the Galactic Cartesian coordinate system the X direction corresponds to the direction, towards and away from the Galactic center, so it is possible that the greater rates of expansion in X vs U seen in Figs. 6.8, 6.10 and 6.11 are due to tidal shearing effects, though such effects are usually observed for older open clusters. It is also possible that the P Puppis and γ Vel clusters are being pulled in a certain direction by the mass of the Vela OB2 association or its primordial molecular cloud that correlates strongly

with the X direction, somewhat with Z and hardly with Y. All of these possibilities are strongly dependent on the configuration of the association and these clusters at the time of birth and over the last 5-10 Myrs, which we explore further in Section 6.4.1.

6.3.1   Rotation

Table 6.3 shows best fit gradients between positions and velocities in different directions for the Vela OB2 association and the γ Vel and P Puppis clusters, which indicate elements of rotation. In the two clusters, most rotation trends are not very significant other than Y vs U for P Puppis at 6σ, which provides evidence that the cluster is rotating in this direction.

For the Vela OB2 association there are significant trends between W and Y of $>10\sigma$ significance (see Fig. 6.13) and between V and Z of $>6\sigma$ significance. Given that the association is gravitationally unbound, these trends more likely represent residual angular momentum in the dynamics of this system, rather than rotation. We will return to this discussion in Section 6.4.1 and where we consider the future (and past) motion of the association.

6.3.2   Estimating kinematic ages

Since the units of these expansion gradients are km s^{-1} pc^{-1} and 1 km s^{-1} = 1.023 pc Myr-1 , we can easily calculate the timescale of expansion in Myrs, allowing us to estimate the period of time they have been expanding for (assuming the rate of expansion has been constant). This is an age determination method known as 'kinematic ages' which, under the assumption that the groups were at their most compact

Group	Velocity	Position	Gradient (kms^{-1}/pc)	Significance
Vela OB2	V	X	$-0.002^{+0.012}_{-0.012}$	-
	W	X	$0.009^{+0.006}_{-0.006}$	1σ
	U	Y	$0.006^{+0.002}_{-0.003}$	2σ
	W	Y	$0.018^{+0.002}_{-0.002}$	10σ
	U	Z	$-0.012^{+0.006}_{-0.006}$	2σ
	V	Z	$0.076^{+0.012}_{-0.012}$	6σ
P Puppis	V	X	$-0.008^{+0.051}_{-0.051}$	-
	W	X	$-0.005^{+0.025}_{-0.023}$	-
	U	Y	$0.042^{+0.008}_{-0.008}$	4σ
	W	Y	$0.010^{+0.007}_{-0.008}$	1σ
	U	Z	$0.016^{+0.036}_{-0.036}$	-
	V	Z	$-0.004^{+0.044}_{-0.041}$	-
γ Vel	V	X	$-0.019^{+0.027}_{-0.025}$	-
	W	X	$-0.022^{+0.014}_{-0.013}$	1σ
	U	Y	$0.022^{+0.014}_{-0.014}$	1σ
	W	Y	$0.004^{+0.009}_{-0.010}$	-
	U	Z	$-0.012^{+0.019}_{-0.019}$	-
	V	Z	$0.013^{+0.025}_{-0.025}$	-

Table 6.3: Rotation gradients of MCMC linear best fit models for the sample populations of the Vela OB2 association, NGC 2547, P Puppis and γ Vel clusters for combinations of cartesian position and velocity dimensions, as well as uncertainties given by the 16% and 84% percentiles of MCMC fits.
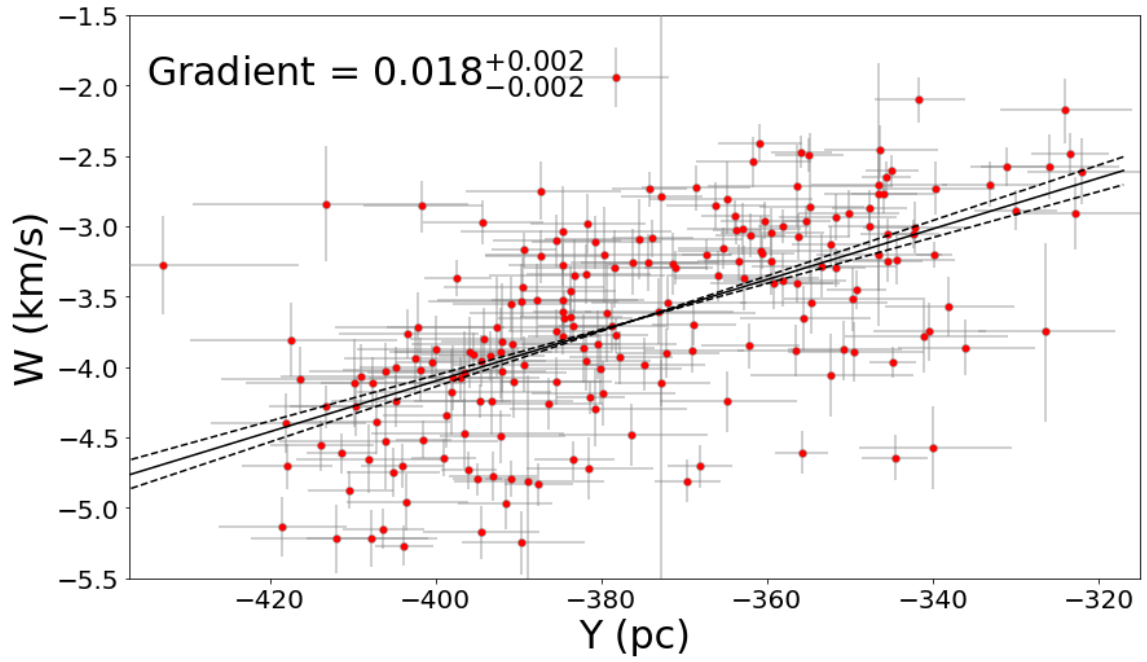
Figure 6.13: Y vs W rotation of Vela OB2 sources (red) with MCMC linear best fit and 16th and 84th percentiles shown as solid and dashed lines respectively.

at birth, provides a potentially model-free estimate of the age of these stars.

Inverting the rates of expansion for the Vela OB2 association as shown in Fig. 6.8 results in timescales of $12.82^{+0.88}_{-0.77}$ Myr in X, $22.73^{+2.91}_{-1.89}$ Myr in Y and $19.23^{+1.60}_{-1.37}$ Myr in Z. The kinematic age is 13-23 Myr for the association, which is consistent with the literature age of 16-20 Myr and mean SED age of 15 Myr (Section 6.2.3). It is therefore feasible that the expansion of Vela OB2 may have begun at, or close to, the time of its formation, and that it has been expanding ever since.

6.4   Motion of the groups

Figure 6.14 shows the positions of sources with significant EW(Li)s colour-coded to indicate the kinematic groups they are allocated to. The vectors indicate the mean proper motions of each group with respect to the mean proper motion of the Vela OB2 association (red) and are located at the mean positions of their respective groups. The vectors are scaled to show the relative motion of the group over 1 Myr. This figure shows that the three main clusters (γ Vel, P Puppis and NGC 2547) have significantly different proper motions than the Vela OB2 association.

6.4.1   Inferring past and future position with epicycle approximation traceback

With 6D positions and velocities for YSOs in our sample we can estimate the relative positions of these sources both backwards and forwards in time to estimate their configuration both in the past (including at their birth) and in the future. In order to incorporate the component of stellar motion due to oscillation through the Galactic
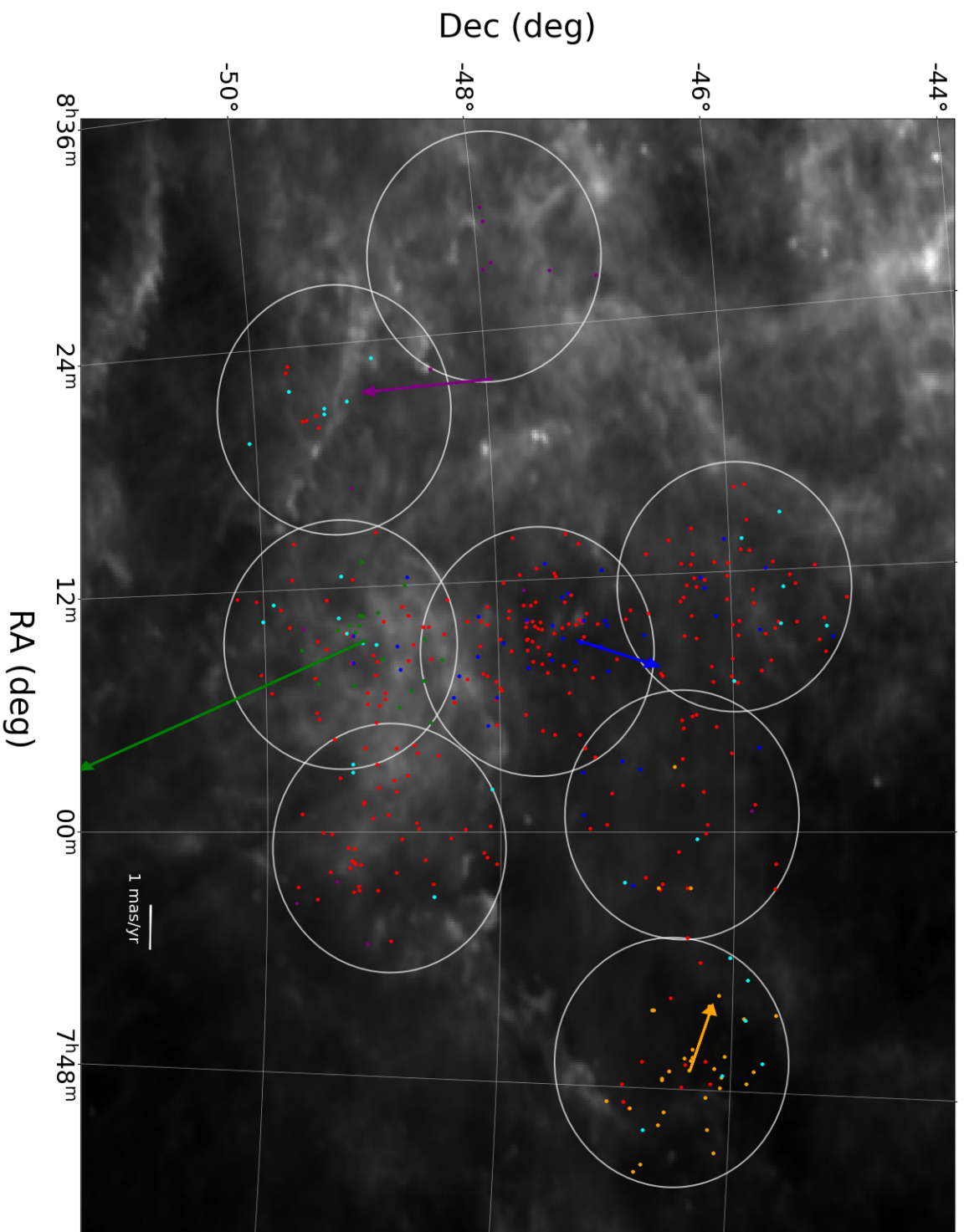
Figure 6.14: Positions of targets in 8 fields selected from the regions of greatest proper motion density (Fig. 6.4). Colour-coding is the same as Fig. 6.4. The vectors indicate the mean proper motions of each group relative to the mean proper motion of the Vela OB2 association (red). The magnitude scale (mas/yr) of proper motion vectors is indicated by the scalebar in the bottom right. The proper motion vectors illustrate the motion of each group over a period of 1 Myr.

plane we calculate new positions using the epicycle approximation. We use the orbital equations from Fuchs et al. (2006). We use the Oort A and B constants from Feast & Whitelock (1997), the local disc density from Holmberg & Flynn (2004), the local standard of rest velocity from Schönrich, Binney & Dehnen (2010) and a solar Z distance above the Galactic plane of 17 pc (Karim & Mamajek 2017). Figures 6.15 - 6.18 show the mean positions of the γ Vel (blue), P Puppis (yellow) and NGC 2547 (green) clusters, and the individual positions of sources belonging to the Vela OB2 group (red), distant group (purple) and outlier group (cyan) at various points in time in both the past and the future. Figures 6.15 and 6.16 show the absolute positions (providing a wide-field view), while Figures 6.17 and 6.18 show the relative positions (allowing the internal dynamics to be visualised). In all the plots we consider the three clusters to be gravitationally bound entities and therefore represent those clusters as single points (overcoming the need to consider their internal dynamics), while for the Vela OB2 associations and the other groups we show the individual sources (where the internal dynamics of these unbound systems will be less important to their past and future dynamics).

It is clear from Figs. 6.15 - 6.18 that the cluster NGC 2547 is an interloper to the Vela OB2 association which happens to be passing through the region at the present time. The mean position of NGC 2547 (green) is outside the volume of Vela OB2 at 5 Myrs past and is > 100pc away at 20 Myrs past (Fig 6.15). Many members of the light blue group also appear to be young interlopers. The γ Vel and P Puppis clusters, however, remain within the volume of the Vela OB2 association up to 20 Myrs forward and 15 Myrs backwards in time, at least to the estimated time when they would have formed (see Section 6.2.3). This indicates that these two clusters have always belonged to the association, that they formed as dense subregions within the substructure of the association. In Figs. 6.16 and 6.18 it appears that the γ Vel and P Puppis clusters will move further apart, following the overall expansion pat-
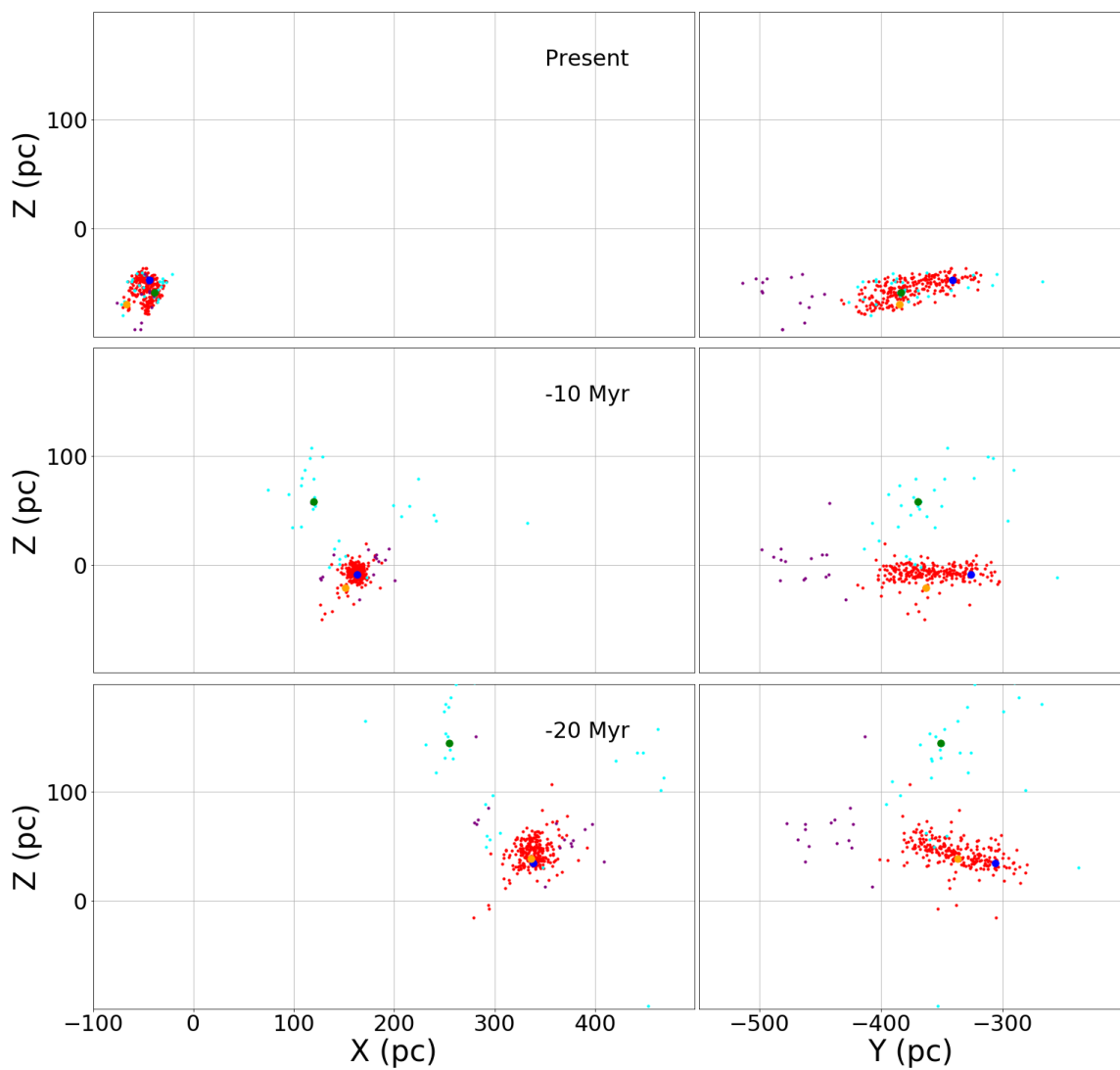
Figure 6.15: Mean past absolute positions of the γ Vel (blue), P Puppis (yellow) and NGC 2547 (green) clusters (shown on the assumption that the clusters are gravitationally bound entities), and the individual positions of sources belonging to the Vela OB2 group (red), distant group (purple) and outlier group (cyan), in absolute X vs Z and Y vs Z positions, back in time in 10 Myr intervals up to 20 Myrs from the present.
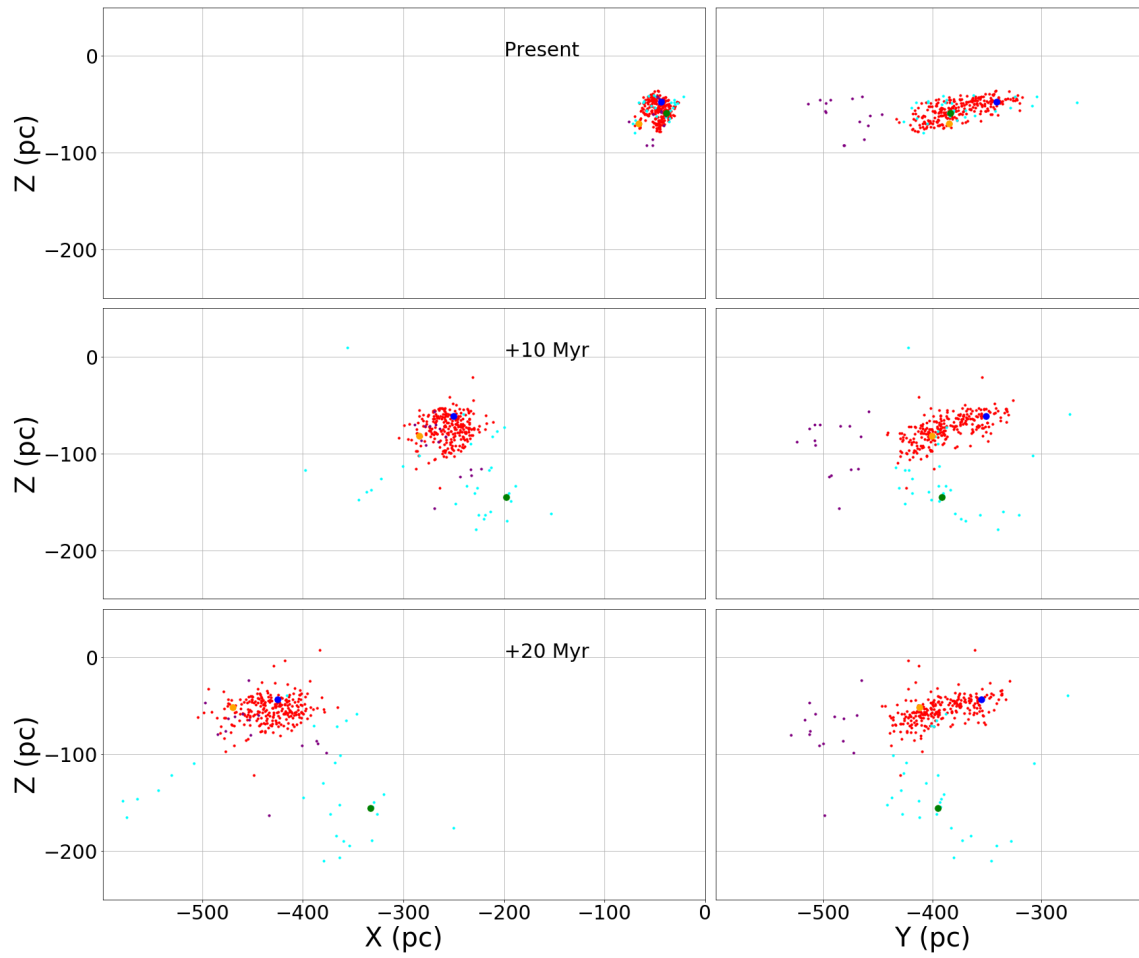
Figure 6.16: Mean future absolute positions of the γ Vel (blue), P Puppis (yellow) and NGC 2547 (green) clusters, and the individual positions of sources belonging to the Vela OB2 group (red), distant group (purple) and outlier group (cyan), in absolute X vs Z and Y vs Z positions, forward in time in 10 Myr intervals up to 20 Myrs from the present.
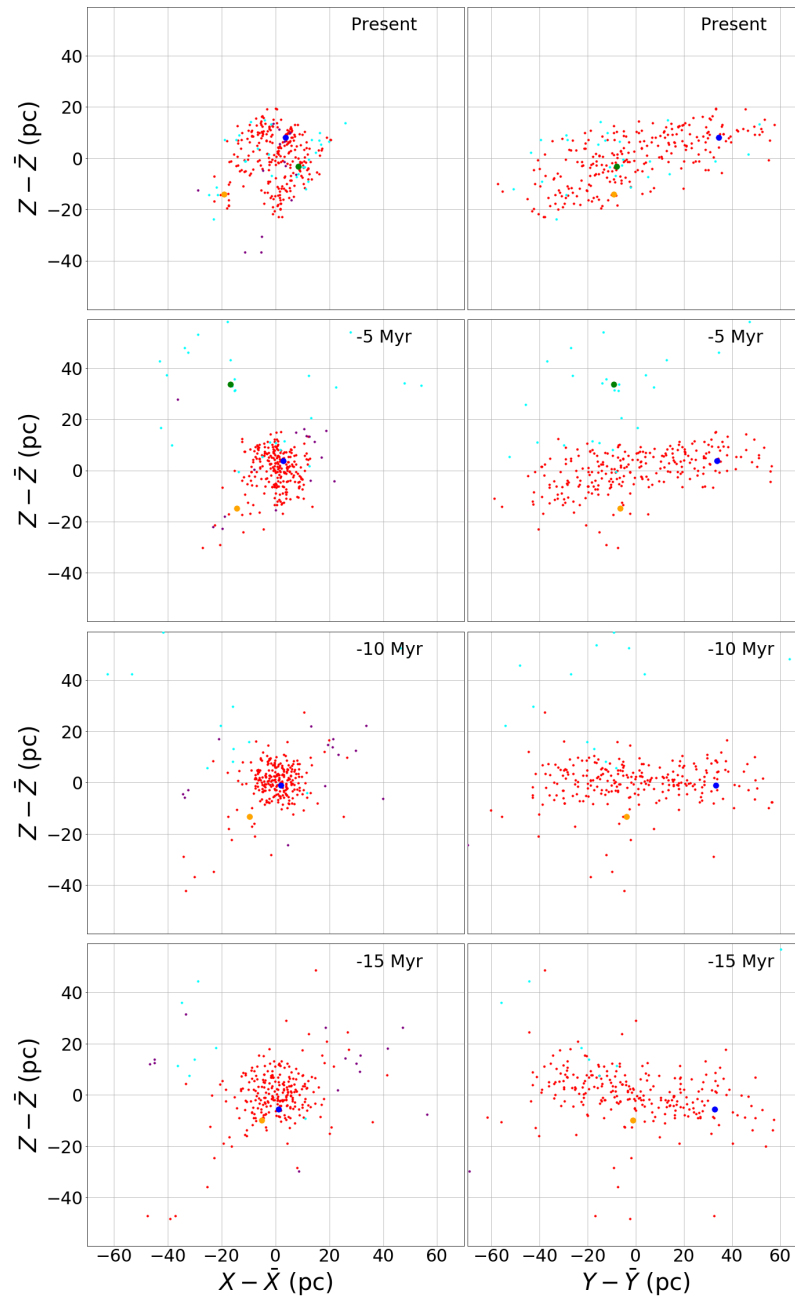
Figure 6.17: Panel of figures showing the mean positions of the γ Vel (blue), P Puppis (yellow) and NGC 2547 (green) clusters, and the individual positions of sources belonging to the Vela OB2 group (red), distant group (purple) and outlier group (cyan), in X vs Z and Y vs Z positions relative to the center of the Vela OB2 group, back in time in 5 Myr intervals up to 15 Myrs from the present.
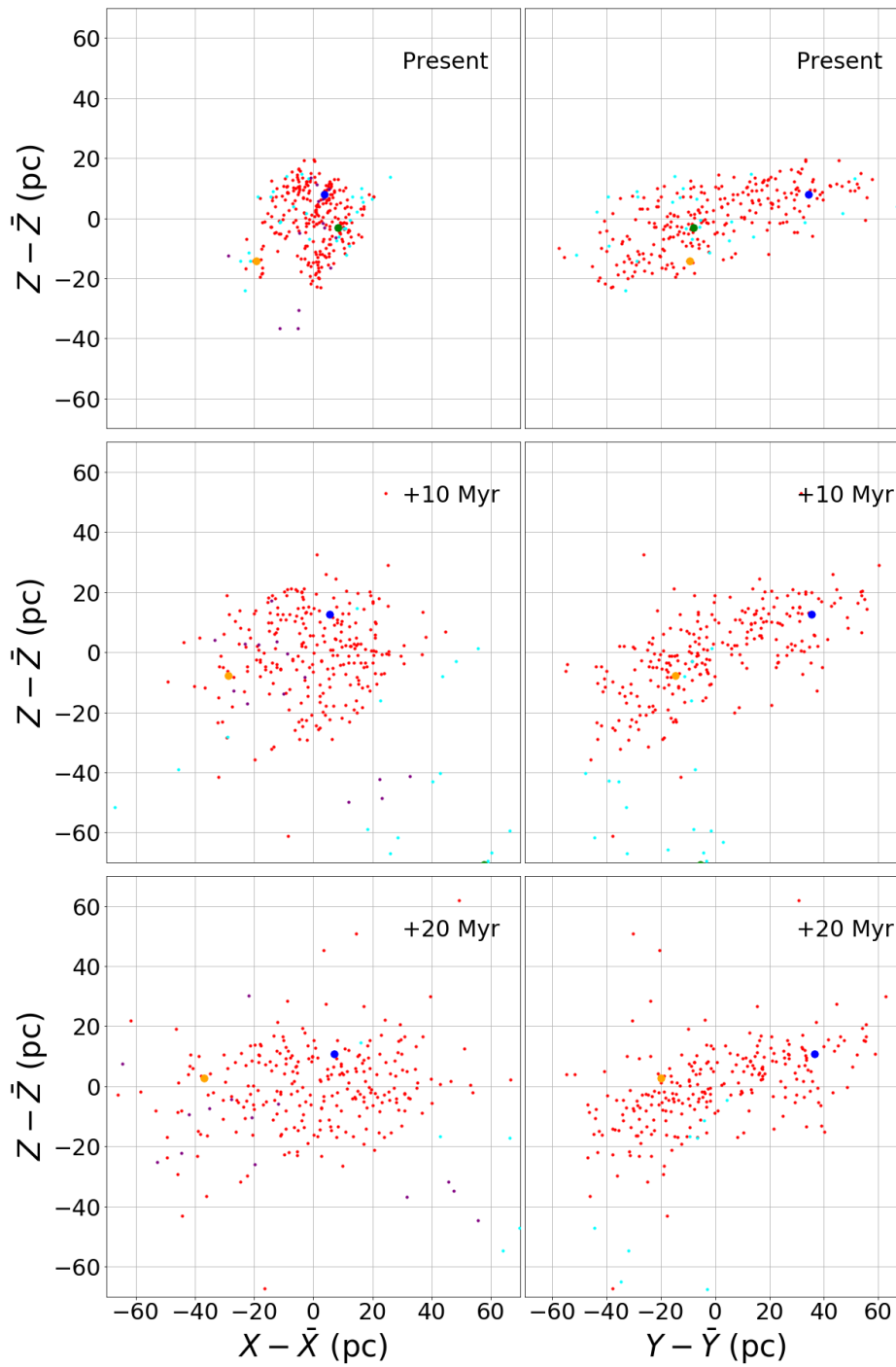
Figure 6.18: Panel of figures showing the mean positions of the γ Vel (blue), P Puppis (yellow) and NGC 2547 (green) clusters, and the individual positions of sources belonging to the Vela OB2 group (red), distant group (purple) and outlier group (cyan), in X vs Z and Y vs Z positions relative to the center of the Vela OB2 group, forward in time in 10 Myr intervals up to 20 Myrs from the present.

tern of the Vela OB2 association.

In Figs. 6.15 and 6.17 the γ Vel cluster is projected against the center of the association in X vs Z at 20 Myr in the past, approximately when it formed, despite being $\sim$40 pc closer, though since Y correlates very closely with the line-of-sight, positions in this direction are the most affected by parallax errors so the apparent spread may not be real. At the time of its formation, 15 Myr ago, the P Puppis cluster is offset from the bulk of the association. Also at 10 Myr past the association appears at its most compact, which would be expected for the initial configuration of an expanding group, in contrast to our amended SED age estimate for this group of 20 Myr (Section 6.2.3).

Notably in the Y vs Z plot in Fig. 6.17 is the change in the apparent tilt of the association group, suggesting that the association is rotating. This rotation can also be seen in Fig. 6.13 in the panel of W vs Y, where a $> 15\sigma$ significant trend is observed (see also Table 6.3), thus confirming this rotation.

This traceback using an epicyclic approximation does not take dynamical interactions within the association into account, investigations using N-body simulations would be needed to assess the accuracy of this method.

6.5 Identifying candidate runaway stars

As mentioned previously there is a group of sources with kinematics distinct from the Vela OB2 association and the three clusters in the region which have been plotted in cyan in Figs. 6.4 - 6.18. It is apparent in Fig. 6.4 that these sources have proper motions distinct from the other groups. Many of their proper motion vectors also appear to point away from the centers of the clusters in this region, indicating that some of these sources may be "runaway stars", stars belonging initially to a bound

cluster but since ejected at high velocity due to dynamical interactions.

One method of identifying runaways would be to calculate tidal radii for the clusters in the region of our sample and to select sources where a traceback of the proper motion relative to those clusters would intersect the cluster radius, i.e. the source's point of closest approach is inside the cluster radius. But this requires that we estimate the masses of these clusters in order to calculate tidal radii, and our sample is incomplete in that sources are only within a specific magnitude range and only within certain fields of position. Any attempt to estimate cluster mass with our sample will be significantly biased. Therefore we make a simple estimate of cluster radii by specifying the radii in which 50% of cluster members are contained as an estimate of a "half-mass radius".

In Fig. 6.19 candidate runaways are plotted in a linear projection coordinate frame (x,y) with their velocities relative to the clusters colour-coded by the clusters they trace back from. We use a linear projection coordinate frame (Helmi et al. 2018) with a set distance (400 pc) to trace these sources' proper motions without the curvature of the celestial coordinate system. Any sources from this group whose proper motion trace back inside the radius of one of the three clusters is a candidate runaway. 10 sources are identified as candidate runaways using this method and 3 of these are possible runaways from either the γ Vel cluster or NGC 2547 (hence these sources are shown with multiple relative proper motion vectors with different lengths). 6 of these are included in Cantat-Gaudin et al. (2019a), 5 belong to their population 4 (coeval with NGC 2547), and 1 belongs to their population 3, which is the only candidate runaway from P Puppis included. No candidate runaways belong to their population 7 (coeval with Vela OB2 and γ Vel), despite $\sim 80\%$ of our Li-rich sources belonging to that population.

In Table 6.4 we list the Gaia IDs of these candidate runaways, the groups they are candidate runaways from, their SED masses, SED ages, 3D velocities relative to the group they are candidate runaways from (v_{3D}), time since point of closest
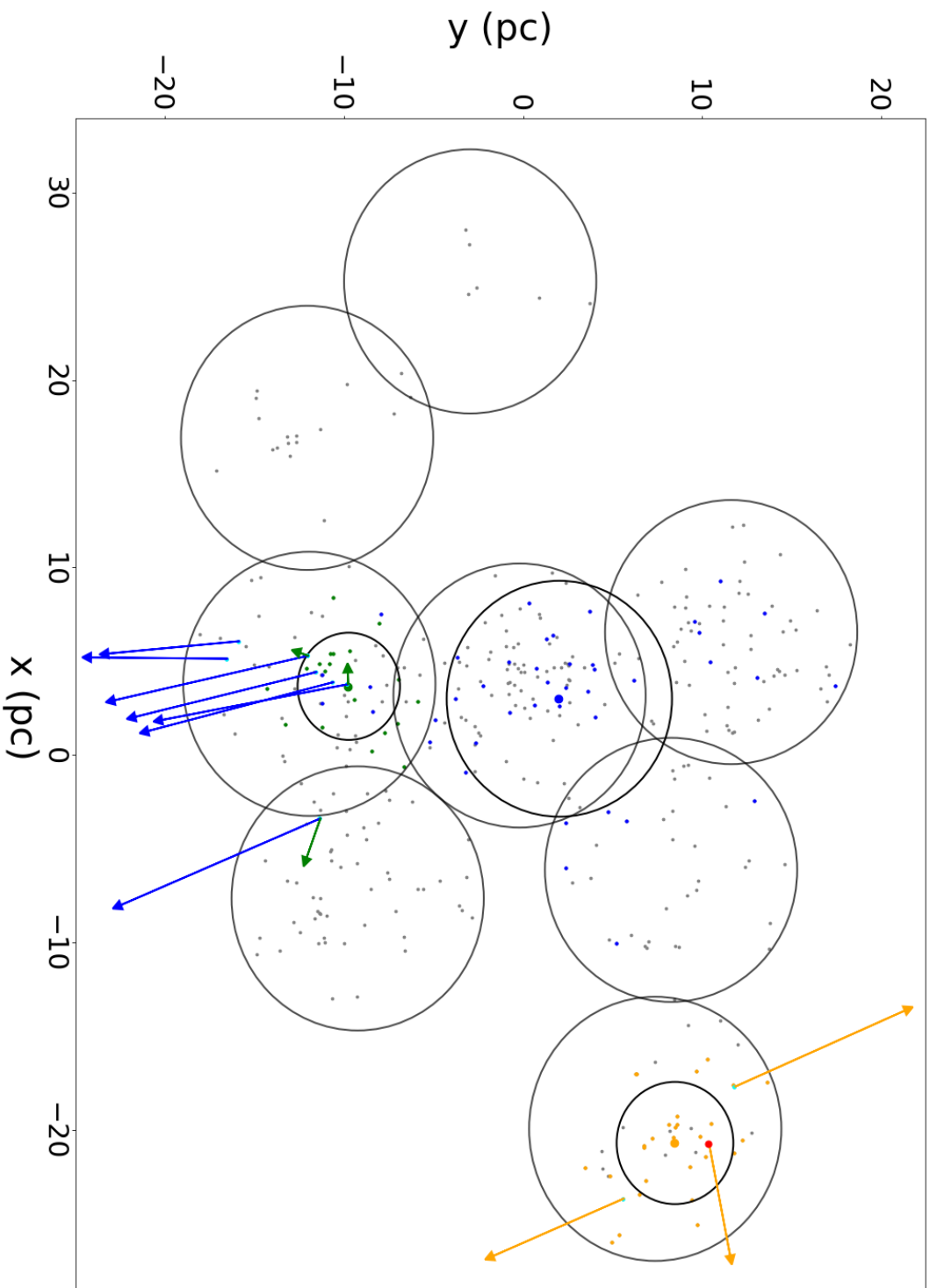
Figure 6.19: A plot of candidate runaways selected only from the cyan group (see Figs. 6.4 - 6.16). Sources are plotted by their relative position in x, y and their vectors indicate their proper motion relative to the cluster they may have been ejected from. The mean positions of the clusters are represented by the large coloured points (γ Vel - blue , P Puppis - yellow, NGC 2547 - green). Candidate runaway sources are colour-coded according to the cluster they may have been ejected from. Other sources in our sample which are not selected as candidate runaways are plotted in grey and the 8 fields of our observations are outlines in grey. Estimated cluster radii are shown in black.

Gaia ID	Group	SED Mass [M$_\odot$]	SED Age [Myr]	v_{3D} [pc Myr^{-1}]	t_e [Myr]	ΔD [pc]	ΔRV [km s^{-1}]
5514251444112598656	γ Vel	$0.72^{+0.01}_{-0.01}$	$13.8^{+1.4}_{-1.3}$	8.30 ± 0.06	0.68 ± 0.98	83.92 ± 6.91	-6.78 ± 3.32
5514275805167770240	γ Vel	$0.72^{+0.01}_{-0.01}$	$16.7^{+1.4}_{-1.3}$	8.84 ± 0.02	0.66 ± 0.10	72.04 ± 5.39	-7.16 ± 0.59
5514349506807731200	γ Vel	$0.81^{+0.01}_{-0.01}$	$13.2^{+0.9}_{-1.2}$	10.41 ± 0.056	0.33 ± 0.02	44.26 ± 3.85	-2.35 ± 1.53
5514349506807731200	NGC 2547	$0.81^{+0.01}_{-0.01}$	$13.2^{+0.9}_{-1.2}$	1.91 ± 0.74	1.56 ± 5.70	2.39 ± 3.85	1.75 ± 1.53
5514362357349925248	γ Vel	$0.71^{+0.01}_{-0.01}$	$20.9^{+1.6}_{-1.5}$	10.87 ± 0.01	0.34 ± 0.02	41.08 ± 4.05	-5.52 ± 0.74
5514506359010085120	γ Vel	$0.75^{+0.01}_{-0.01}$	$21.0^{+1.5}_{-1.7}$	12.96 ± 0.01	0.34 ± 0.01	21.17 ± 2.78	-4.33 ± 0.58
5514506359010085120	NGC 2547	$0.75^{+0.01}_{-0.01}$	$21.0^{+1.5}_{-1.7}$	2.65 ± 1.27	0.89 ± 0.10	-20.69 ± 2.78	-0.23 ± 0.58
5514554771884454272	γ Vel	$0.73^{+0.01}_{-0.01}$	$23.6^{+2.5}_{-2.0}$	11.17 ± 0.01	0.31 ± 0.01	42.24 ± 3.83	-5.51 ± 0.63
5514559238650415744	γ Vel	$0.72^{+0.01}_{-0.01}$	$14.4^{+1.3}_{-1.2}$	9.56 ± 0.13	0.30 ± 0.03	39.37 ± 5.67	0.68 ± 0.59
5514559238650415744	NGC 2547	$0.72^{+0.01}_{-0.01}$	$14.4^{+1.3}_{-1.2}$	4.88 ± 0.77	0.05 ± 22.85	-2.50 ± 5.67	4.78 ± 0.59
5530649148210291328	P Puppis	$0.79^{+0.01}_{-0.01}$	$30.3^{+2.6}_{-3.2}$	11.27 ± 0.01	0.13 ± 0.01	24.56 ± 3.47	-7.08 ± 0.62
5530691754285644032	P Puppis	$0.74^{+0.01}_{-0.01}$	$17.4^{+2.6}_{-2.9}$	9.67 ± 0.02	0.02 ± 0.03	-0.34 ± 4.05	5.02 ± 0.62
5531061155834669184	P Puppis	$0.48^{+0.04}_{-0.05}$	$5.0^{+1.7}_{-1.4}$	12.41 ± 0.02	0.12 ± 0.05	18.77 ± 9.12	2.30 ± 0.60

Table 6.4: Information for the individual sources identified as candidate runaways from the main clusters shown in Fig. 6.19. Columns are the Gaia IDs, the groups they are candidate runaways from, SED masses, SED ages, 3D velocities relative to the group they are candidate runaways from (v_{3D}), time since point of closest approach to the center of the group they are candidate runaways from (t_e, calculated from the projected positions and proper motions only), relative line-of-sight distance from the center of the group they are candidate runaways from (pc) and relative radial velocity.

approach to the center of the group they are candidate runaways from (t_e), relative line-of-sight distance from the center of the group they are candidate runaways from (ΔD) and relative radial velocity (ΔRV).

The majority of these sources have small 3D velocities relative to the clusters and are potentially examples of what have become known as 'walk-away' stars (v_{3D} < 30 km s^{-1}; de Mink et al. 2014; Schoettler et al. 2020).

There are several checks we can make to confirm whether or not these sources are likely runaways:

- Age test: The SED age for the star, with the factor 1.25 correction (see Section 6.2.3) needs to be consistent with the cluster age for it to have been a likely member of that cluster in the past (though a broad agreement is sufficient given the multitude of factors that can affect individual stellar ages).

- Ejection timescale test: The ejection time needs to be less than or equal to the age of the cluster the star is ejected from. The ejection times for these sources are much lower than their SED ages because these sources are still located in close proximity to the clusters due to the limited field of view of our spectroscopic survey. All of our sources therefore pass this test.

- RV test: We compare the sources' line of sight distance from the cluster (ΔD) with their ejection time to calculate the necessary relative RV to traverse this distance in the available time. This is then compared to the measured relative RV (ΔRV) to check for consistency, allowing for a disagreement up to a few tens of km/s due to possible binarity.

In Table 6.5 we assess whether each source is a likely runaway based on these checks.

The only source that seems to be a likely runaway is Gaia ID 5530691754285644032, which has an SED age and kinematics consistent with having been recently ejected (0.02 ± 0.03 Myr) from the P Puppis cluster at a velocity of 9.67 ± 0.02 kms^{-1}. This

Source	Cluster	Age test	t_e [Myr]	RV test	Likely run-away
5514251444112598656	γ Vel	✓	0.68 ± 0.98	✗	✗
5514275805167770240	γ Vel	✓	0.66 ± 0.10	✗	✗
5514349506807731200	γ Vel	✓	0.33 ± 0.02	✗	✗
5514349506807731200	NGC 2547	✗	1.56 ± 5.70	✓	✗
5514362357349925248	γ Vel	✓	0.34 ± 0.02	✗	✗
5514506359010085120	γ Vel	✓	0.34 ± 0.01	✗	✗
5514506359010085120	NGC 2547	✗	0.89 ± 0.10	✗	✗
5514554771884454272	γ Vel	✓	0.31 ± 0.01	✗	✗
5514559238650415744	γ Vel	✓	0.30 ± 0.03	✗	✗
5514559238650415744	NGC 2547	✗	0.05 ± 22.85	✓	✗
5530649148210291328	P Puppis	✗	0.13 ± 0.01	✗	✗
5530691754285644032	P Puppis	✓	0.02 ± 0.03	✓	✓
5531061155834669184	P Puppis	✗	0.12 ± 0.05	✗	✗

Table 6.5: Rotation gradients of MCMC linear best fit models for the sample populations of the Vela OB2 association, NGC 2547, P Puppis and γ Vel clusters for combinations of cartesian position and velocity dimensions, as well as uncertainties given by the 16% and 84% percentiles of MCMC fits.

is the source which in Fig 6.19 is located within the radius of the P Puppis cluster.

Whilst we have only found 1 likely runaway in our sample, this study highlights the importance of using relative distances and RVs or estimating ages to verify candidate runaways, as out of 10 sources whose proper motions were consistent with being runaways, all but 1 were discarded based on inconsistent age or kinematics. This also indicates the importance of spectroscopic follow-up for candidate runaway stars to obtain RVs for this check.

The sources in this group that do not correlate with any particular kinematic population and are determined not to be runaways may be examples of kinematically 'hot' young stars, such as those identified in Binks, Jeffries & Wright (2020), stars whose kinematics are distinct from nearby groups, or that belong to a group with a relatively high velocity dispersion. It is also possible that some of them may be ejectees from groups of young stars outside the fields of our observations. However, in Section 6.2.2 we noted that the majority of sources in this group matched to population 4 of Cantat-Gaudin et al. (2019a), the same population that contains NGC 2547, and in Figures 6.15 - 6.18 many of these sources follow the projected motion of NGC 2547 in a halo. This suggests that some of these sources may be the remnants of a sparse population that formed coeval to NGC 2547 and with similar kinematics, but has now mostly dispersed among the younger Vela OB2 population.

6.6   Discussion

In this chapter, we have combined Gaia astrometry with spectroscopic RVs and EW(Li)s to analyse the 6D kinematics across the Vela OB2 region. Our main results are as follows:

- We have identified considerable substructure in the form of multiple distinct

groups in Vela OB2, namely the known clusters γ Vel and NGC 2547, a previously poorly-studied cluster, P Puppis, a population of YSOs ~ 100 pc more distant than the association, and the association itself.

- We find significant evidence ($> 9\sigma$) of expansion of the Vela OB2 association in all directions, though it is somewhat anisotropic. We calculate a kinematic traceback age of 13-23 Myr for Vela OB2 based on its expansion pattern, which is in good agreement with its estimated isochronal age of 15-20 Myr (Section 6.2.3).

- We have used an epicycle approximation to investigate the relative positions and motions of these groups and clusters, up to 20 Myrs forwards and backwards in time. We find that NGC 2547 is an interloper cluster to Vela OB2 which happens to be passing through the region at the present time and would have been ~ 110 pc distant at the time of Vela OB2's formation. Both the γ Vel and P Puppis clusters, however, seem to have originated from inside the volume of the association, with implications for their formation.

- We have identified a group of sources with kinematics different to the association and clusters and identified 10 runaway candidates based on their proper motions, but conclude that only 1 (Gaia ID 5530691754285644032) has an SED age and RV consistent with the cluster it's moving away from. This highlights the value of spectroscopy and age estimation for verifying runaway candidates.

We now discuss each of these results in more detail.

6.6.1 Structure of Vela OB2 and nearby clusters

Until recently, the structure of the Vela OB2 association was not well constrained. Studies of the region had hinted at the existence of a sparse, widespread population of young stars (Jeffries et al. 2014; Sacco et al. 2015) but it was not until the availability of Gaia DR2 proper motions and parallaxes that a structural and kinematic investigation over the whole region could be done (Cantat-Gaudin et al. 2019a). Even then, radial velocities were lacking. This chapter presents the first 6D kinematic study of the association by combining Gaia astrometry with spectroscopic RVs.

We have found that Vela OB2 is not a single homogenous entity. Rather, it is a highly substructured complex containing multiple open clusters with a range of ages, surrounded by a widespread and dispersed population of young stars, exhibiting complex dynamics. We have confirmed that the sparse population surrounding the γ Vel and NGC 2547 clusters (Jeffries et al. 2014; Sacco et al. 2015) belongs to the Vela OB2 association and has different kinematics from either. We have also found that our membership for the association and clusters agrees well with the populations identified in Cantat-Gaudin et al. (2019a), though we have separated their population 7 into its more detailed substructure, namely the γ Vel and P Puppis clusters and the Vela OB2 association.

6.6.2 Expansion of the association

In this chapter, we have calculated linear expansion rates for each major group in our sample separately, and have found strong evidence ($> 9\sigma$ in all directions) for expansion of the Vela OB2 association that is not apparent in any of the clusters, though this expansion is notably anisotropic ($0.078^{+0.005}_{-0.005}$, $0.044^{+0.004}_{-0.005}$, $0.052^{+0.004}_{-0.004}$ kms^{-1}/pc). These expansion rates were then used to calculate a kinematic age for the association

(13-23 Myr), which is in good agreement with literature ages (15-20 Myr).

Evidence for the expansion of OB associations has been found in recent studies. Cantat-Gaudin et al. (2019a) calculate linear expansion rates for the dispersed populations they identify in the Vela-Puppis region, including that corresponding to Vela OB2 (population 7; $\chi_X = 4.40 \pm 0.35$, $\chi_Y = 5.68 \pm 1.10$, $\chi_Z = 5.98 \pm 0.27$), and find evidence for expansion in all. In our study, however, we only observe expansion in the main Vela OB2 group, while the open clusters, once separated, do not show such trends.

6.6.3   Spatial configuration

We have constrained the initial configuration of Vela OB2 and probed its future evolution by tracing backwards and forwards in time the motion of stars in Vela OB2 and the bulk motion of the clusters in its vicinity.

By tracing back its motion up to 20 Myr in the past, we have found that the open cluster NGC 2547 formed >100 pc outside of the Vela OB2 region and is an interloper in the association at the present time. This, and its older age, indicates that it was part of a separate star formation event from Vela OB2. On the other hand, the γ Vel and P Puppis clusters appear to have formed within the volume of the association, indicating that they originated as compact substructures of Vela OB2. This is supported by their similar ages, while NGC 2547 is approximately twice as old as the association.

The γ Vel cluster appears to have formed relatively centrally within the association, and at a similar time to it, suggesting its formation may have been strongly linked to the formation of the association as a whole, whereas the P Puppis cluster is younger and appears to have formed on the edge of the association, suggesting a total period of star formation up to 10 Myr within the region.

6.6.4   Verification of runaways

We identify a number of young stars in the region whose kinematics are not consistent with being members of a particular kinematic group. 10 of these sources have proper motions consistent with having been recently ejected from one (or more) of the clusters in the region. We assess the validity of these candidate runaway stars by comparing their distances, RVs and ages to the clusters they are candidate ejectees from and find that only 1 source (i.e., 10% of our candidate runaway sample) is still consistent with being a runaway source ejected from one of these clusters. The other sources could be examples of kinematically 'hot' young stars (Binks, Jeffries & Wright 2020) which are not associated with a larger group.

7   Conclusions

This thesis presents the results of studies of the structure and dynamics of the Vela OB2 association using a combination of Gaia DR1 and DR2 astrometry, photometry and spectroscopy obtained from two separate observing runs with the HERMES and 2dF instruments at the AAT.

In Chapter 3 we have combined Gaia DR1 and 2MASS photometry to map out the PMS low-mass population of the Vela OB2 association and compared it to the known high-mass population. This work was extended using Gaia DR2 photometry and astrometry and also formed the basis for selecting targets for spectroscopic observations (Chapter 4).

The first set of spectra was used to obtain RVs and EW(Li)s for 341 PMS stars in the vicinity of the γ Vel cluster. The EW(li)s were used to confirm the youth of 216 of these, whose RVs we combined with Gaia DR2 astrometry to investigate the 6D kinematics of the two populations detected by Jeffries et al. (2014). We find $> 4\sigma$ evidence for anisotropic expansion in the association population.

The second set of spectra was used to obtain RVs and EW(Li)s for >2500 sources in 8 fields across the Vela OB2 region, confirming 395 of these as PMS stars based on their EW(Li) values. We separate the sample into groups using Gaia DR2 astrometry and spectroscopic RVs and find that the Vela OB2 association has significant substructure, with different groups at a range of ages exhibiting distinct 3D kinematics and at different distances. These groups include the sparse Vela OB2 association itself, the known γ Vel and NGC 2547 clusters, a previously poorly-studied cluster, P Puppis, and a number of more dispersed young stars. This supports the growing volume of recent evidence that OB associations are not homogenous groups, but are amalgamations of multiple populations resulting from complex formation and evolution processes.

Recently, similar findings have been made in other nearby associations. Wright et al. (2016) investigated the structure and dynamical state of Cyg OB2 using a sample of stars selected by X-ray and spectroscopy. They found significant kinematic substructure within the unbound association. Damiani et al. (2019) use Gaia DR2 photometry and astrometry to identify and investigate the PMS population of the Scorpius-Centaurus association, and find a number of compact subclusters within the association with distinct kinematics. Zari, Brown & de Zeeuw (2019) use the DBSCAN clustering algorithm to identify subgroups in the Orion star forming region and find that they vary in kinematics and age.

These recent studies and the work in this chapter all provide evidence that OB associations are highly substructured, both spatially and kinematically. This substructure argues against OB associations (as a whole) being the expanded remnants of single, dense clusters (Tutukov 1978) and instead suggests a more substructured, and therefore complex, formation picture.

Large scale radial velocity surveys of other nearby OB associations could be combined with Gaia astrometry to investigate the 6D substructure of similar entities at a range of different ages and environments. Comparison between the kinematic properties of multiple associations could reveal key processes in the evolution of star forming regions.

We find significant evidence for expansion in Vela OB2 but not for the major clusters in the region, which suggests that, while the main portion of the association may be unbound and expanding, the most compact subgroups will remain as bound open clusters. The expansion of Vela OB2 has allowed us to calculate a kinematic age for the association, which we estimate to be 13 - 23 Myr, in good agreement with the isochronal age of 15 - 20 Myr.

Other investigations (Wright et al. 2016; Wright & Mamajek 2018; Ward & Kruijssen 2018) have failed to find conclusive evidence for expansion in other OB associations. But the key difference between these studies and those that do find ev-

idence of expansion (Cantat-Gaudin et al. 2019a; Armstrong et al. 2020) is that the former did not attempt to separate the subgroups and clusters within the association while the latter did. This suggests that it can be helpful to identify the kinematic subgroups within an OB association when searching for evidence of expansion in the association.

The expansion of the association indicates that it is gravitationally unbound and that it would have been more compact in the past. At its formation 15-20 Myr ago, the association would have been 1-2 orders of magnitude denser than it is at present. This raises questions about its formation. Did the association become unbound after its formation while the compact clusters remained bound (Baumgardt & Kroupa 2007)? Or did the association form unbound except for the clusters (Clark, Bonnell & Klessen 2008)?

The anisotropy of its expansion suggests that the association is either experiencing external forces stretching it in a particular direction, or that it has inherited anisotropic motion from its initial conditions. The former could be due to the spatial distribution of surrounding molecular clouds during the gas expulsion process (reminiscent of the 'cruel cradle effect', Kruijssen et al. 2012) Evidence of the latter scenario has been suggested by Wright & Parker (2019), who attribute anisotropic expansion trends in the Lagoon Nebula Cluster (observed by Wright et al. 2019) to the formation of a cluster by anisotropic collapse and the resultant 'bounce' that leads to an observed expansion pattern. A similar pattern could be observed here, particularly given the central location of the γ Vel cluster within the Vela OB2 association during their formation.

Investigations of expansion in substructures of other associations are needed to identify the correct evolution scenario, particularly of younger associations whose present states are closer to their initial conditions.

We study the past and future configurations of the region using an epicyclic approximation to trace the motion of clusters and individual sources over time. We find

evidence that the cluster NGC 2547 is an interloper in this region and was formed earlier than and distant from Vela OB2, while the γ Vel and P Puppis clusters were likely formed within the association. The γ Vel cluster appears to have formed relatively centrally within the association, and at a similar time to it, suggesting its formation may have been strongly linked to the formation of the association as a whole. The P Puppis cluster is younger and appears to have been on the edge of the association at the time of it's formation. It remains to be seen whether the P Puppis cluster is part of some wider age gradient across the association.

Few studies have attempted this kind of investigation before due to the lack of precise 6D kinematics, but by combining Gaia astrometry with precise RV surveys, this may be possible in other nearby star forming regions.

We have used an epicycle approximation to trace the motions of clusters and sources, but this approximation does not take into account the effects of close gravitational interaction between sources in these groups. Detailed N-body simulations would be needed to determine what types of initial configuration are possible given the current structure and kinematics of the region. Comparison to GMC star formation models (such as Dobbs et al. 2017) could also be used to constrain the dispersal timescales and spatial configuration at birth for systems such as these.

Future investigation could be made into the distribution of sources at different ages within Vela OB2, to look for a possible age gradient across the region which would inform us as to the mode of formation of these groups and explain the age difference between P Puppis and γ Vel.

We also attempt to identify candidate runaway stars in this sample, selecting on consistent proper motion, but then verifying using RVs and age. Despite 10 candidates based on their PMs, we find only 1 likely runaway after our verification process. This highlights the importance of such criteria and the use of RVs and stellar ages for confirming runaway candidates.

While unsuccessful in detecting multiple runaways, this study does highlight

the importance of RVs for assessing candidate runaway stars. Other recent studies that have searched for runaway stars (McBride & Kounkel 2019; Schoettler et al. 2020; Farias, Tan & Eyer 2020) have attempted to detect runaways primarily using Gaia DR2 proper motions, but have incomplete RV information. Our study highlights the value of obtaining RVs when assessing candidate runaway stars and shows the considerable decrease in the number of possible runaways that may occur when such information is taken into account when doing this.

To conclude, this work has revealed the complex spatial, kinematic and temporal structure of the Vela OB2 association, identifying various groups and clusters within it, confirming the expansion of the association, and revealing the structure and configuration of the region throughout its formation.

7.1   Future work

The spectra for sources in our fields of observation cover a large wavelength range, yet so far we have only used them to measure RVs and EW(Li)s. We could obtain much more information from them, including other age indicators such as Hα emission. The Hα emission line at 6563 Å is a strong indication of youth in PMS stars, arising from circumstellar disc accretion and chromospheric activity. Obtaining EW(Hα) and Hα 10% (Lanzafame et al. 2015) values for sources in our sample would allow us to identify possible accretors and to calculate mass accretion rates (Frasca et al. 2015).

In Chapter 6 we distinguish between the different kinematic groups in our sample largely based on prior knowledge of their membership and kinematics in the literature (Section 6.2.1). Other methods of identifying clusters have been recently applied to Gaia data, such as clustering algorithms (Kounkel et al. 2018; Cánovas et al. 2019; Hunt & Reffert 2021) and Gaussian mixture models (Gao 2018; Cantat-

Gaudin et al. 2019b). The results of such automated approaches applied to our sample could be compared to our selection criteria, not only to verify membership of sources in the groups and so the expansion and rotation trends in each group, but also to possibly identify further subgroups within Vela OB2.

A spectroscopic survey of a wider area, perhaps across the whole region studied by Cantat-Gaudin et al. (2019a), could be used to investigate the substructure in each of their identified populations, as we have done for their population 7. This could be used to search for runaway stars that may have been ejected further in the past, and to look for possible age gradients across the entire region. The motion of any substructures found could then be traced back in time to investigate the star formation history of the region.

Comparison with N-body simulations would be helpful in our attempts to trace the past configuration of the association. A better understanding of the dynamical evolution of groups of young stellar objects like these is necessary to correctly interpret the initial configuration from their current state. This would be particularly valuable, for example, for estimating how dense the Vela OB2 association could have been at the time of its formation, which has significant implications for the star and planet formation process.

Since our survey of this region is spatially limited, we can only detect recent (<1 Myr) ejectees. Runaways ejected further in the past would have long since moved away from our fields of observation. In order to detect runaways with a broader range of ejection timescales we could expand on this study by searching a wider area for stars whose kinematics are consistent with them having been ejected from these clusters longer ago. Spectroscopic follow-up would then be required to confirm the youth of such objects and measure RVs with which to test their runaway status.

With precise RVs, future investigations could more accurately identify runaways from groups of young stars. Knowledge of the nature and frequency of dynamical ejections is important for our understanding of dynamical interactions within clus-

ters and the means by which their members may disperse into the field population.

Our spectroscopic sample is comprised of low-mass objects and we only briefly make a comparison between these and the high-mass members for which OB associations are known (Section 3.5). A detailed study of how high-mass stars affect their local environment and neighbouring stars in associations (γ^2 Vel in the γ Vel cluster, supernovae remnants in associations e.g. Cantat-Gaudin et al. 2019c) could reveal key processes responsible for the complex substructure we have observed.

In our investigation we have established that the Vela OB2 association is highly substructured, both spatially and kinematically. It contains multiple open clusters of different ages with distinct kinematics, which are surrounded by a sparse, expanding population. This raises questions about other associations, do they typically form with such substructure and over what timescales is it erased? Also, for the formation of clusters, do they typically form as the dense cores of larger, sparse populations or can they form in relative isolation? In order to answer these questions, further kinematic investigations of multiple populations of young stars at a variety of ages are needed. This will require a combination of large scale astrometry (such as Gaia) with data from complimentary surveys to facilitate the widespread identification of young stars, such as WEAVE (Dalton et al. 2018), 4MOST (de Jong et al. 2019), or eROSITA (Merloni, Nandra & Predehl 2020). The results from this investigation of Vela OB2 can be compared to those of other groups of young stars, allowing us to identify trends in structure and kinematics, contributing to a more complete picture of the large-scale formation and early life of stars.

Bibliography

AAO Software Team, 2015, , ascl:1505.015

Allison R. J., Goodwin S. P., Parker R. J., de Grijs R., Portegies Zwart S. F., Kouwenhoven M. B. N., 2009, ApJL, 700, L99

Ambartsumian V., 1947, Acad. Sci. Armenian SSR, Yerevan

Ambartsumian V. A., 1955, The Observatory, 75, 72

Anderson E., Francis C., 2012, Astronomy Letters, 38, 331

André P., Men'shchikov A., Bontemps S., Könyves V., Motte F., Schneider N., Didelon P., Minier V., Saraceno P., Ward-Thompson D., di Francesco J., White G., Molinari S., Testi L., Abergel A., Griffin M., Henning T., Royer P., Merín B., Vavrek R., Attard M., Arzoumanian D., Wilson C. D., Ade P., Aussel H., Baluteau J.-P., Benedettini M., Bernard J.-P., Blommaert J. A. D. L., Cambrésy L., Cox P., di Giorgio A., Hargrave P., Hennemann M., Huang M., Kirk J., Krause O., Launhardt R., Leeks S., Le Pennec J., Li J. Z., Martin P. G., Maury A., Olofsson G., Omont A., Peretto N., Pezzuto S., Prusti T., Roussel H., Russeil D., Sauvage M., Sibthorpe B., Sicilia-Aguilar A., Spinoglio L., Waelkens C., Woodcraft A., Zavagno A., 2010, A&A, 518, L102

André P., Di Francesco J., Ward-Thompson D., Inutsuka S.-I., Pudritz R. E., Pineda J. E., 2014, Protostars and Planets VI, , 27

Arenou F., Luri X., Babusiaux C., Fabricius C., Helmi A., Muraveva T., Robin A. C., Spoto F., Vallenari A., Antoja T., Cantat-Gaudin T., Jordi C., Leclerc N., Reylé C., Romero-Gómez M., Shih I.-C., Soria S., Barache C., Bossini D., Bragaglia A., Breddels M. A., Fabrizio M., Lambert S., Marrese P. M., Massari

D., Moitinho A., Robichon N., Ruiz-Dern L., Sordo R., Veljanoski J., Eyer L., Jasniewicz G., Pancino E., Soubiran C., Spagna A., Tanga P., Turon C., Zurbach C., 2018, A&A, 616, A17

Armstrong J. J., Wright N. J., Jeffries R. D., Jackson R. J., 2020, MNRAS, 494(4), 4794

Armstrong J. J., Wright N. J., Jeffries R. D., 2018, MNRAS, 480, L121

Ascenso J., Alves J., Lago M. T. V. T., 2009, A&A, 495, 147

Bailer-Jones C. A. L., 2015, PASP, 127(956), 994

Bailer-Jones C. A. L., Rybizki J., Fouesneau M., Mantelet G., Andrae R., 2018, AJ, 156, 58

Balog Z., Siegler N., Rieke G. H., Kiss L. L., Muzerolle J., Gutermuth R. A., Bell C. P. M., Vinkó J., Su K. Y. L., Young E. T., Gáspár A., 2016, ApJ, 832, 87

Baraffe I., Chabrier G., Allard F., Hauschildt P. H., 1998, aap, 337, 403

Baraffe I., Homeier D., Allard F., Chabrier G., 2015, A&A, 577, A42

Bastian N., Goodwin S. P., 2006, mnras, 369, L9

Bastian N., Covey K. R., Meyer M. R., 2010, ARA&A, 48, 339

Bastian N., Gieles M., Lamers H. J. G. L. M., Scheepmaker R. A., de Grijs R., 2005, aap, 431, 905

Baumgardt H., Kroupa P., 2007, MNRAS, 380, 1589

Beccari G., Boffin H. M. J., Jerabkova T., Wright N. J., Kalari V. M., Carraro G., De Marchi G., de Wit W.-J., 2018, ArXiv e-prints

Bhardwaj A., Panwar N., Herczeg G. J., Chen W. P., Singh H. P., 2019, A&A, 627, A135

Binks A. S., Jeffries R. D., Wright N. J., 2020, MNRAS, 494(2), 2429

Binney J., Tremaine S., 1998, Princeton Series in Astrophysics,(Princeton University Press, Princeton, NJ, 1987).[Google Books].(Cited on page 36.)

Blaauw A., 1946, Publications of the Kapteyn Astronomical Laboratory Groningen, 52, 1

Blaauw A., 1952, bain, 11, 405

Blaauw A., 1964, ARA&A, 2, 213

Blitz L., Thaddeus P., 1980, apj, 241, 676

Bonnell I. A., Davies M. B., 1998, MNRAS, 295, 691

Brandt J. C., Stecher T. P., Crawford D. L., Maran S. P., 1971, ApJL, 163, L99

Bressert E., Bastian N., Gutermuth R., Megeath S. T., Allen L., Evans, II N. J., Rebull L. M., Hatchell J., Johnstone D., Bourke T. L., Cieza L. A., Harvey P. M., Merin B., Ray T. P., Tothill N. F. H., 2010, MNRAS, 409, L54

Buder S., Sharma S., Kos J., Amarsi A. M., Nordlander T., Lind K., Martell S. L., Asplund M., Bland-Hawthorn J., Casey A. R., de Silva G. M., D'Orazi V., Freeman K. C., Hayden M. R., Lewis G. F., Lin J., Schlesinger K. J., Simpson J. D., Stello D., Zucker D. B., Zwitter T., Beeson K. L., Buck T., Casagrande L., Clark J. T., Čotar K., da Costa G. S., de Grijs R., Feuillet D., Horner J., Kafle P. R., Khanna S., Kobayashi C., Liu F., Montet B. T., Nandakumar G., Nataf D. M., Ness M. K., Spina L., Tepper-García T., Ting Y.-S., Traven G., Vogrinčič R., Wittenmyer R. A., Wyse R. F. G., Žerjal M., Galah Collaboration, 2021, MNRAS

Caballero J. A., Dinis L., 2008, Astronomische Nachrichten, 329(8), 801

Cánovas H., Cantero C., Cieza L., Bombrun A., Lammers U., Merín B., Mora A., Ribas Á., Ruíz-Rodríguez D., 2019, A&A, 626, A80

Cantat-Gaudin T., Jordi C., Wright N. J., Armstrong J. J., Vallenari A., Balaguer-Núñez L., Ramos P., Bossini D., Padoan P., Pelkonen V. M., Mapelli M., Jeffries R. D., 2019a, A&A, 626, A17

Cantat-Gaudin T., Krone-Martins A., Sedaghat N., Farahi A., de Souza R. S., Ska-lidis R., Malz A. I., Macêdo S., Moews B., Jordi C., Moitinho A., Castro-Ginard A., Ishida E. E. O., Heneka C., Boucaud A., Trindade A. M. M., 2019b, A&A, 624, A126

Cantat-Gaudin T., Mapelli M., Balaguer-Núñez L., Jordi C., Sacco G., Vallenari A., 2019c, A&A, 621, A115

Cartwright A., Whitworth A. P., 2004, MNRAS, 348, 589

Clark P. C., Bonnell I. A., Klessen R. S., 2008, MNRAS, 386, 3

Clark P. C., Bonnell I. A., Zinnecker H., Bate M. R., 2005, MNRAS, 359, 809

Dale J. E., Ercolano B., Bonnell I. A., 2013, mnras, 430, 234

Dalton G., Trager S., Abrams D. C., Bonifacio P., Aguerri J. A. L., Vallenari A., Middleton K., Benn C., Dee K., Sayède F., Lewis I., Pragt J., Picó S., Walton N., Rey J., Allende Prieto C., Lhomé É., Terrett D., Brock M., Gilbert J., Ridings A., Verheijen M., Tosh I., Steele I., Stuik R., Kroes G., Tromp N., Kragt J., Lesman D., Mottram C., Bates S., Gribbin F., Burgal J. A., Herreros J. M., Delgado J. M., Martin C., Cano D., Navarro R., Irwin M., Lewis J., Gonzales Solares E., O'Mahony N., Bianco A., Zurita C., ter Horst R., Molinari E., Lodi M., Guerra J., Baruffolo A., Carrasco E., Farkas S., Schallig E., Hill V., Smith

D., Drew J., Poggianti B., Pieri M., Jin S., Dominquez Palmero L., Fariña C., Martin A., Worley C., Murphy D., Hidalgo A., Mignot S., Bishop G., Guest S., Elswijk E., de Haan M., Hanenburg H., Salasnich B., Mayya D., Izazaga-Pérez R., Peralta de Arriba L., 2018, in Evans C. J., Simard L., Takami H., eds, Ground-based and Airborne Instrumentation for Astronomy VII, Society of Photo-Optical Instrumentation Engineers (SPIE) Conference Series Vol. 10702, p. 107021B

Damiani F., Prisinzano L., Micela G., Randich S., Gilmore G., Drew J. E., Jeffries R. D., Frémat Y., Alfaro E. J., Bensby T., Bragaglia A., Flaccomio E., Lanzafame A. C., Pancino E., Recio-Blanco A., Sacco G. G., Smiljanic R., Jackson R. J., de Laverny P., Morbidelli L., Worley C. C., Hourihane A., Costado M. T., Jofré P., Lind K., Maiorca E., 2014, A&A, 566, A50

Damiani F., Prisinzano L., Jeffries R. D., Sacco G. G., Randich S., Micela G., 2017, A&A, 602, L1

Damiani F., Prisinzano L., Pillitteri I., Micela G., Sciortino S., 2019, A&A, 623, A112

De Bruijne J. H., 1999, Monthly Notices of the Royal Astronomical Society, 306(2), 381

de Jong R. S., Agertz O., Berbel A. A., Aird J., Alexander D. A., Amarsi A., Anders F., Andrae R., Ansarinejad B., Ansorge W., Antilogus P., Anwand-Heerwart H., Arentsen A., Arnadottir A., Asplund M., Auger M., Azais N., Baade D., Baker G., Baker S., Balbinot E., Baldry I. K., Banerji M., Barden S., Barklem P., Barthélémy-Mazot E., Battistini C., Bauer S., Bell C. P. M., Bellido-Tirado O., Bellstedt S., Belokurov V., Bensby T., Bergemann M., Bestenlehner J. M., Bielby R., Bilicki M., Blake C., Bland-Hawthorn J., Boeche C., Boland W., Boller T., Bongard S., Bongiorno A., Bonifacio P., Boudon D., Brooks D.,

Brown M. J. I., Brown R., Brüggen M., Brynnel J., Brzeski J., Buchert T., Buschkamp P., Caffau E., Caillier P., Carrick J., Casagrande L., Case S., Casey A., Cesarini I., Cescutti G., Chapuis D., Chiappini C., Childress M., Christlieb N., Church R., Cioni M. R. L., Cluver M., Colless M., Collett T., Comparat J., Cooper A., Couch W., Courbin F., Croom S., Croton D., Daguisé E., Dalton G., Davies L. J. M., Davis T., de Laverny P., Deason A., Dionies F., Disseau K., Doel P., Döscher D., Driver S. P., Dwelly T., Eckert D., Edge A., Edvardsson B., Youssoufi D. E., Elhaddad A., Enke H., Erfanianfar G., Farrell T., Fechner T., Feiz C., Feltzing S., Ferreras I., Feuerstein D., Feuillet D., Finoguenov A., Ford D., Fotopoulou S., Fouesneau M., Frenk C., Frey S., Gaessler W., Geier S., Gentile Fusillo N., Gerhard O., Giannantonio T., Giannone D., Gibson B., Gillingham P., González-Fernández C., Gonzalez-Solares E., Gottloeber S., Gould A., Grebel E. K., Gueguen A., Guiglion G., Haehnelt M., Hahn T., Hansen C. J., Hartman H., Hauptner K., Hawkins K., Haynes D., Haynes R., Heiter U., Helmi A., Aguayo C. H., Hewett P., Hinton S., Hobbs D., Hoenig S., Hofman D., Hook I., Hopgood J., Hopkins A., Hourihane A., Howes L., Howlett C., Huet T., Irwin M., Iwert O., Jablonka P., Jahn T., Jahnke K., Jarno A., Jin S., Jofre P., Johl D., Jones D., Jönsson H., Jordan C., Karovicova I., Khalatyan A., Kelz A., Kennicutt R., King D., Kitaura F., Klar J., Klauser U., Kneib J. P., Koch A., Koposov S., Kordopatis G., Korn A., Kosmalski J., Kotak R., Kovalev M., Kreckel K., Kripak Y., Krumpe M., Kuijken K., Kunder A., Kushniruk I., Lam M. I., Lamer G., Laurent F., Lawrence J., Lehmitz M., Lemasle B., Lewis J., Li B., Lidman C., Lind K., Liske J., Lizon J. L., Loveday J., Ludwig H. G., McDermid R. M., Maguire K., Mainieri V., Mali S., Mandel H., Mandel K., Mannering L., Martell S., Martinez Delgado D., Matijevic G., McGregor H., McMahon R., McMillan P., Mena O., Merloni A., Meyer M. J., Michel C., Micheva G., Migniau J. E., Minchev I., Monari G., Muller R., Murphy D., Muthukrishna D., Nandra K., Navarro R., Ness M., Nichani V., Nichol

R., Nicklas H., Niederhofer F., Norberg P., Obreschkow D., Oliver S., Owers
M., Pai N., Pankratow S., Parkinson D., Paschke J., Paterson R., Pecontal A.,
Parry I., Phillips D., Pillepich A., Pinard L., Pirard J., Piskunov N., Plank V.,
Plüschke D., Pons E., Popesso P., Power C., Pragt J., Pramskiy A., Pryer D.,
Quattri M., Queiroz A. B. d. A., Quirrenbach A., Rahurkar S., Raichoor A.,
Ramstedt S., Rau A., Recio-Blanco A., Reiss R., Renaud F., Revaz Y., Rhode
P., Richard J., Richter A. D., Rix H. W., Robotham A. S. G., Roelfsema R.,
Romaniello M., Rosario D., Rothmaier F., Roukema B., Ruchti G., Rupprecht
G., Rybizki J., Ryde N., Saar A., Sadler E., Sahlén M., Salvato M., Sassolas B.,
Saunders W., Saviauk A., Sbordone L., Schmidt T., Schnurr O., Scholz R. D.,
Schwope A., Seifert W., Shanks T., Sheinis A., Sivov T., Skúladóttir Á., Smartt
S., Smedley S., Smith G., Smith R., Sorce J., Spitler L., Starkenburg E., Stein-
metz M., Stilz I., Storm J., Sullivan M., Sutherland W., Swann E., Tamone A.,
Taylor E. N., Teillon J., Tempel E., ter Horst R., Thi W. F., Tolstoy E., Trager
S., Traven G., Tremblay P. E., Tresse L., Valentini M., van de Weygaert R., van
den Ancker M., Veljanoski J., Venkatesan S., Wagner L., Wagner K., Walcher
C. J., Waller L., Walton N., Wang L., Winkler R., Wisotzki L., Worley C. C.,
Worseck G., Xiang M., Xu W., Yong D., Zhao C., Zheng J., Zscheyge F., Zucker
D., 2019, The Messenger, 175, 3

de Mink S. E., Sana H., Langer N., Izzard R. G., Schneider F. R. N., 2014, ApJ,
782(1), 7

de Zeeuw P. T., Hoogerwerf R., de Bruijne J. H. J., Brown A. G. A., Blaauw A.,
1999, AJ, 117, 354

Dobbs C. L., Adamo A., Few C. G., Calzetti D., Dale D. A., Elmegreen B. G., Evans
A. S., Gouliermis D. A., Grasha K., Grebel E. K., Johnson K. E., Kim H., Lee
J. C., Messa M., Ryon J. E., Smith L. J., Thilker D., Ubeda L., Whitmore B.,
2017, MNRAS, 464(3), 3580

Duerr R., Imhoff C. L., Lada C. J., 1982, ApJ, 261, 135

Eddington A. S., 1914, Stellar movements and the structure of the universe

Eggen O. J., 1980, ApJ, 238, 627

Eggen O. J., 1982, ApJS, 50, 199

Eggen O. J., 1983, AJ, 88, 197

Eggen O. J., 1986, AJ, 92, 1074

Ekström S., Georgy C., Eggenberger P., Meynet G., Mowlavi N., Wyttenbach A., Granada A., Decressin T., Hirschi R., Frischknecht U., Charbonnel C., Maeder A., 2012, A&A, 537, A146

Elmegreen B. G., Lada C. J., 1977, ApJ, 214, 725

Elmegreen B. G., Efremov Y., Pudritz R. E., Zinnecker H., 2000, Protostars and Planets IV, , 179

Elson R. A., Fall S. M., Freeman K. C., 1987, The Astrophysical Journal, 323, 54

Fall S. M., Chandar R., Whitmore B. C., 2005, apjl, 631, L133

Farias J. P., Tan J. C., Eyer L., 2020, arXiv e-prints, , arXiv:2005.04762

Feast M., Whitelock P., 1997, MNRAS, 291(4), 683

Fellhauer M., Kroupa P., 2005, ApJ, 630, 879

Foreman-Mackey D., Hogg D. W., Lang D., Goodman J., 2013, Publications of the Astronomical Society of the Pacific, 125, 306

Frank A., Ray T. P., Cabrit S., Hartigan P., Arce H. G., Bacciotti F., Bally J., Benisty M., Eislöffel J., Güdel M., Lebedev S., Nisini B., Raga A., 2014, Protostars and Planets VI, , 451

Frasca A., Biazzo K., Lanzafame A. C., Alcalá J. M., Brugaletta E., Klutsch A., Stelzer B., Sacco G. G., Spina L., Jeffries R. D., Montes D., Alfaro E. J., Barentsen G., Bonito R., Gameiro J. F., López-Santiago J., Pace G., Pasquini L., Prisinzano L., Sousa S. G., Gilmore G., Randich S., Micela G., Bragaglia A., Flaccomio E., Bayo A., Costado M. T., Franciosini E., Hill V., Hourihane A., Jofré P., Lardo C., Maiorca E., Masseron T., Morbidelli L., Worley C. C., 2015, A&A, 575, A4

Fuchs B., Breitschwerdt D., de Avillez M. A., Dettbarn C., Flynn C., 2006, MNRAS, 373(3), 993

Gaia Collaboration, Brown A. G. A., Vallenari A., Prusti T., de Bruijne J. H. J., Mignard F., Drimmel R., Babusiaux C., Bailer-Jones C. A. L., Bastian U., et al., 2016a, A&A, 595, A2

Gaia Collaboration, Prusti T., de Bruijne J. H. J., Brown A. G. A., Vallenari A., Babusiaux C., Bailer-Jones C. A. L., Bastian U., Biermann M., Evans D. W., 2016b, A&A, 595, A1

Gaia Collaboration, Prusti T., de Bruijne J. H. J., Brown A. G. A., Vallenari A., Babusiaux C., Bailer-Jones C. A. L., Bastian U., Biermann M., Evans D. W., et al., 2016c, A&A, 595, A1

Gao X.-h., 2018, PASP, 130(994), 124101

Gieles M., Sana H., Zwart S. P., 2010, Monthly Notices of the Royal Astronomical Society, 402(3), 1750

Gielesen W., de Bruijn D., van den Dool T., Kamphues F., Meijer E., Calvel B., Laborie A., Monteiro D., Coatantiec C., Touzeau S., 2012, Space Telescopes and Instrumentation 2012: Optical, Infrared, and Millimeter Wave, Society of Photo-Optical Instrumentation Engineers (SPIE) Conference Series Vol. 8442, p. 84421R

Gielesen W., de Bruijn D., van den Dool T., Kamphues F., Meijer E., Braam B. C., 2017, Society of Photo-Optical Instrumentation Engineers (SPIE) Conference Series, Society of Photo-Optical Instrumentation Engineers (SPIE) Conference Series Vol. 10564, p. 105641Z

Gilmore G., Randich S., Asplund M., Binney J., Bonifacio P., Drew J., Feltzing S., Ferguson A., Jeffries R., Micela G., et al., 2012, The Messenger, 147, 25

Goodwin S. P., Whitworth A. P., 2004, A&A, 413, 929

Hacar A., Tafalla M., 2011, A&A, 533, A34

Hacar A., Tafalla M., Kauffmann J., Kovács A., 2013, A&A, 554, A55

Hacar A., Alves J., Forbrich J., Meingast S., Kubiak K., Großschedl J., 2016, A&A, 589, A80

Helmi A., Babusiaux C., Koppelman H. H., Massari D., Veljanoski J., Brown A. G. A., 2018, Nature, 563(7729), 85

Hénault-Brunet V., Gieles M., Evans C. J., Sana H., Bastian N., Maíz Apellániz J., Taylor W. D., Markova N., Bressert E., de Koter A., van Loon J. T., 2012, A&A, 545, L1

Herbst W., Herbst D. K., Grossman E. J., Weinstein D., 1994, AJ, 108, 1906

Hillenbrand L. A., Hartmann L. W., 1998, apj, 492, 540

Hills J. G., 1980, ApJ, 235, 986

Hogg D. W., Bovy J., Lang D., 2010, arXiv e-prints, , arXiv:1008.4686

Holmberg J., Flynn C., 2004, MNRAS, 352(2), 440

Hoogerwerf R., Aguilar L. A., 1999, Monthly Notices of the Royal Astronomical Society, 306(2), 394

Huang Y., Liu X. W., Chen B. Q., Zhang H. W., Yuan H. B., Xiang M. S., Wang C., Tian Z. J., 2018, AJ, 156(3), 90

Humphreys R. M., 1978, ApJS, 38, 309

Hunt E. L., Reffert S., 2021, A&A, 646, A104

Jackson R. J., Deliyannis C. P., Jeffries R. D., 2018, MNRAS, 476, 3245

Jackson R. J., Jeffries R. D., Wright N. J., Rand ich S., Sacco G., Pancino E., Cantat-Gaudin T., Gilmore G., Vallenari A., Bensby T., Bayo A., Costado M. T., Franciosini E., Gonneau A., Hourihane A., Lewis J., Monaco L., Morbidelli L., Worley C., 2020, MNRAS

Jeffries R. D., Oliveira J. M., 2005, MNRAS, 358, 13

Jeffries R. D., Naylor T., Devey C. R., Totten E. J., 2004, MNRAS, 351, 1401

Jeffries R. D., Naylor T., Walter F. M., Pozzo M. P., Devey C. R., 2009, MNRAS, 393, 538

Jeffries R. D., Jackson R. J., Cottaar M., Koposov S. E., Lanzafame A. C., Meyer M. R., Prisinzano L., Randich S., Sacco G. G., Brugaletta E., Caramazza M., Damiani F., Franciosini E., Frasca A., Gilmore G., Feltzing S., Micela G., Alfaro E., Bensby T., Pancino E., Recio-Blanco A., de Laverny P., Lewis J., Magrini

L., Morbidelli L., Costado M. T., Jofré P., Klutsch A., Lind K., Maiorca E., 2014, A&A, 563, A94

Jeffries R. D., Jackson R. J., Franciosini E., Rand ich S., Barrado D., Frasca A., Klutsch A., Lanzafame A. C., Prisinzano L., Sacco G. G., Gilmore G., Vallenari A., Alfaro E. J., Koposov S. E., Pancino E., Bayo A., Casey A. R., Costado M. T., Damiani F., Hourihane A., Lewis J., Jofre P., Magrini L., Monaco L., Morbidelli L., Worley C. C., Zaggia S., Zwitter T., 2017, MNRAS, 464(2), 1456

Jeffries R. D., Jackson R. J., Sun Q., Deliyannis C. P., 2021, MNRAS, 500(1), 1158

Johnson D. R. H., Soderblom D. R., 1987, AJ, 93, 864

Jones D. H. P., 1971, mnras, 152, 231

Jordi C., Gebran M., Carrasco J. M., de Bruijne J., Voss H., Fabricius C., Knude J., Vallenari A., Kohley R., Mora A., 2010, A&A, 523, A48

Kapteyn J. C., 1914, apj, 40

Kapteyn J. C., 1918, apj, 47, 104

Karim M. T., Mamajek E. E., 2017, MNRAS, 465(1), 472

King I., 1962, The Astronomical Journal, 67, 471

King I. R., 1966, The Astronomical Journal, 71, 64

Kos J., Lin J., Zwitter T., Žerjal M., Sharma S., Bland-Hawthorn J., Asplund M., Casey A. R., De Silva G. M., Freeman K. C., Martell S. L., Simpson J. D., Schlesinger K. J., Zucker D., Anguiano B., Bacigalupo C., Bedding T. R., Betters C., Da Costa G., Duong L., Hyde E., Ireland M., Kafle P. R., Leon-Saval S., Lewis G. F., Munari U., Nataf D., Stello D., Tinney C. G., Traven G., Watson F., Wittenmyer R. A., 2017, MNRAS, 464(2), 1259

Kounkel M., Covey K., Suárez G., Román-Zúñiga C., Hernandez J., Stassun K., Jaehnig K. O., Feigelson E. D., Peña Ramírez K., Roman-Lopes A., Da Rio N., Stringfellow G. S., Kim J. S., Borissova J., Fernández-Trincado J. G., Burgasser A., García-Hernández D. A., Zamora O., Pan K., Nitschelm C., 2018, AJ, 156(3), 84

Krause M. G. H., Burkert A., Diehl R., Fierlinger K., Gaczkowski B., Kroell D., Ngoumou J., Roccatagliata V., Siegert T., Preibisch T., 2018, A&A, 619, A120

Kroupa P., 2002, Science, 295, 82

Kroupa P., Aarseth S., Hurley J., 2001, MNRAS, 321, 699

Kruijssen J. M. D., 2012, MNRAS, 426, 3008

Kruijssen J. M. D., Maschberger T., Moeckel N., Clarke C. J., Bastian N., Bonnell I. A., 2012, MNRAS, 419, 841

Krumholz M. R., Matzner C. D., 2009, ApJ, 703, 1352

Kurucz R. L., 1992, in Barbuy B., Renzini A., eds, The Stellar Populations of Galaxies, IAU Symposium Vol. 149, p. 225

Lada C. J., Lada E. A., 2003, araa, 41, 57

Lada C. J., Margulis M., Dearborn D., 1984, ApJ, 285, 141

Lanzafame A. C., Frasca A., Damiani F., Franciosini E., Cottaar M., Sousa S. G., Tabernero H. M., Klutsch A., Spina L., Biazzo K., Prisinzano L., Sacco G. G., Randich S., Brugaletta E., Delgado Mena E., Adibekyan V., Montes D., Bonito R., Gameiro J. F., Alcalá J. M., González Hernández J. I., Jeffries R., Messina S., Meyer M., Gilmore G., Asplund M., Binney J., Bonifacio P., Drew J. E., Feltzing S., Ferguson A. M. N., Micela G., Negueruela I., Prusti T., Rix H. W.,

Vallenari A., Alfaro E. J., Allende Prieto C., Babusiaux C., Bensby T., Blomme R., Bragaglia A., Flaccomio E., Francois P., Hambly N., Irwin M., Koposov S. E., Korn A. J., Smiljanic R., Van Eck S., Walton N., Bayo A., Bergemann M., Carraro G., Costado M. T., Edvardsson B., Heiter U., Hill V., Hourihane A., Jackson R. J., Jofré P., Lardo C., Lewis J., Lind K., Magrini L., Marconi G., Martayan C., Masseron T., Monaco L., Morbidelli L., Sbordone L., Worley C. C., Zaggia S., 2015, A&A, 576, A80

Larson R. B., 1995, MNRAS, 272, 213

Lee Y.-N., Offner S. S. R., Hennebelle P., André P., Zinnecker H., Ballesteros-Paredes J., Inutsuka S.-i., Kruijssen J. M. D., 2020, SSRv, 216(4), 70

Lewis I. J., Cannon R. D., Taylor K., Glazebrook K., Bailey J. A., Baldry I. K., Barton J. R., Bridges T. J., Dalton G. B., Farrell T. J., Gray P. M., Lankshear A., McCowage C., Parry I. R., Sharples R. M., Shortridge K., Smith G. A., Stevenson J., Straede J. O., Waller L. G., Whittard J. D., Wilcox J. K., Willis K. C., 2002, MNRAS, 333(2), 279

Lindegren L., Bastian U., 2010, EAS Publications Series Vol. 45, p. 109

Lindegren L., Lammers U., Hobbs D., O'Mullane W., Bastian U., Hernández J., 2012, A&A, 538, A78

Lindegren L., Lammers U., Bastian U., Hernández J., Klioner S., Hobbs D., Bombrun A., Michalik D., Ramos-Lerate M., Butkevich A., 2016, A&A, 595, A4

Lindegren L., Hernández J., Bombrun A., Klioner S., Bastian U., Ramos-Lerate M., de Torres A., Steidelmüller H., Stephenson C., Hobbs D., 2018a, A&A, 616, A2

Lindegren L., Hernández J., Bombrun A., Klioner S., Bastian U., Ramos-Lerate M., de Torres A., Steidelmüller H., Stephenson C., Hobbs D., Lammers U.,

Biermann M., Geyer R., Hilger T., Michalik D., Stampa U., McMillan P. J., Castañeda J., Clotet M., Comoretto G., Davidson M., Fabricius C., Gracia G., Hambly N. C., Hutton A., Mora A., Portell J., van Leeuwen F., Abbas U., Abreu A., Altmann M., Andrei A., Anglada E., Balaguer-Núñez L., Barache C., Becciani U., Bertone S., Bianchi L., Bouquillon S., Bourda G., Brüsemeister T., Bucciarelli B., Busonero D., Buzzi R., Cancelliere R., Carlucci T., Charlot P., Cheek N., Crosta M., Crowley C., de Bruijne J., de Felice F., Drimmel R., Esquej P., Fienga A., Fraile E., Gai M., Garralda N., González-Vidal J. J., Guerra R., Hauser M., Hofmann W., Holl B., Jordan S., Lattanzi M. G., Lenhardt H., Liao S., Licata E., Lister T., Löffler W., Marchant J., Martin-Fleitas J.-M., Messineo R., Mignard F., Morbidelli R., Poggio E., Riva A., Rowell N., Salguero E., Sarasso M., Sciacca E., Siddiqui H., Smart R. L., Spagna A., Steele I., Taris F., Torra J., van Elteren A., van Reeven W., Vecchiato A., 2018b, A&A, 616, A2

Luri X., Brown A. G. A., Sarro L. M., Arenou F., Bailer-Jones C. A. L., Castro-Ginard A., de Bruijne J., Prusti T., Babusiaux C., Delgado H. E., 2018, ArXiv e-prints

Mapelli M., Vallenari A., Jeffries R. D., Gavagnin E., Cantat-Gaudin T., Sacco G. G., Meyer M. R., Alfaro E. J., Costado M., Damiani F., 2015, A&A, 578, A35

Marigo P., Girardi L., Bressan A., Rosenfield P., Aringer B., Chen Y., Dussin M., Nanni A., Pastorelli G., Rodrigues T. S., Trabucchi M., Bladh S., Dalcanton J., Groenewegen M. A. T., Montalbán J., Wood P. R., 2017, ApJ, 835(1), 77

Martell S. L., Sharma S., Buder S., Duong L., Schlesinger K. J., Simpson J., Lind K., Ness M., Marshall J. P., Asplund M., Bland-Hawthorn J., Casey A. R., De Silva G., Freeman K. C., Kos J., Lin J., Zucker D. B., Zwitter T., Anguiano B., Bacigalupo C., Carollo D., Casagrande L., Da Costa G. S., Horner J., Huber D.,

Hyde E. A., Kafle P. R., Lewis G. F., Nataf D., Navin C. A., Stello D., Tinney C. G., Watson F. G., Wittenmyer R., 2017, MNRAS, 465(3), 3203

Maschberger T., 2013, MNRAS, 429, 1725

Massey P., 2003, araa, 41, 15

McBride A., Kounkel M., 2019, ApJ, 884(1), 6

McKee C. F., Tan J. C., 2003, ApJ, 585(2), 850

McMahon R. G., Banerji M., Gonzalez E., Koposov S. E., Bejar V. J., Lodieu N., Rebolo R., VHS Collaboration, 2013, The Messenger, 154, 35

Merloni A., Nandra K., Predehl P., 2020, Nature Astronomy, 4, 634

Miller G. E., Scalo J. M., 1979, apjs, 41, 513

Miville-Deschênes M.-A., Lagache G., 2005, ApJS, 157(2), 302

Mora A., Biermann M., Brown A. G. A., Busonero D., Carminati L., Carrasco J. M., Chassat F., Erdmann M., Gielesen W. L. M., Jordi C., 2014, Space Telescopes and Instrumentation 2014: Optical, Infrared, and Millimeter Wave, Society of Photo-Optical Instrumentation Engineers (SPIE) Conference Series Vol. 9143, p. 91430X

Naylor T., Totten E. J., Jeffries R. D., Pozzo M., Devey C. R., Thompson S. A., 2002, MNRAS, 335, 291

Netopil M., Paunzen E., Heiter U., Soubiran C., 2016, VizieR Online Data Catalog, , J/A+A/585/A150

North J. R., Tuthill P. G., Tango W. J., Davis J., 2007, MNRAS, 377, 415

Oort J. H., 1954, bain, 12, 177

Opik E. J., 1953, Irish Astronomical Journal, 2, 219

Parker R. J., Wright N. J., Goodwin S. P., Meyer M. R., 2014, MNRAS, 438, 620

Pecaut M. J., Mamajek E. E., 2013, ApJS, 208, 9

Pecaut M. J., Mamajek E. E., 2016, MNRAS, 461, 794

Perryman M. A. C., Lindegren L., Kovalevsky J., Hoeg E., Bastian U., Bernacca
    P. L., Crézé M., Donati F., Grenon M., Grewing M., van Leeuwen F., van der
    Marel H., Mignard F., Murray C. A., Le Poole R. S., Schrijver H., Turon C.,
    Arenou F., Froeschlé M., Petersen C. S., 1997, A&A, 323, L49

Pfalzner S., Kaczmarek T., 2013, A&A, 555, A135

Plummer H. C., 1911, Monthly notices of the royal astronomical society, 71, 460

Pozzo M., Jeffries R. D., Naylor T., Totten E. J., Harmer S., Kenyon M., 2000,
    MNRAS, 313, L23

Preibisch T., Feigelson E. D., 2005, apjs, 160, 390

Prisinzano L., Damiani F., Micela G., Jeffries R. D., Franciosini E., Sacco G. G.,
    Frasca A., Klutsch A., Lanzafame A., Alfaro E. J., Biazzo K., Bonito R., Bra-
    gaglia A., Caramazza M., Vallenari A., Carraro G., Costado M. T., Flaccomio E.,
    Jofré P., Lardo C., Monaco L., Morbidelli L., Mowlavi N., Pancino E., Randich
    S., Zaggia S., 2016, A&A, 589, A70

Robin A. C., Reylé C., Derrière S., Picaud S., 2003, A&A, 409, 523

Sacco G. G., Jeffries R. D., Randich S., Franciosini E., Jackson R. J., Cottaar M.,
    Spina L., Palla F., Mapelli M., Alfaro E. J., Bonito R., Damiani F., Frasca A.,
    Klutsch A., Lanzafame A., Bayo A., Barrado D., Jiménez-Esteban F., Gilmore
    G., Micela G., Vallenari A., Allende Prieto C., Flaccomio E., Carraro G.,

Costado M. T., Jofré P., Lardo C., Magrini L., Morbidelli L., Prisinzano L., Sbordone L., 2015, A&A, 574, L7

Sacco G. G., Spina L., Randich S., Palla F., Parker R. J., Jeffries R. D., Jackson R., Meyer M. R., Mapelli M., Lanzafame A. C., Bonito R., Damiani F., Franciosini E., Frasca A., Klutsch A., Prisinzano L., Tognelli E., Degl'Innocenti S., Prada Moroni P. G., Alfaro E. J., Micela G., Prusti T., Barrado D., Biazzo K., Bouy H., Bravi L., Lopez-Santiago J., Wright N. J., Bayo A., Gilmore G., Bragaglia A., Flaccomio E., Koposov S. E., Pancino E., Casey A. R., Costado M. T., Donati P., Hourihane A., Jofré P., Lardo C., Lewis J., Magrini L., Monaco L., Morbidelli L., Sousa S. G., Worley C. C., Zaggia S., 2017, aap, 601, A97

Sahu M. S., 1992, PhD thesis, Kapteyn Institute, Postbus 800 9700 AV Groningen, The Netherlands

Salpeter E. E., 1955, apj, 121, 161

Samus' N. N., Kazarovets E. V., Durlevich O. V., Kireeva N. N., Pastukhova E. N., 2017, Astronomy Reports, 61(1), 80

Sánchez N., Alfaro E. J., 2009, ApJ, 696, 2086

Scally A., Clarke C., 2002, MNRAS, 334, 156

Schneider N., Csengeri T., Hennemann M., Motte F., Didelon P., Federrath C., Bontemps S., Di Francesco J., Arzoumanian D., Minier V., André P., Hill T., Zavagno A., Nguyen-Luong Q., Attard M., Bernard J. P., Elia D., Fallscheer C., Griffin M., Kirk J., Klessen R., Könyves V., Martin P., Men'shchikov A., Palmeirim P., Peretto N., Pestalozzi M., Russeil D., Sadavoy S., Sousbie T., Testi L., Tremblin P., Ward-Thompson D., White G., 2012, A&A, 540, L11

Schoettler C., de Bruijne J., Vaher E., Parker R. J., 2020, MNRAS, 495(3), 3104

Schönrich R., Binney J., Dehnen W., 2010, MNRAS, 403(4), 1829

Sharp R., Birchall M. N., 2010, PASA, 27(1), 91

Sheinis A., Anguiano B., Asplund M., Bacigalupo C., Barden S., Birchall M., Bland
     -Hawthorn J., Brzeski J., Cannon R., Carollo D., Case S., Casey A., Churilov
     V., Warrick C., Dean R., De Silva G., D'Orazi V., Duong L., Farrell T., Fiegert
     K., Freeman K., Gabriella F., Gers L., Goodwin M., Gray D., Green A., Heald
     R., Heijmans J., Ireland M., Jones D., Kafle P., Keller S., Klauser U., Kondrat
     Y., Kos J., Lawrence J., Lee S., Mali S., Martell S., Mathews D., Mayfield D.,
     Miziarski S., Muller R., Pai N., Patterson R., Penny E., Orr D., Schlesinger
     K., Sharma S., Shortridge K., Simpson J., Smedley S., Smith G., Stafford D.,
     Staszak N., Vuong M., Waller L., de Boer E. W., Xavier P., Zheng J., Zhelem R.,
     Zucker D., Zwitter T., 2015, Journal of Astronomical Telescopes, Instruments,
     and Systems, 1, 035002

Siess L., Dufour E., Forestini M., 2000, aap, 358, 593

Simpson J. D., De Silva G. M., Martell S. L., Zucker D. B., Ferguson A. M. N.,
     Bernard E. J., Irwin M., Penarrubia J., Tolstoy E., 2017, MNRAS, 471(4), 4087

Skrutskie M. F., Cutri R. M., Stiening R., Weinberg M. D., Schneider S., Carpenter
     J. M., Beichman C., Capps R., Chester T., Elias J., Huchra J., Liebert J.,
     Lonsdale C., Monet D. G., Price S., Seitzer P., Jarrett T., Kirkpatrick J. D.,
     Gizis J. E., Howard E., Evans T., Fowler J., Fullmer L., Hurt R., Light R.,
     Kopan E. L., Marsh K. A., McCallon H. L., Tam R., Van Dyk S., Wheelock S.,
     2006, AJ, 131(2), 1163

Sneden C., Bean J., Ivans I., Lucatello S., Sobeck J., 2012, , ascl:1202.009

Soderblom D. R., 2010, araa, 48, 581

Soderblom D. R., Hillenbrand L. A., Jeffries R. D., Mamajek E. E., Naylor T., 2014, Protostars and Planets VI, , 219

Spitzer L., 1987, Dynamical evolution of globular clusters

Stahler S. W., Palla F., 2008, The formation of stars, John Wiley & Sons

Straka W. C., 1973, ApJ, 180, 907

Tognelli E., Prada Moroni P. G., Degl'Innocenti S., 2011, A&A, 533, A109

Tutukov A. V., 1978, A&A, 70, 57

Upton E. K. L., 1973, NASA Special Publication, 332, 119

van Leeuwen F., 2007, A&A, 474(2), 653

von Hoerner S., 1968, Bulletin Astronomique, 3, 147

Ward J. L., Kruijssen J. M. D., 2018, MNRAS, 475, 5659

Weidner C., Kroupa P., Bonnell I. A. D., 2010, MNRAS, 401, 275

Whitworth A., 1979, mnras, 186, 59

Williams J. P., Blitz L., McKee C. F., 2000, Protostars and Planets IV, , 97

Wright N. J., Drake J. J., 2009, apjs, 184, 84

Wright N. J., Mamajek E. E., 2018, MNRAS, 476, 381

Wright N. J., Parker R. J., 2019, MNRAS, , 2232

Wright N. J., Parker R. J., Goodwin S. P., Drake J. J., 2014, MNRAS, 438, 639

Wright N. J., Bouy H., Drew J. E., Sarro L. M., Bertin E., Cuillandre J.-C., Barrado D., 2016, MNRAS, 460, 2593

Wright N. J., Jeffries R. D., Jackson R. J., Bayo A., Bonito R., Damiani F., Kalari V., Lanzafame A. C., Pancino E., Parker R. J., Prisinzano L., Randich S., Vink J. S., Alfaro E. J., Bergemann M., Franciosini E., Gilmore G., Gonneau A., Hourihane A., Jofré P., Koposov S. E., Lewis J., Magrini L., Micela G., Morbidelli L., Sacco G. G., Worley C. C., Zaggia S., 2019, MNRAS, 486(2), 2477

Zari E., Brown A. G. A., de Zeeuw P. T., 2019, A&A, 628, A123

Zinnecker H., 1984, mnras, 210, 43

Zwart S. P., McMillan S., Gieles M., 2010, arXiv preprint arXiv:1002.1961

Zwitter T., Kos J., Buder S., Čotar K., Asplund M., Bland-Hawthorn J., Casey A. R., De Silva G. M., D'Orazi V., Freeman K. C., Hayden M. R., Lewis G. F., Lin J., Lind K., Martell S. L., Schlesinger K. J., Sharma S., Simpson J. D., Stello D., Zucker D. B., Beeson K. L., de Grijs R., Nordlander T., Ting Y.-S., Traven G., Vogrinčič R., Watson F., Wittenmyer R., 2020, arXiv e-prints, , arXiv:2012.12201